TRANS-ROTARY MAGNETIC GEAR FOR WAVE ENERGY APPLICATION

A Dissertation

by

SIAVASH PAKDELIAN

Submitted to the Office of Graduate and Professional Studies of
Texas A&M University
in partial fulfillment of the requirements for the degree of

DOCTOR OF PHILOSOPHY

Chair of Committee,	Hamid A. Toliyat
Committee Members,	Robert S. Balog
	Shankar P. Bhattacharyya
	Won-jong Kim
Head of Department,	Chanan Singh

December 2014

Major Subject: Electrical Engineering

ABSTRACT

This dissertation looks into a type of magnetic gear, referred to as the Trans-Rotary Magnetic Gear (TROMAG), for reciprocating Wave Energy Converters (WECs). A TROMAG consists of two main parts: a translator that is coupled, mechanically or magnetically, to a buoy and a rotor that is coupled to a rotary generator. The device accomplishes two tasks: it converts linear motion to rotation (and vice versa) through magnetic fields, and at the same time it does a gearing action. This means that it can convert the high-force, low-speed linear motion of a buoy to a low-torque, high-speed rotation, which enables using a compact, high-speed rotary generator. As a magnetic gear, the TROMAG offers contact-free force transmission and its consequent advantages such as reduced wear and tear, reduced need for lubrication and maintenance, high reliability, and inherent overload protection capability. In this dissertation, first, the motivation behind developing the TROMAG is presented. Then, the structure of the device and its principles of operation are laid out. Moreover, aspects of magnetic design are studied by using either an analytical model, three-dimensional (3D) finite element analysis (FEA) or two-dimensional (2D) FEA. It is shown that, for a high-force, low-speed load characteristic, a system comprising a TROMAG and a rotary machine would far surpass a direct drive linear machine (DDLM) designed for the same force and speed, in terms of weight, cost, and volume of the required active material. In addition, a nonlinear analytical model is proposed to describe the dynamic behavior of the TROAMG. The model is then linearized and combined with the linearized model of a

buoy in order to study the dynamics of the entire wave energy conversion system. Furthermore, a demonstrative prototype of the TROMAG is constructed and tested to verify the theoretical concepts and employed analyses.

To my parents: *Naser and Forough*

To my wife, *Mahshid*

ACKNOWLEDGEMENTS

I wish to acknowledge and deeply thank those who have helped me in accomplishing this dissertation. First and foremost, my heartfelt appreciation goes to my advisor, Prof. Hamid Toliyat, for his unparalleled support and encouragement. His deep knowledge and invaluable experience made this work possible. I feel blessed to have had such a caring and considerate mentor and advisor.

My sincere gratitude goes also to the members of my graduate study committee, Prof. Robert Balog, Prof. Shankar Bhattacharyya, and Prof. Won-jong Kim, for their precious time and insightful comments, as well as the wonderful courses I took from them. I have benefited from their knowledge, help, and guidance throughout the course of my studies.

I also wish to thank the Electrical and Computer Engineering Department at Texas A&M University for providing me with a great educational environment. For all their help and efforts, I especially acknowledge Prof. Chanan Singh, Prof. Krishna Narayanan, Prof. Scott L. Miller, Ms. Tammy Carda, Ms. Jeanie Marshal, Ms. Anni Brunker, Ms. Claudia Samford, Ms. Eugenia Costea, Ms. Janice Allen, Ms. Sheryl Mallett, Mr. Wayne Matous, Mr. Henry Gongora, Ms. Deana Totzke, Ms. Rebecca Rice, Ms. Nancy Reichart, Mr. Chris Jones, and Mr. Jessie Hernandez.

My appreciation is extended to Dr. Waqas Arshad and Dr. Zach Pan at the ABB Corporate Research Center in the U.S., Raleigh, North Carolina, for providing me with the opportunity to work in an excellent environment. During my time at that research center, I had the opportunity to learn also from Dr. Hongrae Kim, Dr. Steven

Englebretson, Dr. Darren Tremelling, and Dr. Sandeep Bala. I thank them here. In addition, I sincerely thank the ABB U.S. CRC for their three-year fellowship, which partially supported my Ph.D. studies.

I express my appreciation to Mr. John Vilas, a machinist from Bryan, Texas, who helped with building my prototype.

I am genuinely grateful to my past and present colleagues at Texas A&M University. They helped to make great memories for me to carry along for the rest of my life. I especially thank Vivek Sundaram on whom I have always relied for generous and unlimited help. I am truly thankful to Dr. Yateendra Deshpande for long hours of provocative and inspiring discussions, and the valuable experiences of the work we did together. Many thanks to Jae-bum Park for being a great lab manager and helping me with finding everything I needed in the lab. I am grateful to Dr. Nicolas Frank for all the collaboration we had on magnetic gears. I am grateful to Dr. Babak Farhangi for his friendship and the great time we had together. I appreciate Dr. Robert Vartanian and Behrouz Nikbakhtan for their friendship and all of the fun moments. I acknowledge Mathew Johnson for all his help. Moreover, I wish to thank Khalid Ali Al Jafaari, Hussain Hussain, Esra Ozkentli, Abdulkadir Bostanci, Dr. Seung-Deog Choi, Dr. Jeihoon Baek, Morteza Mousavi, Bahar Anvari, Niloofar Torabi, Mathew Gardner, Amir Negahdari, Ajay Kumar Morya, Dr. Mehran Mirjafari, Dr. Souhib Harb, Dr. Somasundaram Essakiappan, Mohammad Shadmand, Pawan Garg, Harish Sarma Krishnamoorthy, Samantha Castillo, Poornima Mazumdar, and Dibyendu Rana.

I am deeply indebted to my parents, Naser and Forough; my brothers, Reza, Ali, and Siroos; and my sisters, Anahita and Faranak. Throughout my life, they have showered me with unconditional love and support.

And I cannot find the words to express my appreciation to my wife, Mahshid. Her beautiful heart and sincere emotions have kept me optimistic about life. She has persistently encouraged me and has held my back at every moment of our life. Without her endless love, help, support, and care, I would have been unable to accomplish this dissertation.

TABLE OF CONTENTS

Page

LIST OF FIGURES

Page

LIST OF TABLES

Page

1. INTRODUCTION

1.1. Ocean wave energy__ advantages and challenges

The methods for harvesting energy from the ocean waves can be traced back to the late 18th century; however, modern research into the wave energy, similar to research into wind energy, was initiated by the oil crisis of the 1970s [1]. Concerns regarding energy security and climate change have once again made generating electricity from renewable sources an important area of research. It is estimated that the potential worldwide wave power resource is 2 TW [1]. Rich wave resources are found in western coasts toward the poles, especially those of Europe, the United States, and Australia [2].

Ocean wave energy offers certain advantages over other types of renewable energy resources that potentially make it an important contributor to the renewable energy mix of the future. The main advantages are [1], [3]:

- High energy density: Among renewable energy sources, ocean waves are the most energy-dense type. The wave energy is a concentrated form of solar energy: solar energy density, which is typically 0.1–0.3 kW/m^2 of horizontal surface, is converted to an average power density of 2–3 kW/m^2 on a vertical plane perpendicular to the direction of wave propagation just below the water surface [1].

- High capacity factor: While strong-enough waves are available almost 90% of the time, the typical numbers lie within the range of 20–30% for wind and solar power devices [4].
- High predictability: With measurement buoys based several hundred miles offshore, it is possible to forecast the available energy 10 hours or more ahead of time [3]. This is very important from a grid management perspective.
- Unlike wind, rich resources are very close to densely populated areas. This would reduce the overall cost of electricity through reducing transmission costs.
- Unlike offshore wind turbines, offshore Wave Energy Converters (WECs) are not visible from shore. This advantage distinguishes WECs from other renewable energy resources in terms of aesthetics.

To realize these advantages and make wave energy harvesting commercially competitive, particular challenges need to be overcome. Some of these challenges are listed below [1]:

- The power of the waves varies as the height and period of the waves change. Efficiently capturing this irregular motion is challenging. On one hand, an efficient design tailors the system rating to the most common wave power levels; on the other hand, the designed system, must be able to withstand the extreme wave conditions, which, although rare, could have power levels more than 100 times the average values. This criterion poses not only structural engineering challenges, but also economic ones: while the normal amount of energy a device can harness is determined by the most commonly occurring waves, the need to

withstand the high power level of the extreme, yet infrequent waves determines the capital cost of device construction.

- The ocean is a highly corrosive environment, which poses challenges in terms of material selection, sealing, etc.

While the challenges listed above are mainly pertinent to fields of civil, mechanical, and material engineering, there is another issue, possibly the most challenging of all [1], which must be addressed specifically by designers of electric machines. The challenge is to convert the slow (as low as 0.1 Hz), random, and high-force oscillatory motion of ocean waves into a type of motion that is suitable for driving a conventional generator [1]. Addressing this challenge is the central idea of this dissertation. The problem is discussed in more detail in Section 1.3.

1.2. A brief overview of wave energy converters

Unlike wind energy, for which the method of harvesting is well established, a wide variety of devices have been, and are being, proposed for harnessing ocean wave energy. More than one thousand patents had been registered by 1980 [5], and the number has increased since.

In general, converting ocean wave energy into electricity is performed through five distinct steps, as described by Bull et al. [6]:

- Primary Energy Capture Device: Hydrokinetic to mechanical power conversion
- Drivetrain: Conversion of device motions into the final form of mechanical power required for driving the generator (hydraulics, shafts, bearings, gearboxes)
- Generator: Mechanical to electrical power conversion

- On-device Energy Storage: Mechanical or electrical power storage for power quality
- On-device Power Electronics: Electrical power conversion for power quality

Steps 2–5 may be grouped into one category, called the power conversion chain (PCC). Moreover, the “drivetrain-generator” pair is often referred to as the Power Take-Off (PTO) in the wave energy industry. In the case where a linear generator is used, the drivetrain and generator are not distinguishable, as such a power conversion mechanism accomplishes the aims of each of the two components in one [6].

A comprehensive study, covering all the introduced designs and neatly categorizing them into a limited number of classes, is not straightforward. Different authors have chosen different factors as criteria for classification.

WECs can be classified by their directional dependence [6]. In this case, devices fall into three main groups, namely, point absorbers, terminators, and attenuators, as shown in Fig. 1. Point absorbers can convert incident wave energy from any direction with equal efficiency and thus, are generally axisymmetric. On the other hand, terminators and attenuators are orientation-dependent and are not fully symmetric. While terminators are oriented perpendicular to the incoming wave fronts, attenuators are oriented parallel to incoming wave fronts.

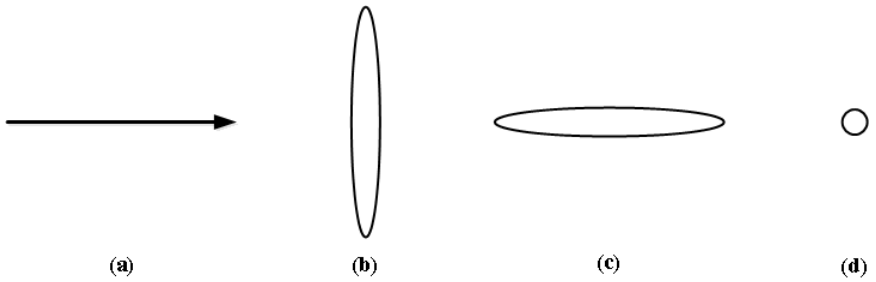

Fig. 1. An incident wave confronting three main groups of WECs based on their directional dependence. (a) incident wave. (b) terminator. (c) attenuator. (d) point absorber.

WECs can also be classified by their depth of installation. A device can be installed offshore, near-shore, or shore-mounted. These distinctions in depth usually affect the type of mooring required [6].

Falcao classifies WECs based on the method of energy conversion, into three main groups [7]. Fig. 2 presents the three groups along with their sub-groups and examples. A brief description of each type, adopted from [7], follows.

1.2.1. Oscillating Water Column (OWC)

These devices, sometimes called the first-generation devices, may have either a fixed or floating structure. "Limpet" is an example of a fixed structure OWC. This device comprises a partially submerged structure, of concrete or steel, which is open below the water surface and serves to trap the air above the free surface of water. The incident waves result in the oscillation of the internal free surface. The oscillation, in its own right, causes the air to flow through an air turbine that drives an electric generator. The employed air turbine is of the axial-flow Wells type, which is capable of rotating in a single direction regardless of the direction of air flow [7]. An off-the-shelf high-speed

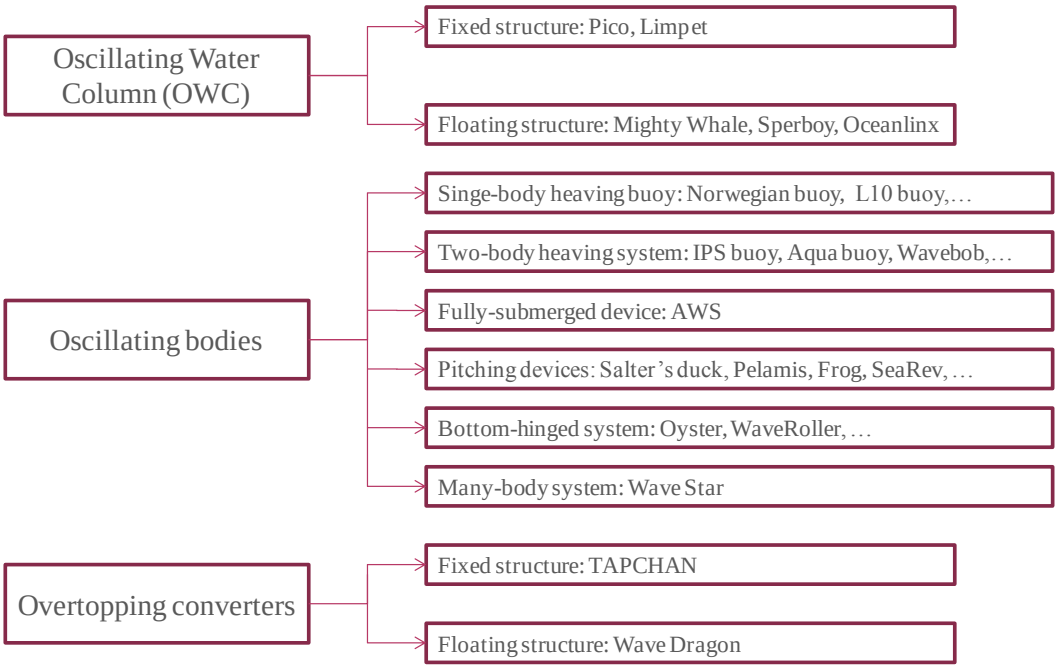

Fig. 2. Three main groups of WECs based on the method of energy conversion

rotary generator is used along with the Wells turbine. "Limpet" uses a variable speed induction generator [8].

1.2.2. Oscillating bodies

These devices take advantage of the more powerful waves existing off shore. They may be floating or, less commonly, fully submerged. The devices may also be heaving, pitching, or a combination of both. Heaving devices offer a high-force, low-speed reciprocating motion; whereas the pitching devices offer a high-torque, low-speed rotational motion [7].

Single-body heaving buoy: The simplest form of an oscillating-body device is a heaving buoy reacting against a fixed reference frame, which may be either the sea floor itself or a structure fixed to the sea floor. Often, horizontal dimensions of such a buoy

are much smaller than the wavelength; in other words, they are considered point absorbers. An example of a single-body heaving device is the L10 buoy developed at the Oregon State University. The L10 buoy consists of a deep-draught spar and an annular buoy. The buoy can heave relative to the spar, which is taut-moored to the sea bed by a cable; however, a linear bearing system prevents the buoy from moving in other directions. The relative motion of the buoy and spar exerts a force on the spar, causing it to move, and this motion is converted into electricity through a permanent magnet (PM) tubular linear generator [7].

Two-body heaving buoy: Single-body heaving buoys may suffer from problems raised due to tidal oscillations, as well as to the distance between the free surface of water and the sea bed. To address these issues, multi-body systems have been developed in which the relative motion between two bodies, oscillating differently, results in energy conversion. Two examples of two-body heaving buoys are "WaveBob" and "PowerBuoy". "WaveBob" consists of two concentric axisymmetric buoys, the inner of which is rigidly connected to a submerged body that is located sufficiently far underneath the buoys. The submerged body serves to increase inertia without reducing excitation and radiation forces. A high-pressure-oil system is employed as a part of the PTO to convert the relative axial motion of the two bodies into electric energy. In the "PowerBuoy" a disc-shaped floater moves relative to a submerged cylindrical body, rigidly connected to a large horizontal damper plate at its bottom end. Similar to the "WaveBob," the role of the plate is to increase inertia through added mass of the

surrounding water. A hydraulic PTO is adopted to convert the relative heaving motion between the two bodies into electricity [7].

Fully submerged heaving systems: The Archimedes Wave Swing (AWS) is a fully submerged device, and consists of two main parts: a "floater" which is oscillating, and a "basement" which is fixed to the sea bed. A wave crest pushes the floater down while a wave trough makes the floater move up [7]. The resultant motion is converted into electricity by a variable speed linear PM synchronous generator, rated at 2 MW peak power and 400 kW average power [8].

Many-body systems: A heaving device may consist of a large number of floating buoys reacting against a common reference frame and sharing a common PTO. An example, FO3, is a system consisting of an array of 21 axisymmetric buoys heaving with respect to a large floating structure. The system uses a hydraulic PTO [7].

Pitching devices: As opposed to the three categories presented above (in all of which the energy conversion is mainly associated with relative translational motion), in pitching devices, energy conversion is mostly associated with relative rotation. A well-known example of such devices is "Pelamis," a snake-like device consisting of four cylindrical bodies linked by hinged joints. The device is slack-moored and is placed on the ocean surface, aligned with the wave direction. The joints move due to incident waves, and their motion pumps high-pressure oil through hydraulic motors [7] which drive three fixed-speed induction generators [8]. Gas accumulators serve as energy storage.

Bottom-hinged systems: These devices are, in essence, an inverted pendulum that is hinged at the sea bed, operating in pitching mode and converting wave energy into reciprocating rotation. "Oyster," as an example, uses the sea water as fluid to propel a Pelton turbine that is located onshore. Another example of such devices is "WaveRoller" that uses oil as its working fluid to drive an onshore generator [7].

1.2.3. Overtopping devices

These devices include a reservoir that stores water at a level higher than the average free surface level when wave is at or close to its crest. The potential energy of the stored water is then used to drive a turbine. Overtopping devices have highly nonlinear dynamics and, unlike OWCs and oscillating bodies, their behavior may not be described through linearized wave models. "WaveDragon" is an example of this type of devices [7]. In this system, the low-speed water turbine is coupled to a high-pole-count variable speed rotary PM synchronous machine [8].

1.3. Making the case for the TROMAG

Although there is no general consensus about which of the WECs described above will eventually dominate the wave industry [9], some experts speculate that heaving point absorbers are the "way to go" [10]. These devices, often called buoys [11], have been promising in terms of power-to-volume ratio and have the potential for mass production [12]. Buoys offer a high-force, low-speed reciprocating translation. The case resembles wind turbines, in which a hub rotates at high torque and low speed. Therefore, first, a summary of the statement of the problem and its proposed solutions in wind

turbine industry is provided. Then, the PTOs adopted so far for buoys are presented along with their pros and cons, so that a case can be made for the TROMAG.

1.3.1. Generators for the wind turbines

The solution originally opted in wind industry for tackling the problem of high-torque and low-speed rotation was the use of a mechanical gearboxe to convert the described motion into high-speed, low-torque rotation, suitable for an off-the-shelf, high-speed rotary generator. Mechanical gears, despite being a well-established technology, proved problematic when used in this application, especially as the rating of turbines increased; in many cases, the gearbox failure has been the reason for shutting down a wind turbine [13]. Mechanical gears transmit force through mechanical contact, and, therefore, they suffer from friction and the consequent wear and tear that mandates regular maintenance. These problems are prohibitive, especially for offshore wind turbines where area of installation is costly to reach. As an alternative, a small but growing sector of wind industry adopted the direct drive technology in which the gearbox is eliminated and the generator is directly driven by the hub [13]. This approach, however, results in bulky and heavy generators because, in general, weight, volume, and cost of the active material of an electric machine are proportional to the amount of torque (force) with which it has to interact. Moreover, large size of direct drive machines necessitates large amounts of inactive material as the supporting structure for maintaining the air gap. Iron-core PM synchronous machines have generally been the choice of machine configuration in this application. Small imperfections in air gap uniformity, which stem from manufacturing tolerances, and are more likely to happen as

the machine size increases, can yield a large unbalanced magnetic pull between the rotor and stator. The supporting structure and bearings hence must be designed to withstand these additional forces as well. As a consequence, inactive material would contribute to a significant part of the whole machine weight [14].

Magnetic gears, thus, have been proposed as a hybrid solution to overcome the problems associated with mechanical gearboxes and bulkiness and heaviness of the direct drive generator systems [13], [15]-[16]. Magnetic gears transmit force through magnetic field. The contact-free force transmission is expected to afford the device advantages such as reduced wear and tear, reduced need for maintenance, increased reliability, and reduced noise. More interestingly, magnetic gears offer inherent overload protection capability: unlike mechanical gears, in which an overload can break the teeth, magnetic gears slip when overloaded [13], [17]. Such advantages have rendered magnetic gears an active and flourishing area of research today. Several types of these gears have been investigated and prototyped, namely, the magnetic cycloid gear [18], the magnetic harmonic gear [19], and the magnetic worm gear [20]. The type that has attracted the most interest, however, is the so-called field modulated magnetic gear. Fig. 3 shows 2D and exploded views of a radial flux rotary field modulated gear [13]. The radial flux rotary realization of this type of gear, in its most common configuration, consists of two concentric permanent magnet (PM) rotors and field-modulating iron pole pieces which are sandwiched between the two PM rotors. Upon using high energy density PM material, torque per active volume of these gears has reported to reach about 100 kN.m/m^3.[21]

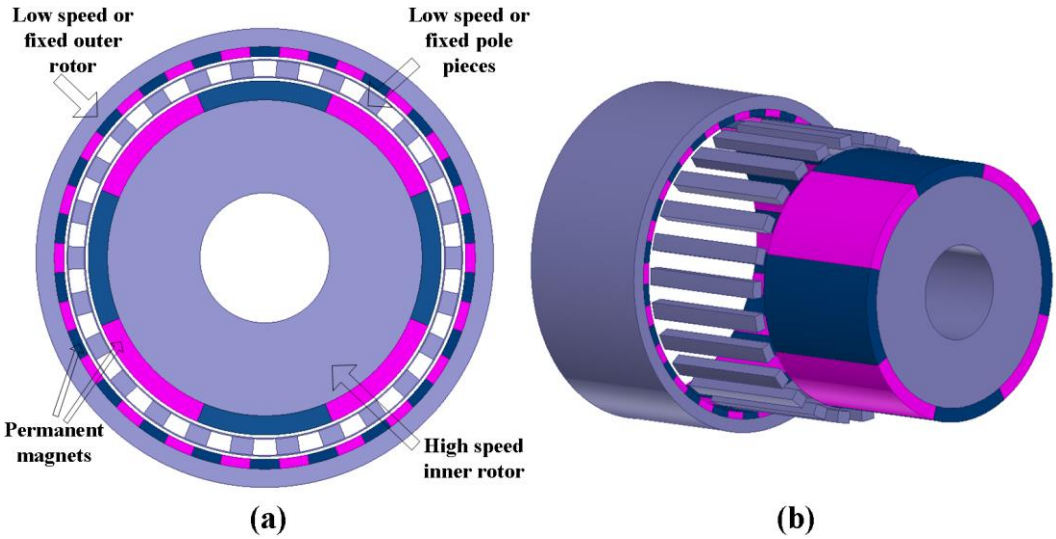

Fig. 3. A field modulated magnetic gear. (a) 2D view. (b) exploded view.

Also proposed is integration of the field-modulated magnetic gear and a PM machine to achieve a torque-dense electro-mechanical energy conversion system, the torque density of which reaches double the values common to radial-flux, liquid-cooled PM machines without jeopardizing the power factor [22]. Two possible arrangements for the integration of a field-modulated gear and a PM machine are illustrated in Fig. 4. In one possible arrangement, shown in Fig. 4(a), a surface mount PM machine is inserted into the inner volume of the field-modulated gear, and the overall system has three air gaps [23], [24]. Although the gear and the machine are mechanically coupled, a thick core may be used on the outer rotor of the gear to magnetically decouple the gear and the machine [24]. In another arrangement, shown in Fig. 4(b), the stator and coils are placed as the outermost embodiment, and the overall system has two air gaps [22].

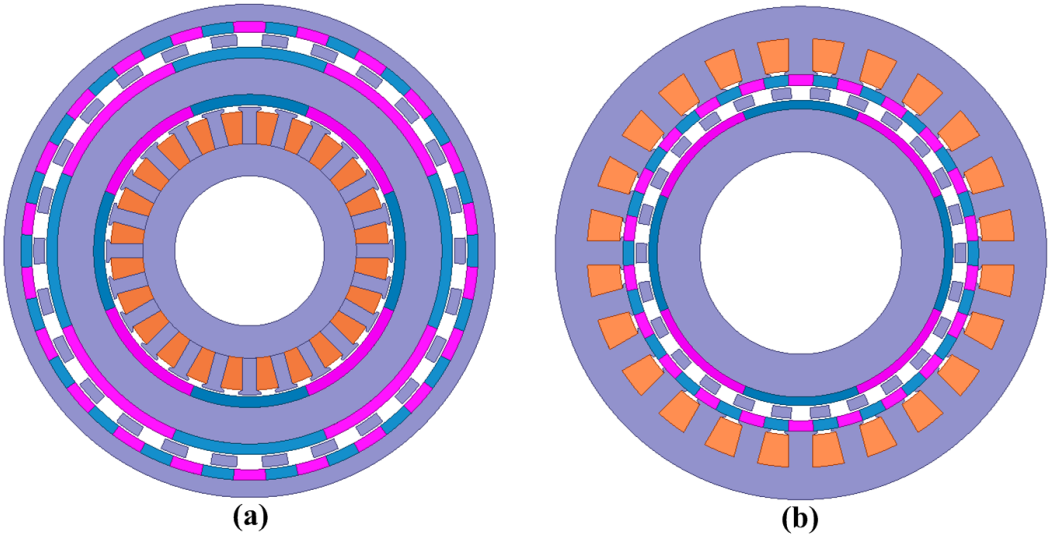

Fig. 4. Gear-integrated machine configurations. (a) inner stator. (b) outer stator.

1.3.2. PTOs for the buoys

When addressing the problem of high-force, low-speed translation of buoys, a trend similar to wind turbines can be observed. In practice, two solutions have so far been adopted, as summarized in the following two sections.

1.3.2.1. Mechanical intermediary systems

One solution is employing a hydraulic system to convert the described motion to a high-speed, low-torque rotation suitable for traditional high-speed generators. Utilizing high pressure oil affords these hydraulic systems superb force density and thus, reduced weight and size. Moreover, an accumulator or two can be used as an energy storage system [25]. However, hydraulic systems suffer from several drawbacks. They need regular maintenance and, since buoys are installed offshore, the cost of maintenance would be more than an equivalent onshore system [26]. Moreover, hydraulic seals are

generally designed for speeds lower than typical values of these WECs [27]. In addition, leakage of the sea water into the oil would degrade the system performance, while contamination of the sea due to the oil leakage is another concern [28]. Furthermore, axial displacement hydraulic systems offer low efficiency at partial loads [8]. Given the highly variable nature of the sea state, acceptable efficiency over a wide range of operation is highly desired. Another point to consider is that wave industry uses components of a hydraulic system in role reversal: in wave energy conversion application, a hydraulic system is driven by a low-speed linear motion and drives a high-speed rotary generator. On the other hand, in common industrial applications, rams are typically used as actuators that displace the hydraulic fluid at high pressure, and a high-speed motor is used to create rotational motion [25]. Traditionally, the mechanical interface required to convert low-speed motion to high-speed rotation suitable for conventional high-speed generators has been considered as an area that needs further research [28].

1.3.2.2. Direct drive linear machines (DDLMs)

To eliminate the problematic mechanical interface and its associated maintenance needs and losses, direct coupling of a linear machine to a buoy was proposed. The direct drive system has fewer moving parts and a more robust structure, thus expected to have higher efficiency, need less maintenance, and offer higher reliability [8]. The employed machine, however, has to operate at the same speed as that of the buoy, that is, typically 0.5 to 2 m/s [8], and resist a high force. As an example, a 100 kW buoy translating at 1 m/s exerts 100 kN force on the machine. With 20-40 kN/m^2 being a typical value for the

tangential shear stress of conventional linear machines [8], an active area of about 5 m^2 would be required.

Polinder et al. modeled, optimized, and compared five linear machine configurations to be used with the AWS [29]. Induction machines with and without iron in the translator, switched reluctance machines, and iron-core and air-core surface mount PM synchronous machines were considered. The study concluded that an iron-core PM is the optimum choice in terms of required active material and efficiency. They also built a flat, double-sided, linear surface-mount PM machine rated at 2 MW peak power for the AWS [30]. The machine is shown in Fig. 5 [8]. The design was performed for 2 m/s speed and therefore, 2 MN peak force; hence, the resultant machine was extremely heavy, bulky, and expensive. This machine is the only MW scale of its type; however, it is no longer operational [26].

Fig. 5. The flat, double-sided linear PM machine built for the AWS (Copyright 2007 by IEEE)

Another example of a direct drive system is a PM linear tubular machine (LTM), designed, built, and tested at the Oregon State University [31]. The machine has no moving, sliding, or rotating seawater seals, and uses seawater as the lubricant for a stainless steel sliding bearing system. Pictures of this machine are depicted in Fig. 6.

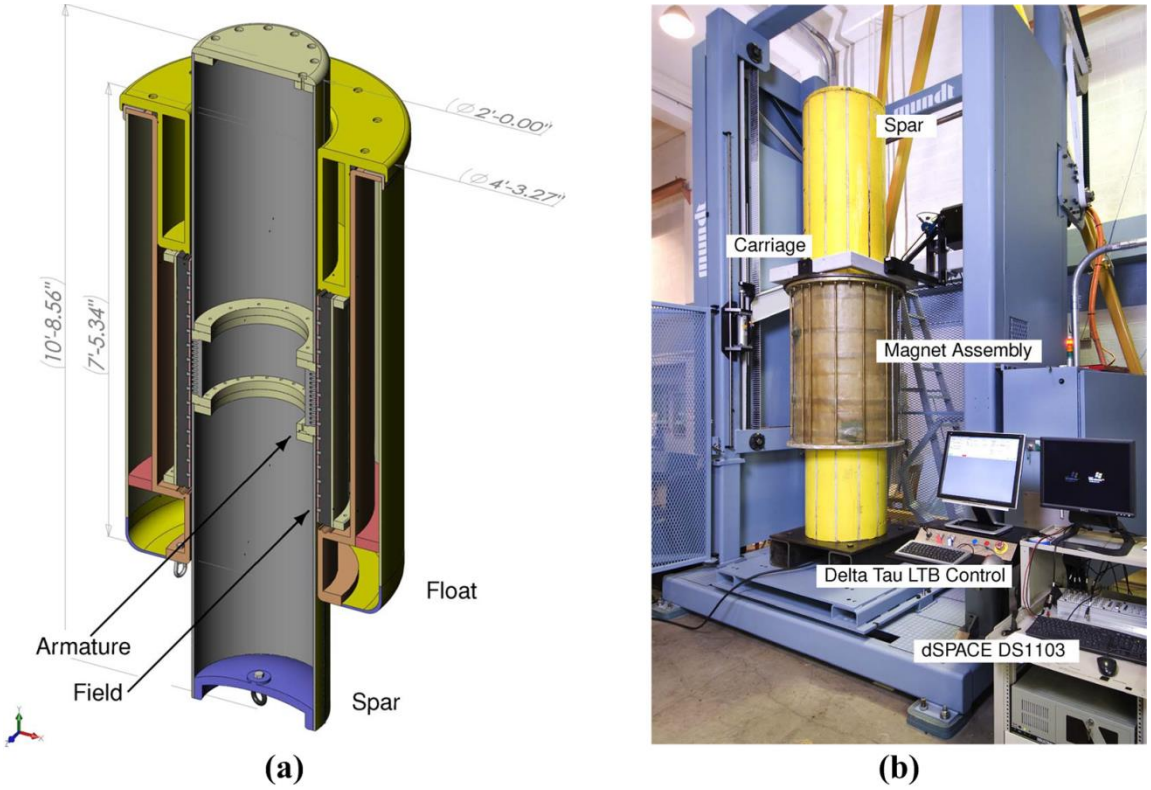

Fig. 6. The PM LTM built for L10 buoy at OSU (Copyright 2010 by IEEE)

Similar to direct drive wind generators, DDLMs used for utility scale buoys turn out to be very bulky and heavy. To address this issue, some researchers have suggested to depart from conventional machine configurations and resort to the class of Variable Reluctance PM Machines (VRPMs) [27]. The Transverse Flux PM Machine (TFPM),

which may be considered the ultimate VRPM [25], is reported to exhibit tangential shear stress of about 200 kN/m^2, an order of magnitude higher than the conventional machines [32]. TFPMs, however, suffer from complexity of structure, essentially a 3D flux path that prohibits the use of iron laminations, large cogging force, reportedly as high as 30 kN/m^2 [25], and poor power factor. Another type of VRPM is the so-called Vernier Hybrid Machine (VHM), which accommodates both copper and magnets on a stator, and its translator is just a toothed iron core [25], [33]. Although the tangential shear stress of a VHM is lower than a TFPM, it has a simpler structure; specifically, the stator can be made by laminations. VHMs still suffer from a poor power factor; one is reported to offer a tangential shear stress of 120 kN/m^2 at 30% power factor [33]. In order for a VHM to offer competitive shear stress, its air gap should be kept small, roughly below 1 mm, and this is difficult when the translator is several meters long [8]. When the air gap length is increased, the magnet pitch should be increased as well to prevent excessive flux leakage. A VHM with increased magnet pitch attains to a conventional PM machine and tends to lose its superior shear stress [8].

Another issue with the iron-core linear machines discussed above is an attraction force between the stator and translator; the so-called closing gap force. This force, similar to the case of direct drive wind generators, arises from the air gap non-uniformity caused by manufacturing tolerances. The attraction force may be 5–10 times the tangential shear stress [27]. To tackle this problem, one proposed solution has been to remove iron from either the stator or translator, usually the part that is stationary [25]. Removing the iron core, however, results in a significant reduction in the shear stress,

down to the 10 kN/m^2 region [34]. Another proposed solution has been the so-called C-Gen, which offers a shear stress larger than an air-core machine, but still lower than a conventional iron-core PM machine, while ideally exhibiting zero closing gap force [34].

Similar to the case of wind turbines, field-modulated magnetic gears have been proposed as a hybrid solution for buoys as well [35]. Fig. 7 shows a gear of this kind [36]. Similar to the rotary counterpart, two possible arrangements exist for integrating a linear gear into a linear machine [35], [37]. The force density achieved by these configurations has been reported to be roughly twice the values common to conventional linear PM machines. Although the boost in force density is noticeable, these configurations still result in large machines because of large forces with which they need to interact. The structure is also complex.

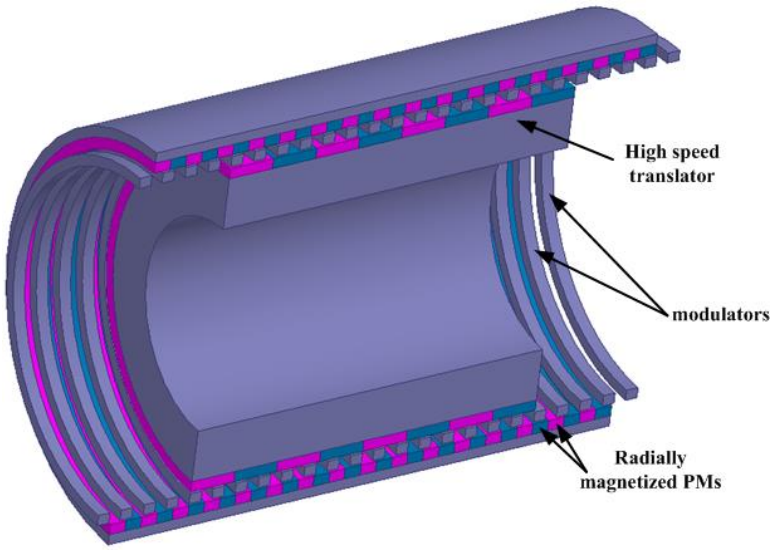

Fig. 7. Cut-away view of a field-modulated linear magnetic gear

1.3.3. Proposed solution: TROMAG

In pursuit of a linear machine configuration with significant shear stress, simple structure, and high power factor, this dissertation proposes a different pathway: a magnetic device, referred to as the Trans-Rotary Magnetic Gear (TROMAG). The idea is to use the TROMAG as an intermediary stage to convert the high-force, low-speed translation of a buoy into a low-torque, high-speed rotation such that a conventional high-speed rotary machine can be employed. As opposed to hydraulic systems or mechanical gears, the TROMAG, as a type of magnetic gear, would offer contact-free force transmission and, therefore, inherent overload protection capability along with high reliability and high efficiency. In addition, by using high energy density magnets, the TROMAG can easily reach an axial shear stress in the region of 200–300 kN/m^2 which yields a lightweight and compact device. It will be shown that for a high-force, low-speed load characteristic, the system consisting of a TROMAG and a rotary machine would use much less active material, compared to a DDLM that is designed for the same force and power.

1.4. Outline of the dissertation

In Chapter 2, structure of the TROMAG is presented as well as its historical background and principles of operation. It is shown how the device can be deduced from elementary magnetic arrays and how an analogy can be set forth between the TROMAG and conventional rotary and linear machines. Chapter 3 discusses aspects of magnetic design of the TROMAG and compares the system comprising a TROMAG and a rotary machine with a liner tubular PM machine in terms of cost, weight, and volume of the

active material. Chapter 4 studies dynamic behavior of the TROMAG. In this chapter, a nonlinear analytical model is proposed for describing the dynamics of the device. The model is then linearized and combined with that of a buoy. In this way, dynamics of the entire energy conversion system can be studied. Chapter 5 reports on prototyping a TROMAG and presents static force measurements as well as oscillation test results. Chapter 6 summarizes the highlights of the work and concludes the dissertation by suggesting paths for future research.

2. PRINCIPLES OF THE TROMAG*

2.1. Introduction

This chapter introduces the TROMAG. First, the structure of the TROMAG is presented and it is observed that the TROMAG can be looked upon as a pair of either rotating or translating arrays of alternating polarity magnets. Principles of operation of the TROMAG and how it exhibits a gearing effect are discussed, and force and torque characteristics of the device are presented. Then it is shown how the TROMAG can be developed from elementary arrays of magnets.

2.2. Structure

Fig. 8 depicts different views of a 2-pole TROMAG, specifications of which are given in Table 1. Both the rotor and translator are made of ferromagnetic iron cores, covered by radially magnetized, helically disposed, alternating north and south PM poles. Blue and pink colors indicate north and south poles. The ferromagnetic cores provide structural support for the magnets and improve the force capability of the device.

---

* Part of this section is reprinted with permission from

"Principles of the Trans-Rotary magnetic Gear" by S. Pakdelian, N. W. Frank, and H. A. Toliyat, *IEEE Trans. Magn.*, vol. 49, no. 2, pp. 883-889, 2013. Copyright 2013 by IEEE.

"Analysis and design of the Trans-Rotary magnetic Gear" by S. Pakdelian, N. W. Frank, and H. A. Toliyat, in *Proc. 2012 IEEE Energy Convers. Congr. Expo. (ECCE), pp*. 3340-3347. Copyright 2012 by IEEE.

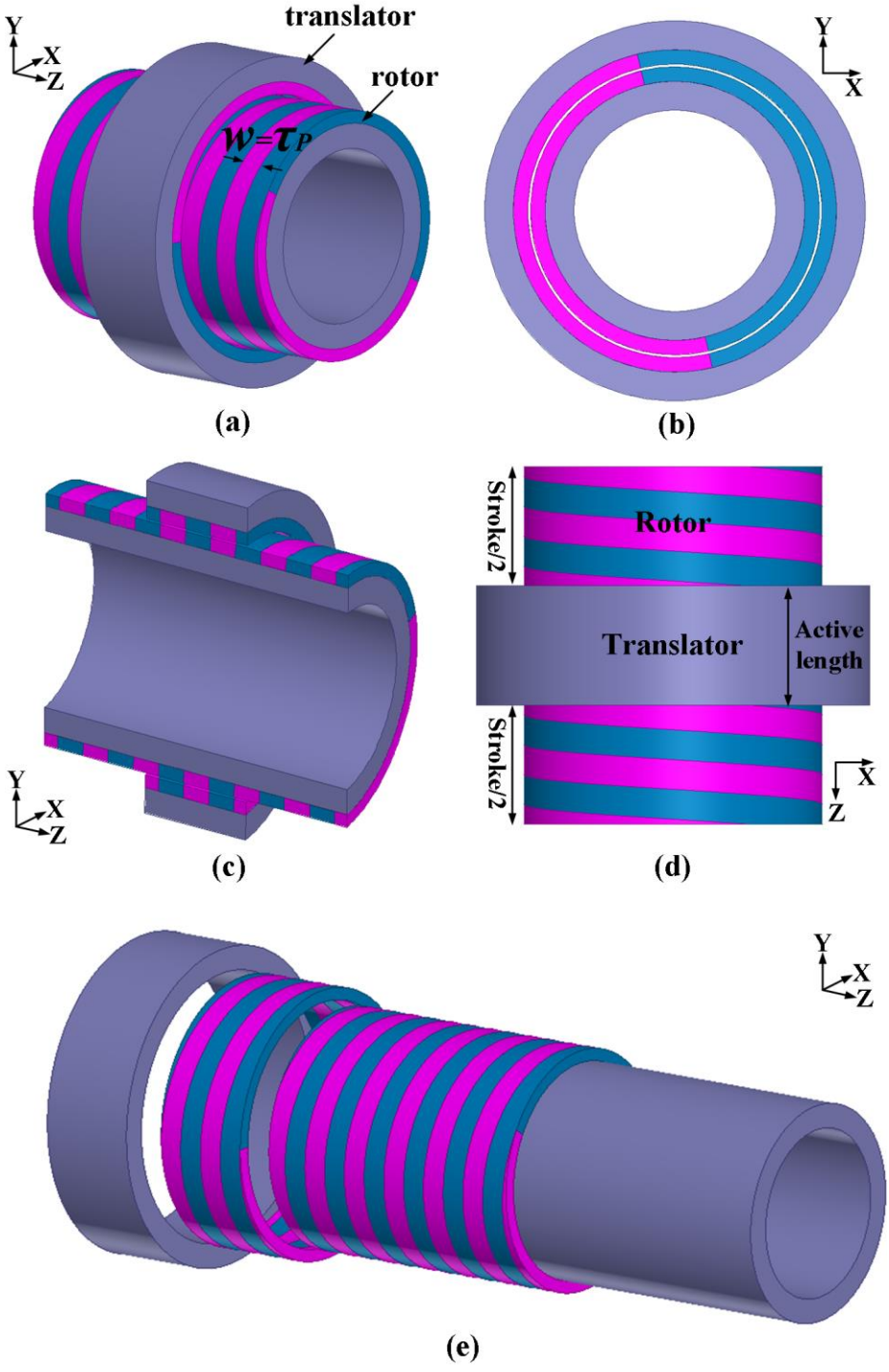

Fig. 8. Views of a 2-pole TROMAG. (a) 3D view. (b) front view. (c) cut-away view. (d) top view. (e) exploded view.

Table 1. Design specifications of the TROMAG of Fig. 8

Quantity	Value
Magnet thickness on translator and rotor	5 mm
Magnet width	10 mm
Magnet coercivity	838 kA/m
Magnet remanent flux density	1.1 T
Outer radius of the rotor including PMs	50 mm
Air gap length	1 mm
Active length	40 mm
Core material	Steel 1020

The front view of the TROMAG, shown in Fig. 8(b), looks like two concentric rotors, each having two PM poles. The side view, depicted in Fig. 8(c), resembles two translators lined up with alternating polarity ring magnets.

The TROMAG consists of two main parts: a rotor and a translator. While the translator moves back and forth along the Z-axis, the rotor rotates about that axis. One of the two parts has to be longer than the other one, so the magnets remain engaged as the translator moves. Length of the shorter part is referred to as the active length of the device, while the extra length added to provide the engagement is called the stroke.

The TROMAG can be used in both motoring and generating applications. In a generating system like a WEC, the translator is coupled to a prime mover, for example, a buoy, and the rotor is coupled to a rotary generator. As the buoy heaves, the translator reciprocates, causing the rotor to rotate and drive the rotary generator. In the motoring mode, the rotor is coupled to a rotary motor and the translator is coupled to the load to be moved, for example, a reciprocating pump. The motor rotates the rotor. As a result of this rotation, the translator moves and propels the load. A given system can keep switching between the two modes of operation.

In Fig. 8, the outer part is identified as the translator, and the inner part is identified as the rotor; whereas, in general, either of the inner part or outer part could serve as a rotor or translator. In fact, the rotor is the part which is mechanically kept from translation, and the translator is the part which is mechanically kept from rotation. The application in which the TROMAG is employed would determine which option to choose.

The device resembles a lead-screw system and may be considered as a magnetic dual of the mechanical lead-screw. However, the name "Trans-Rotary Magnetic Gear" is chosen instead of names such as magnetic screw [38], or magnetic lead screw [39], to emphasize the gearing capability of the device and to categorize it as a type of magnetic gear. Moreover, the name indicates the presence of both rotation and linear motion in the device.

2.3. Principles of operation

2.3.1. Gear ratio

To understand the gearing action of the TROMAG, Fig. 9 displays an example of a 12-pole TROMAG. During steady state, the rotor and translator move in synchronism. As the translator moves one pole pitch, the rotor also rotates one pole pitch. However, the pole pitches of the rotor and translator are different: the rotor pole pitch is in an angle unit, whereas the translator pole pitch is in a length unit. The mismatch in the pole pitches can be translated into the so-called gearing effect. Intuitively speaking, when the translator pole pitch is short and the rotor pole pitch is large, a small displacement of the translator would result in a large rotation of the rotor. A gear ratio may then be defined

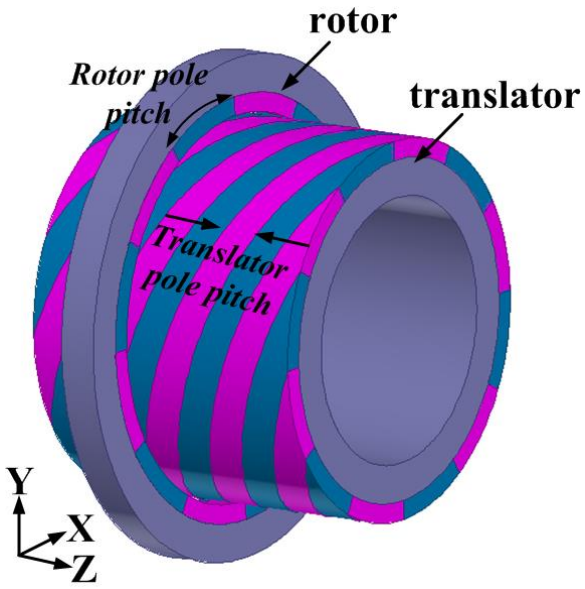

Fig. 9. A 12-pole TROMAG

as the ratio of rotor angular speed, ω, to the translator linear speed, v. Suppose P denotes the number of (rotor) poles as viewed from the XY plane (which equals 12 in Fig. 9) and τ_P denotes the translator pole pitch. Since the translator moves at the speed of v m/s, the number of translator pole pitches that it would traverse during 1 second is equal to v/τ_P. During that time period, the rotor would traverse the same number of its own pole pitches. Therefore, the rotor speed in terms of revolutions per second would be:

$$n = v/P\tau_P \tag{1}$$

Thus, the gear ratio is obtained:

$$G = \frac{\omega}{v} = \frac{2\pi n}{v} = 2\pi/P\tau_P \tag{2}$$

From (2) it is deduced that two factors determine the gear ratio: the number of (rotor) poles and the translator pole pitch. The lower the number of poles and the

narrower the pole pitch are, the higher the gear ratio will be. In a mechanical screw, by definition, the "lead" is the distance the screw traverses as the nut rotates one turn. Hence, the product $P \times \tau_P$, determining the gear ratio in the TROMAG, is equivalent to the lead of a mechanical screw. As an example, a 2-pole TROMAG with 10 mm translator pole pitch has 20 mm lead and can convert a linear speed of 1 m/s to a rotary speed of 3000 rpm. A 12-pole TROMAG with the same specifications would have a 120 mm lead and can convert a 1 m/s linear speed to a 500 rpm rotation.

The relation between the translator force, F_t, and the rotor torque, T_r, can be simply obtained by assuming an ideal TROMAG in which the power associated with the translator motion, P_t, equals the power associated with the rotor rotation, P_r, as shown in (3).

$$P_t = P_r \Rightarrow F_t v = T_r \omega \Rightarrow \frac{F_t}{T_r} = \frac{\omega}{v} = \frac{2\pi}{P\tau_P} = G \tag{3}$$

Notably, the gear ratio would better be defined as $G = F_t/T_r$ instead of ω/v because the former definition holds in all operating conditions as long as the helices are ideal; whereas, in a TROMAG with non-unity efficiency or during transient states, the relation between ω and v may not simply be a proportionality factor. However, the latter definition provides an intuitive way of understanding the device operation as explained above.

2.3.2. Force and torque characteristics

When the translator is kept stationary and the rotor is rotated 360 electrical degrees (which corresponds to 360 mechanical degrees rotation for a 2-pole TROMAG), or when the rotor is kept stationary and the translator is moved by two translator pole

pitches, then the characteristics of the rotor torque and translator force (along with its central axis) would be obtained. The curves shown in Fig. 10 correspond to the TROMAG of Table 1, and are obtained by three-dimensional (3D) finite element analysis (FEA). Several points are worthy of notice regarding these characteristics:

- The torque and force characteristics resemble torque and force characteristics of rotary and linear synchronous machines, respectively. Accordingly, the peak values may be called pull-out torque and pull-out force, respectively.
- The pull-out force is about 2.9 kN. With the given air gap radius and active length, the pull-out force per active area, which is referred to as the (axial) shear stress, turns out to be about 230 kN/m^2. Given that the axial shear stress of conventional linear machines is within the range of 20-40 kN/m^2, the TROMAG offers a force density an order of magnitude higher than those machines.
- The FEA simulation is not performed on a TROMAG with ideal helix; rather, each turn of a helix is replaced by 120 pieces of magnet, each having an arc of 3 degrees. Using a lower number of magnets for approximating an ideal helix would affect the characteristics. The influence is studied in Chapter 3.
- Notably, the rotor torque and translator force characteristics are 180 degrees apart. In other words, the gear ratio is negative. This is due to the fact that the simulated TROMAG, as seen in Fig. 8(a) and Fig. 8(d) has a left-handed helix; that is, as the helix rotates in a clockwise direction, it moves toward the viewer. The characteristics for a right-handed helix TROMAG are shown in Chapter 4.

- The points at which the torque and force are zero are called the equilibrium points. The number of equilibrium points of a TROMAG equals its number of poles. The concept of equilibrium point is further discussed in Chapter 4.

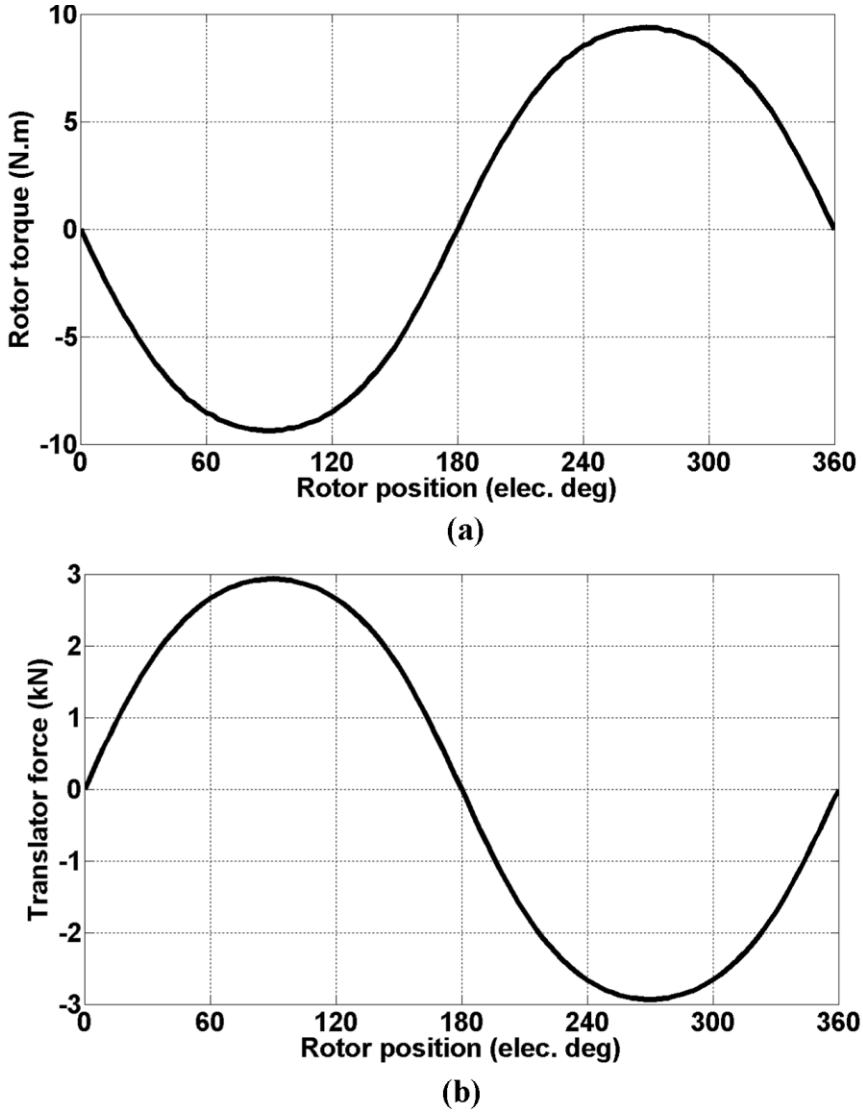

Fig. 10. Characteristics of the 2-pole TROMAG of Table 1. (a) rotor torque. (b) translator force.

2.4. Historical background

So far, the tenets of the TROMAG have been set forth. The idea of employing a helical structure in an electro-mechanical energy conversion system, however, is not recent and may be traced back to more than a century ago. In the following, a brief review of the most relevant ideas is given.

A United States patent dating back to 1912 reveals a "reciprocating motor" for drilling and pumping applications [40]. In the proposed system, a schematic of which is shown in Fig. 11, the ferromagnetic moving object, on which a thread is grooved, exhibits rotational and translational motions simultaneously as it interacts with the magnetic field of a winding.

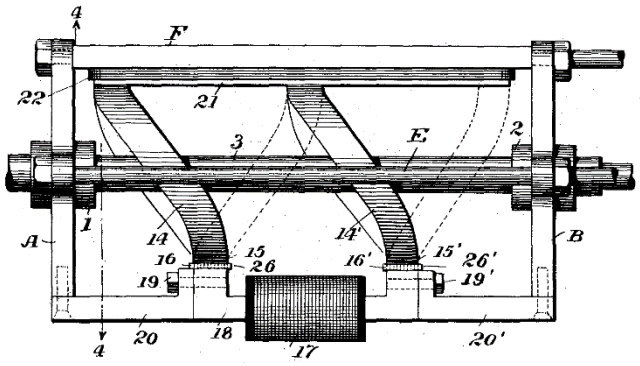

Fig. 11. A reciprocating motor

In [41], a "magnetic screw," depicted in Fig. 12, is driven by a rotary machine through a worm gear. Two sets of windings are employed, along with two sets of cores with opposite thread directions to convert unidirectional rotation of the motor to a reciprocating motion.

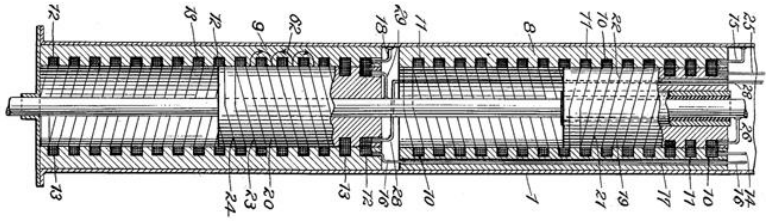

Fig. 12. A magnetic screw

The “magnetic transmission” device presented in [42] seems to be the first to use permanent magnet (PM) material for converting translation to rotation. The apparatus, the inventor of which had already patented a magnetic spur gear, was proposed as a gauge for measuring the liquid level in a tank. The device, shown in Fig. 13, consists of a short outer translator, moving up and down with the liquid level, and a long inner rotor, attached to a pointer rotating against a graduated dial. The term “magnetic gearing” was used in the patent to show that a small displacement of the translator can result in a large rotation of the rotor.

Several similar attempts were also made during the 1970s, the purpose of most of which was to create linear motion from a rotating magnetic field. In the absence of commercially viable high energy density permanent magnets, they all chose to take advantage of the reluctance variation originating from a helical structure. Gerrard and Paul developed the “recti-linear machine” [43]. The proposed machine was, in essence, a linear reluctance machine. The stator was of the rotary machine type, inside of which a thread of square cross-section was grooved. The translator was a cylinder made of mild steel on which were cut slots of square cross-section orthogonal to the displacement axis.

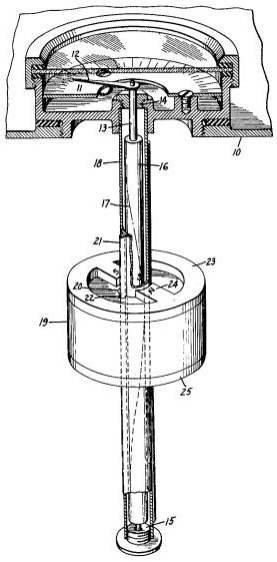

Fig. 13. A linear to rotary magnetic transmission device

The motivation at the time was to create precise linear movements. Two prototypes with different air gaps were built and test results along with analysis were presented.

Later, in 1978, Dawkins and Rhodes developed an electromagnet rotary-to-linear coupler with the aim of producing linear motion from rotation [44]. The coupler consists of two parts: a rotating inner part called the screw, and a linearly moving outer part called the track. The screw is a ferromagnetic iron rod with a double helix grooved on it while the track is a toothed structure with slots which are either straight or skewed. By exciting a coil wound inside the dips of a drilling bit, alternating north and south poles would be created on the peaks of the drilling bit. When the aforementioned bit is inserted inside a toothed structure, the tendency of the flux to travel through the minimum reluctance path would convert rotation to linear motion.

In [45], Paul proposed a system to convert rotation to linear motion and vice versa. The rotating inner part was a ferromagnetic iron rod with two rectangular PMs covered by pole shoes on which threads were grooved. The moving outer part was a mild steel sleeve with threads on the inner face.

Later, an energy conversion system was introduced to convert rotary torque to axial force [46]. In that patent, a magnetic screw and nut system was integrated into a PM machine to convert the rotation of the rotor of that machine to a reciprocating motion. The motion was used to actuate a pump for an artificial heart application [47]. The magnetic screw and nut system used in [46] is, in essence, similar to the system proposed in [45], but the peaks and dips on the two parts are replaced by north and south PMs.

In parallel with the research presented in this dissertation, two other research centers have been pursuing a similar idea. In [38], Wang et al. set forth an analysis method, based on a field solution, to calculate the thrust force of the magnetic screw and nut system proposed in [46]. The model is similar to that of a PM LTM [48]. The results, presented for a particular set of parameters, are in very close agreement with the 2D and 3D FEA calculations. Also integrating the system with a winding, similar to [46], is proposed as a method of achieving high force density linear actuator. The paper, nonetheless, does not present any other results. In [49], the same device is called "Magnetic Lead Screw" (MLS) and design and manufacture of a 17 kN prototype has been reported. The paper presents a discussion comparing the force density of an MLS with a rotary magnetic coupling as well. Moreover, the authors have performed a

structural analysis to determine the amount of rotor deflection caused by the attraction force arising from eccentricity.

This dissertation deals with the same concept, that is, magnetically converting linear motion to rotation and vice versa. However, it starts from an elementary system and provides a basic understanding of continuous force transmission between two arrays of skewed magnets, moving in orthogonal directions. With that in mind, it becomes possible to relate the skew degree of the magnets to the number of poles and, consequently, to the rotor torque. Also the active length could be considered analogous to the stack length in conventional rotary electric machines in terms of torque production, or analogous to the active length in conventional linear machines in terms of force production.

2.5. Deriving the TROMAG from elementary magnet arrays

The original goal of this dissertation has been to devise a magnetic gear which, in addition to gearing capability, could convert linear motion to rotation. To that end, the problem was first simplified to conversion of the linear motion of an array of magnets to the linear motion of another array of magnets in an orthogonal direction. The solution to this problem and how it led to the TROMAG is outlined in this section.

2.5.1. A basic system

A basic system consists of two simple arrays of alternating magnets backed by ferromagnetic iron cores, and separated by a small air gap as depicted in Fig. 14. The top array is called the rotor and the bottom one is called the translator because they will later be converted to the rotor and translator of the TROMAG. The basic system is set forth to

study the possibility of continuous force transmission in orthogonal directions. To do so, the translator is kept stationary and the rotor is moved along the Z-axis at a constant speed (or the rotor may be kept stationary while the translator is moving along with X-axis). In a synchronous machine, when one of the rotating fields is kept stationary while the other one is rotating, there would ideally be sinusoidal torques of the same frequency exerted on both the rotor and the stator. Analogously, in the basic system, alternating forces of the same frequency would be expected on the two parts when the system is capable of transmitting a non-zero average force in steady state operation. The 3D FEA simulation results, shown in Fig. 15, reveal that moving the two parts of this system in orthogonal directions causes a ripple force only.

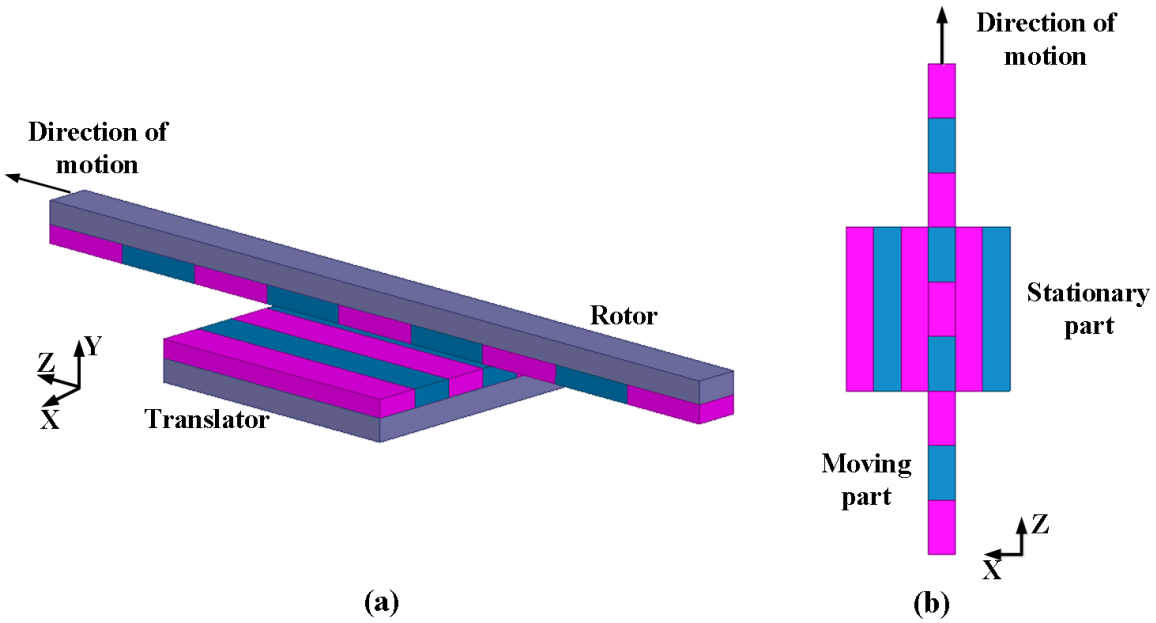

Fig. 14. A basic system. (a) 3D view. (b) 2D view with cores removed.

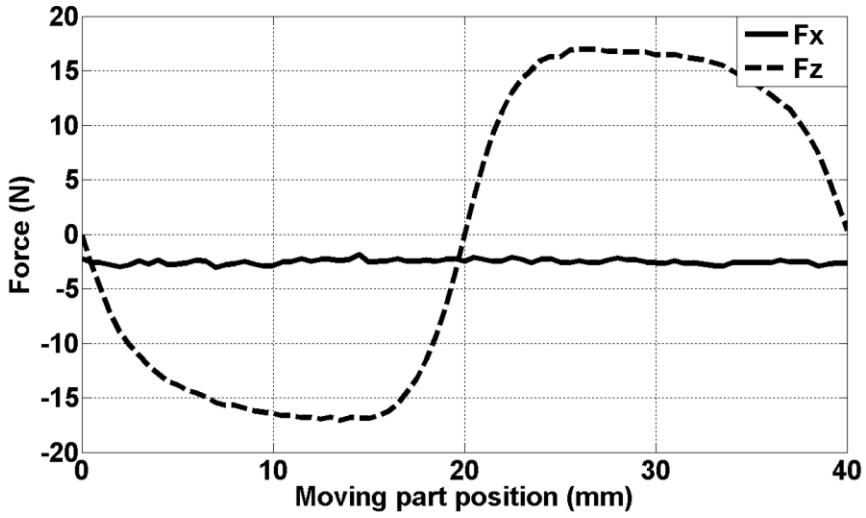

Fig. 15. Rotor force in Z direction and translator force in X direction as the translator is stationary and the rotor moves in Z direction in the basic system of Fig. 14.

However, when the magnets are skewed in the same direction, as illustrated in Fig. 16, the resultant system exhibits an interesting characteristic: the system can reach an equilibrium point, in which no force is exerted on either of the arrays, by either motion of the rotor along Z-axis or by motion of the translator along the X-axis. Such a characteristic implies that the two arrays can continuously transmit force when they move synchronously in the X and Z directions. Fig. 17 shows the force profiles of the two arrays as the rotor moves in Z direction and the translator is stationary. The two arrays have sinusoidal force profiles of the same frequency, a verification of the system's capability to transmit force in orthogonal directions. Another interesting point to notice is that when the skew angles are exactly the same, as is the case in Fig. 16, the relative positions of all north and south poles of the overlapping regions of the two moving parts remain constant as the rotor moves in the Z direction and the translator

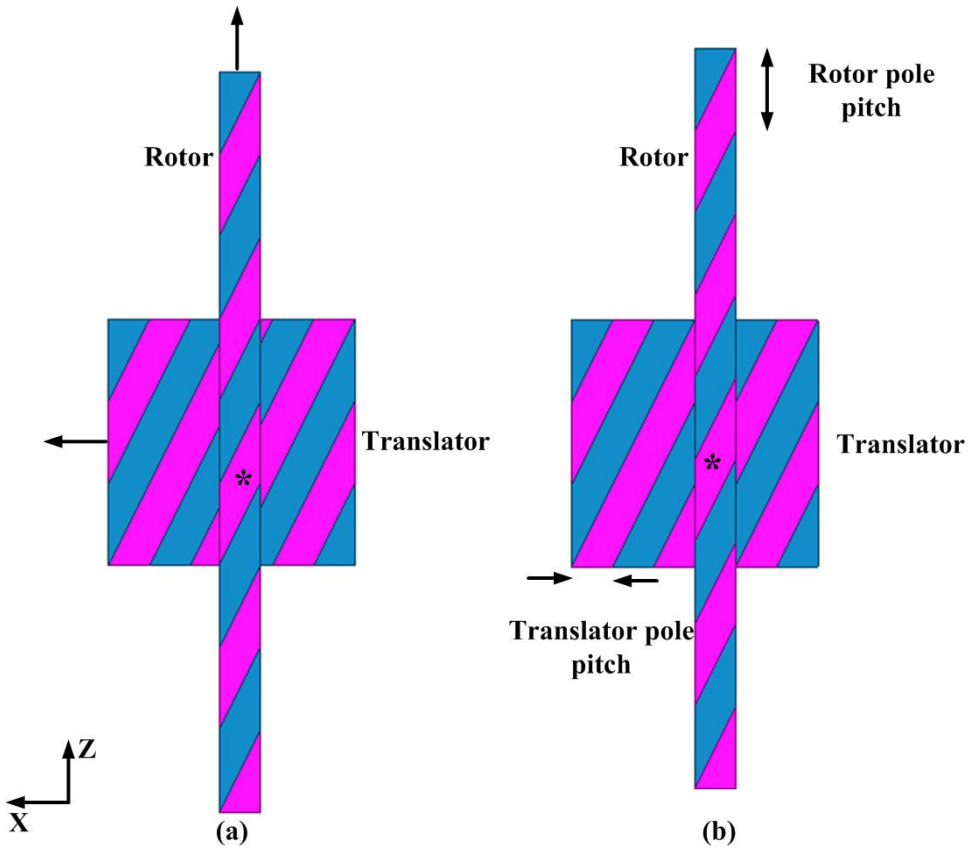

Fig. 16. Top view of the basic systems with skewed PMs. (a) initial position. (b) with rotor moved in Z direction and translator moved in X direction.

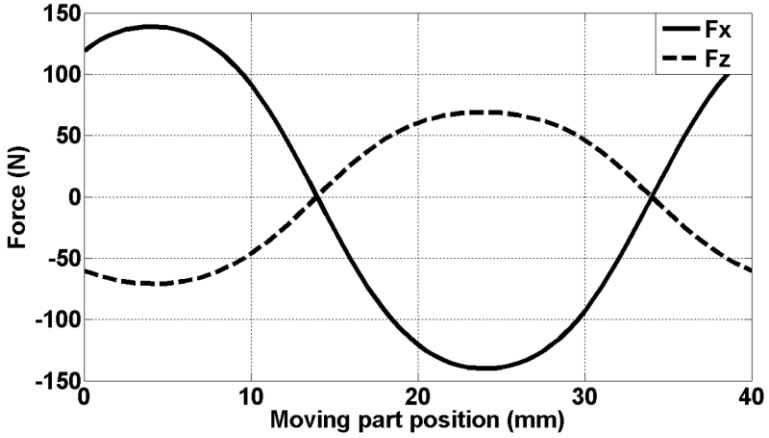

Fig. 17. Forces on the rotor and translator of the system of Fig. 16 as the translator is stationary and the rotor moves in the Z direction.

moves in the X direction. In Fig. 16(a), the basic system is in an arbitrary initial position. Fig. 16(b) depicts the same basic system in which the rotor is moved by 6 mm in the Z direction and the translator is moved by 3 mm in the X direction. For example, when the rotor magnet marked with an asterisk is considered in both Fig. 16(a) and Fig. 16(b), its position relative to the pink and blue magnets of the translator is exactly the same. Such a characteristic indicates that the system can transmit the force without any ripple.

More interestingly, since the two arrays move in different directions, their corresponding pole pitches could be different. It means that in order to maintain the synchronism between the two arrays, that is, to maintain relative positions of the magnets of the rotor and translator constant, the amount of required displacement by rotor in response to any displacement of the translator depends on the ratio of the pole pitches of the rotor and translator. This phenomenon essentially leads to the concept of gear ratio. In the demonstrated case, the rotor pole pitch is twice that of the translator, and accordingly its force is one half that of the translator.

Finally, rolling the rotor and translator about the X-axis yields a TROMAG with left-handed helix in which F_Z is analogous to the rotor torque and F_X represents the translator force.

2.5.2. The effect of the number of poles

The apparent question at this stage is what the skew angle should be. Shown in Fig. 18 are four similar basic systems with skew angle being the only difference. When a certain length of the rotor is considered, as shown by the black arrows on the four cases of Fig. 18, it is observed that the number of pole pitches fit into that length depends on

the skew angle. By rolling the two parts and shaping the TROMAG, the number of pole pitches fit into the length of $2\pi R$ of the rotor will translate to the number of poles. In analogy with mechanical screws, the number of poles can be interpreted as the number of starts of a helix.

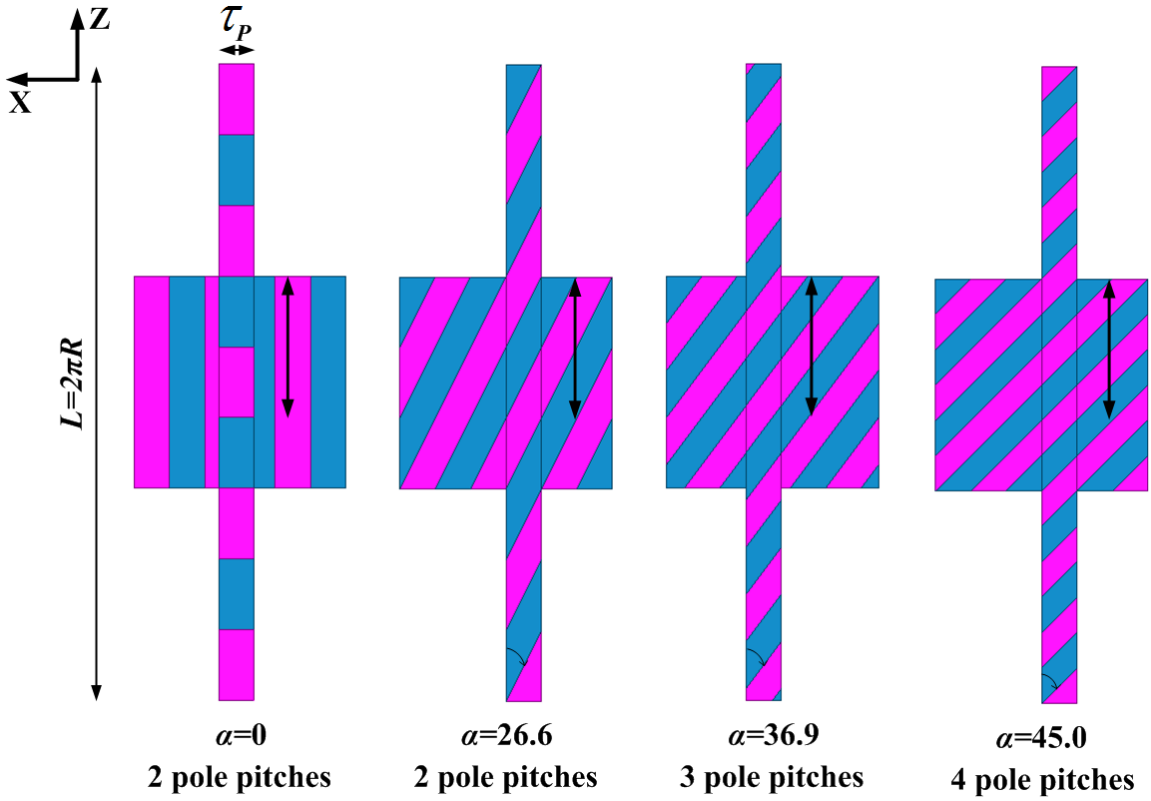

Fig. 18. Skewed basic systems with different degrees of skew.

To obtain the force profiles shown in Fig. 19, the translator is kept stationary and the rotor is moved by 40 mm, which is equivalent to two pole pitches of the rotor of the 2-pole system. Results illustrate the impact of skew angle, the number of poles in other words, on the amplitude of force profiles, as well as the number of full cycles completed.

The 4-pole system completes two full cycles because its pole pitch is one-half that of the 2-pole system.

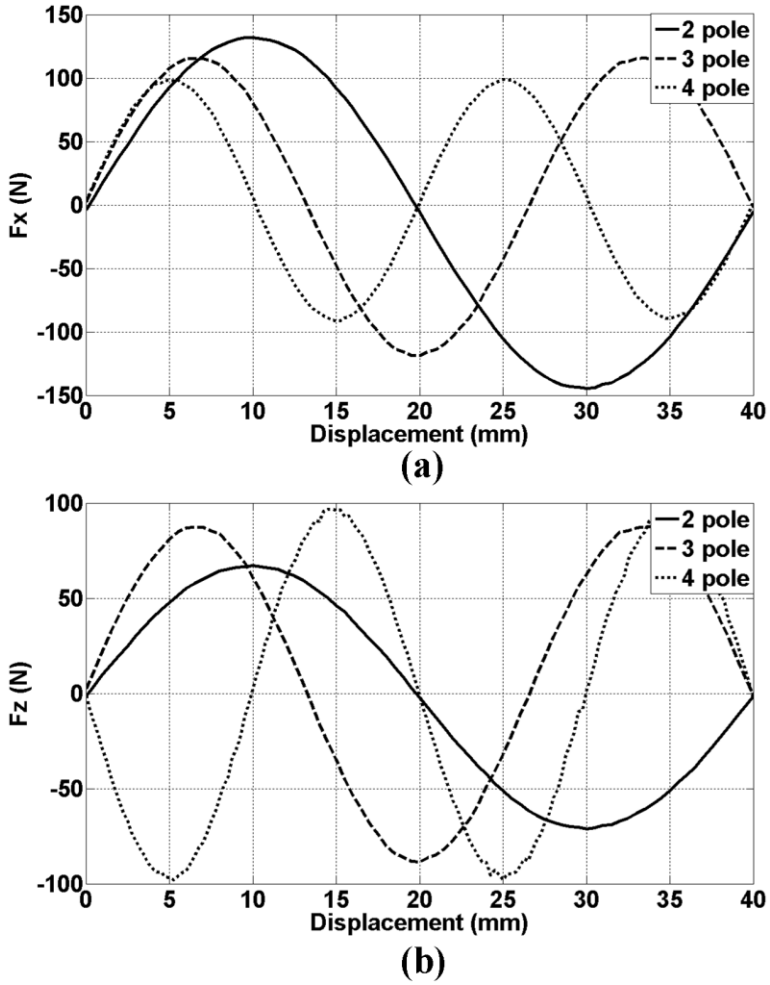

Fig. 19. Forces on the arrays of Fig. 18 as the translator is stationary and the rotor moves in Z direction. (a) translator force in X direction. (b) rotor force in Z direction.

It must be emphasized that the open-ended structure of the basic system has a noticeable impact on the basic system behavior. As the rotor moves, the system configuration at the two ends of the translator changes. However, such an "end effect"

does not exist in a TROMAG because it has a closed structure. Therefore, the TROMAG is not expected to follow exactly the same trends as the basic system, although some rules still apply.

Fig. 20 shows TROMAGs with different number of poles, namely, 2, 4, and 8 poles. For further clarity, only the inner parts are shown. Although the front views clearly indicate the number of poles, similar to Fig. 8(b), when cut-away views are considered, similar to Fig. 8(c), no distinction can be made between the TROMAGs with different number of poles. Notice that in all the three cases, the helices are discretized by 3° arc blocks of PM. Numbers common to all designs are the same as those given in Table 11. The torque characteristics, given in Fig. 21, are obtained by keeping the translator stationary and rotating the rotor 360 electrical degrees (360, 180, and 90 degrees for 2, 4, and 8-pole systems, respectively). The force profiles are practically the same for all cases; the rotor torque, however, is proportional to the number of poles. This observation verifies that the TROMAG can be looked upon as shown in both Fig. 8(b) and Fig. 8(c): in a system of two concentric PM rotors, the torque on each rotor is linearly proportional to the number of poles as viewed from the front (when non-ideal effects such as iron saturation and leakage are neglected). On the other hand, in a system of two concentric translators, the axial force is proportional to the number of poles as viewed from the side. The number of poles as viewed from the side is the same for TROMAGs that have different number of poles as viewed from the front. Therefore, the axial force remains essentially the same for the three TROMAGs presented above.

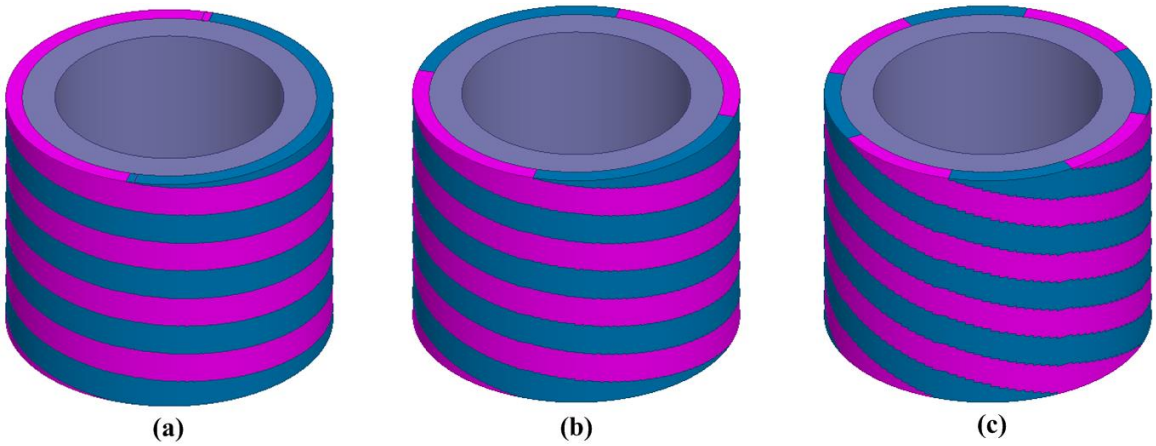

Fig. 20. TROMAGs with different number of poles. (a) 2-pole. (b) 4-pole. (c) 8-pole.

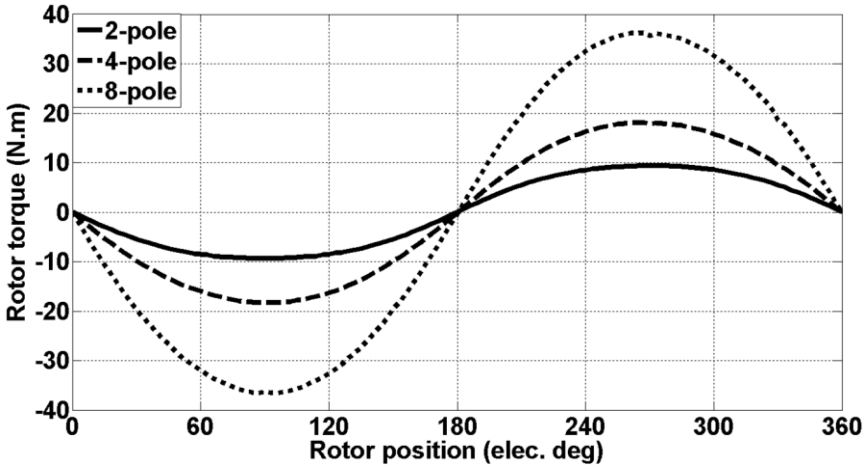

Fig. 21. Rotor torque of TROMAGs with different number of poles.

2.6. Alternative configurations

As mentioned in Section 2.4, the early devices converting linear motion to rotation used reluctance torque for this purpose. Fig. 22 shows a 2-pole reluctance TROMAG, the inner part of which resembles a single-start threaded rod. This reluctance TROMAG has the same dimensions and material as the PM TROMAG of Fig. 8. The

rotor torque and translator force characteristics are depicted in Fig. 23. Due to the reluctance effect, one complete cycle of torque and force is observed as the rotor rotates 180 mechanical degrees (while it is one half of a cycle for the case of a 2-pole PM TROMAG). Also observed is that the pull-out force of 2.9 k N for the 2-pole PM TROMAG of Fig. 18 is reduced to 377 N for the corresponding reluctance TROMAG, showing more than 85% reduction. Increasing the thread depth from 5 mm to 10 mm elevated the reluctance force to 408 N.

It may be also possible to replace either of the rotor or translator magnets with a conductive hollow cylinder, analogous to the slab used in linear induction machines. A model with a 12-pole outer part and the conductive material on the inner part, as shown in Fig. 24, is simulated to show the concept. The inner part is kept stationary and the outer part is rotated at 1500 rpm as an example. Simulation results in Fig. 25 show that through a short interval required for the currents to build up in the conductor, torque and force are developed on the two parts. The pull-out force is roughly 10% that of the PM TROMAG with similar dimensions.

The PM TROMAGs presented so far have a surface mount configuration. However, the iron and magnets may be arranged to form an embedded magnet configuration, as illustrated in Fig. 26, in which blue and pink helices represent alternating axially magnetized PMs. Such a configuration is briefly discussed in [49], and it is claimed that it may offer advantages in terms of fabrication, while offering almost the same force per magnet material as the surface mount configuration.

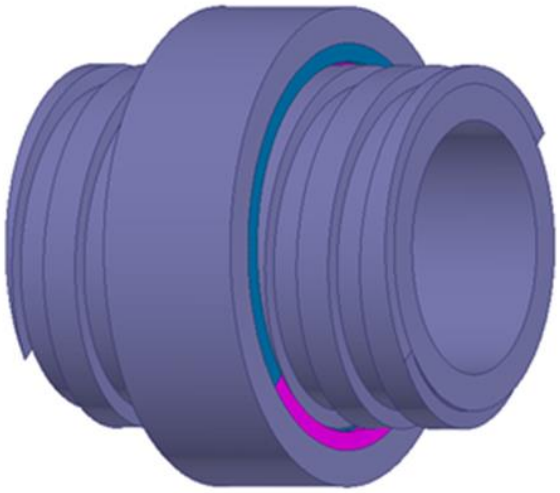

Fig. 22. A 2-pole reluctance TROMAG.

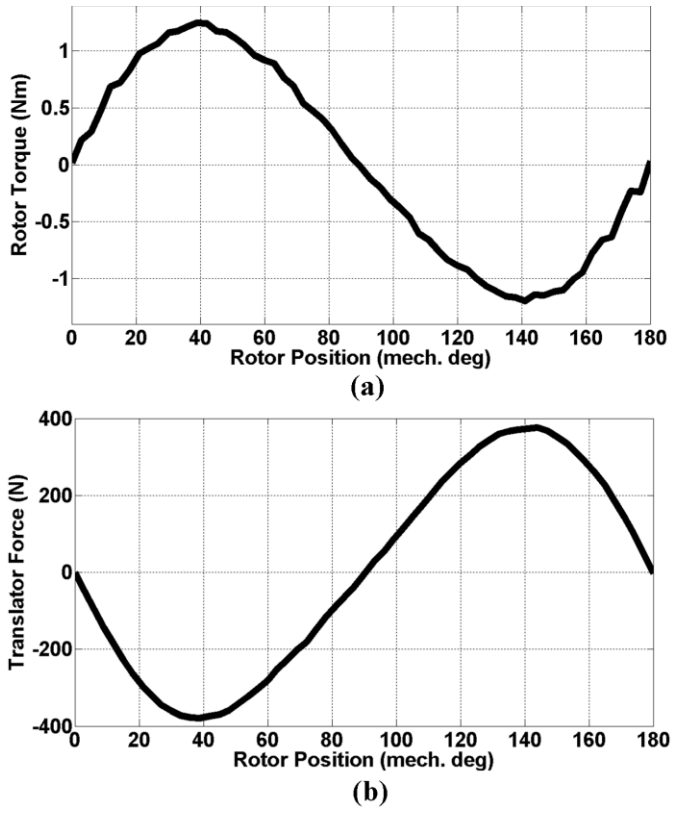

Fig. 23. Characteristics of the 2-pole reluctance TROMAG of Fig. 22. (a) rotor torque. (b) translator force.

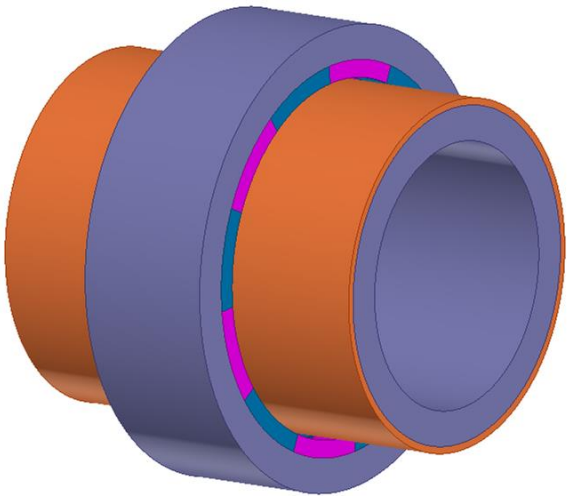

Fig. 24. An induction TROMAG.

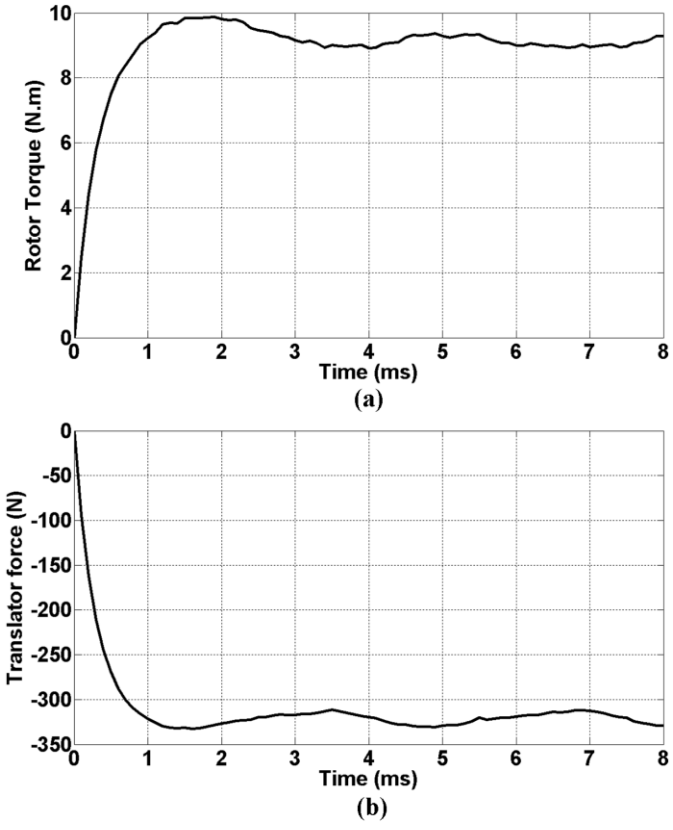

Fig. 25. Rotor torque and translator force of the induction TROMAG of Fig. 24 during the start up. (a) torque. (b) force.

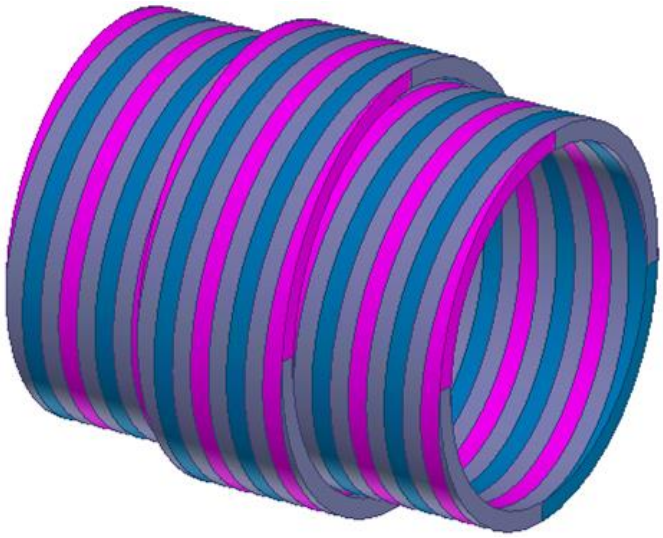

Fig. 26. A 2-pole TROMAG with embedded magnet configuration.

2.7. Summary

This chapter presented the structure of TROMAG and how it converts linear motion to rotation by using helically disposed alternating magnets. It was shown that such a magnetic conversion is a century-old idea that had been resorted to for a few applications; without the use of high energy density magnets, however, the device exhibits a poor force density. Upon using rare earth material magnets, a PM TROMAG offers a force density an order of magnitude larger than those of the conventional linear machines. This makes TROMAG a strong contender for force-dense actuators and linear generators for heaving buoys.

It was shown how TROMAG has been developed in this dissertation by starting from basic arrays of alternating magnets. Skewing the magnets affords the system of two basic arrays the capability of continuously transmitting force in orthogonal directions.

This capability, upon rolling the arrays, translates to the torque and force developed on the rotor and translator of the TROMAG. Moreover, the skew angle translates to the number of poles of the TROMAG as viewed from the front. The number of poles affects the gear ratio and the rotor torque, in that a higher number of poles means a lower gear ratio and higher rotor torque.

In addition, reluctance and induction configurations for the TROMAG were introduced. These alternatives offer a poor force density as compared to a PM TROMAG. A PM TROMAG with embedded magnet configuration was presented as an alternative to the surface mount configuration. Such a configuration, however, requires further investigation.

3. MAGNETIC DESIGN OF THE TROMAG[*]

3.1. Introduction

This chapter is devoted to studying the aspects of the magnetic design of the TROMAG. First, an analytical model of the TROMAG, adopted from [38], is briefly presented. This model, along with 2D and 3D FEA are then used for investigating the influence of design parameters on the performance of the TROMAG. Scaling rules of the TROMAG, the impact of a non-ideal helix on the force and torque characteristics, variations of the shear stress with dimensions of the magnets and air gap, and possibility of demagnetization are discussed. Finally, the system consisting of a TROMAG and a rotary machine is designed and compared (in terms of weight, volume, and cost of the active material), with a PM LTM designed for the same force and speed to show the superiority of the proposed system over the conventional one for high-force, low-speed applications.

---

[*] Part of this section is reprinted with permission from:

"Analysis and design of the Trans-Rotary Magnetic Gear" by S. Pakdelian, N. W. Frank, and H. Toliyat, in *Proc. 2012 IEEE Energy Convers. Congr. Expo. (ECCE)*, pp. 3340-3347, 2012. Copyright 2012 by IEEE.

"An electric machine integrated with the Trans-Rotary Magnetic Gear" by S. Pakdelian, Y. Deshpande, and H. Toliyat, in *Proc. 2012 IEEE Energy Convers. Congr. Expo. (ECCE)*, pp. 3356-3362, 2012. Copyright 2012 by IEEE.

"Design aspects of the Trans-Rotary Magnetic Gear" by S. Pakdelian and H. Toliyat, in *Proc. 2012 IEEE Annu. Conf. Ind. Electron. Soc. (IECON)*, pp. 1720-1725. Copyright 2012 by IEEE.

3.2. Analysis

Using an analytical model instead of 3D FEA would expedite thorough investigation of the relationship between the axial shear stress (briefly called "shear stress" hereafter for simplicity) and dimensions of the magnet and air gap. Moreover, such a model can help automate the design process. The analytical model developed in [38] has been adopted here for this purpose and is presented in the Appendix. The model assumes an ideal helix and starts with 2D approximation of the TROMAG. Fig. 27 presents a 2-pole TROMAG (with right-handed helix) along with its cut-away view and 2D approximation. Notice that, in a TROMAG, the magnets do not need to cover $1/P$ of the helix pitch. The ratio of magnet width, w, to the translator pole pitch, τ_P, is called the magnet coverage, cov. The TROMAG of Fig. 27 has a magnet coverage of 70%. (Note that when the magnets cover $1/P$ of the helix pitch, the magnet coverage is 100%, which is the case for the TROMAG of Fig. 8).

In developing the analytical model, in addition to assuming infinite permeability for the iron core, it is assumed that the device length in Z direction is infinite. The latter assumption results in a symmetric field distribution in Z direction. The first step is to calculate the field due to rotor magnets in the absence of translator magnets. To that end, Laplace and Poisson equations have to be solved in the air gap (the physical air gap and the region appearing after removing rotor magnets) and magnet regions, respectively. Then the translator magnets are replaced with equivalent current-carrying sheets. Finally, the axial component of force exerted on the current-carrying sheets can be

obtained by applying Lorentz's force law and integrating the force over the surface of the current sheet.

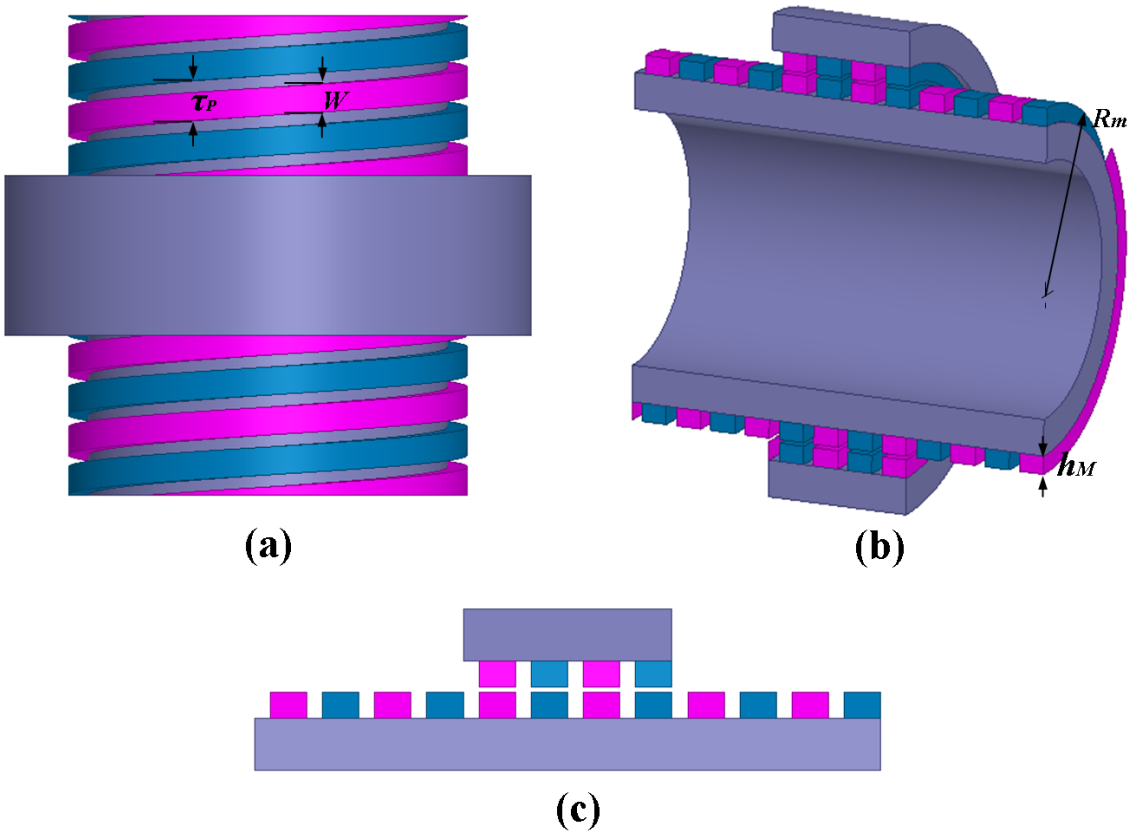

Fig. 27. A 2-pole TROMAG with right-handed helix and 70% magnet coverage. (a) top view. (b) cut-away view. (c) 2D approximation.

Fig. 28 compares the force characteristic of the TROMAG of Fig. 27 obtained from running 3D FEA on the 3D model, shown in Fig. 27(a), from running 2D FEA on the 2D approximation of the same TROMAG, shown in Fig. 27(c), and from the analytical model. The pull-out force calculated from 3D FEA, 2D FEA, and the analytical model is 2462 N, 2504 N, and 2443 N, respectively. Therefore, for force

calculation purposes, by adopting the 2D approximation, a significant saving can be made in computing time at the cost of a small error in the results.

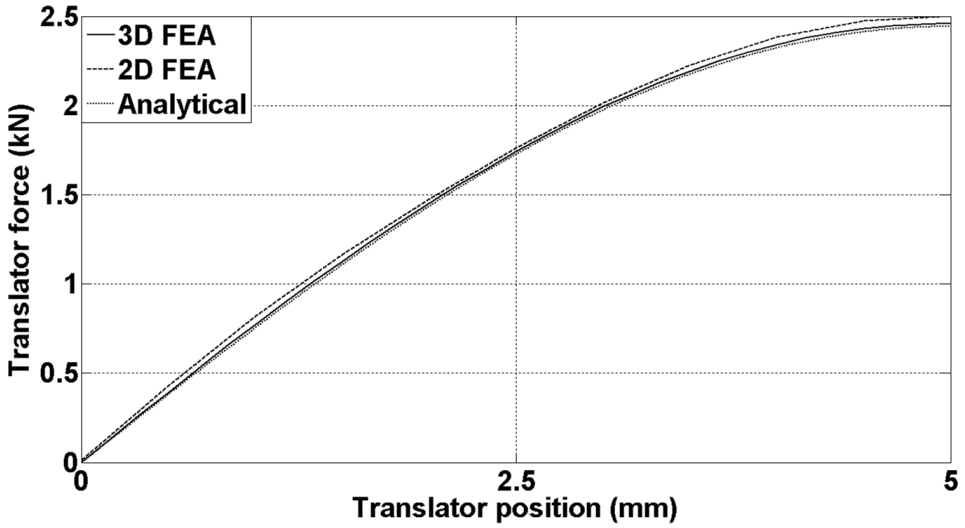

Fig. 28. Force characteristic of the TROMAG of Fig. 27, calculated by three different methods.

3.3. Aspects of magnetic design

3.3.1. Scaling

Intuitively, the pull-out force, F_m, and the pull-out torque, T_m, of a TROMAG are linearly proportional to its active air gap area, A, the area enclosed between the rotor and the translator. A 3D FEA is adopted to verify the linear proportionality of the pull-out force with both the air gap radius and the active length, the two parameters determining the active air gap area. The outer radius, including magnets, of the rotor (inner part) of the TROMAG of Table 1 is increased from 25 mm to 200 mm while the active length is fixed at 40 mm. The same system is simulated for a constant rotor outer radius of 50 mm and a variable active length ranging from 10 mm to 40 mm. The results, presented in

Fig. 29, verify that a TROMAG simply scales in linear proportion with its inner part outer radius, R_m, and its active length, L_{ac}. For the cases studied, the shear stress is about 230 kN/m^2. The force is linearly proportional to L_{ac}, regardless of the length being an integer multiple of the lead.

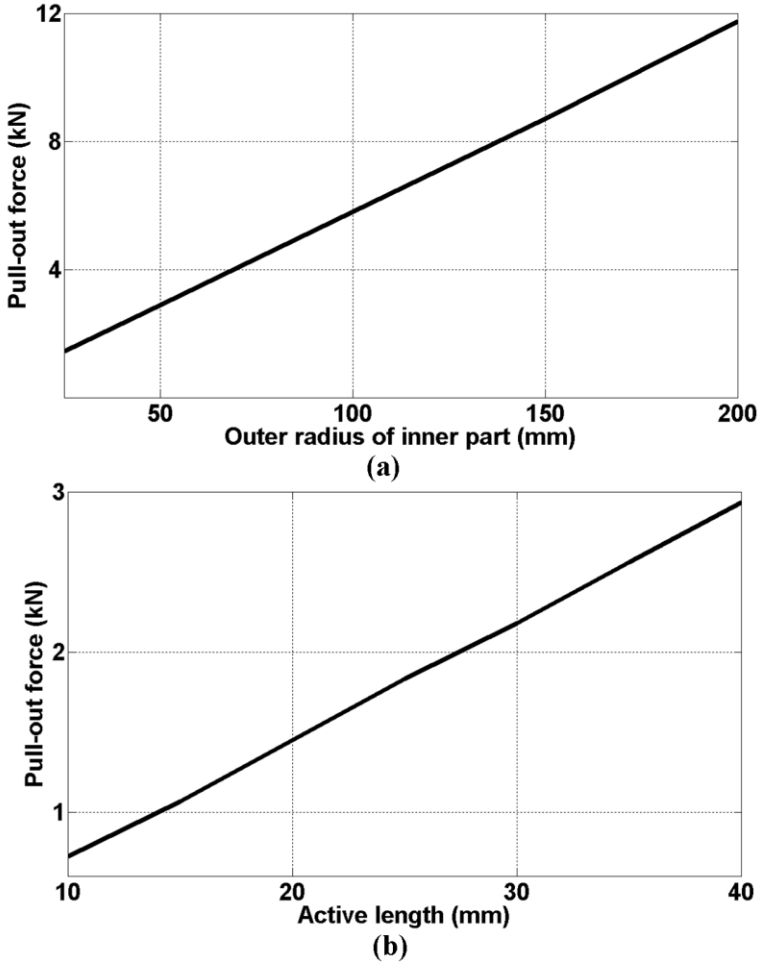

Fig. 29. Variation of the pull-out force with radius and length. (a) radius. (b) active length.

Therefore, the pull-out force of the TROMAG equals:

$$F_m = \sigma A = \sigma 2\pi R_m L_{ac} \tag{4}$$

Let d_c denote the thickness of iron core for both the rotor and translator. The total volume of active iron works out to:

$$V_{Fe,ac} = 2\pi(2R_m + g)L_{ac}d_c \cong 4\pi R_m L_{ac} d_c \tag{5}$$

And the total volume of the active magnets is going to be:

$$V_{PM,ac} = 2\pi(2R_m + g)L_{ac}h_M \cong 4\pi R_m L_{ac} h_M \tag{6}$$

Iron and magnet volumes are indications of the TROMAG active material consumption. The term R_mL_{ac} appears in expressions for force, iron volume, and magnet volume. Therefore, as long as the shear stress is constant, what affects the active material consumption is the product R_mL_{ac}, not the individual values of R_m and L_{ac}. However, the individual values of R_m and L_{ac} would affect the overall force per active volume. The device volume is proportional to second power of radius and first power of length. Hence, the force per active volume remains constant with variation of active length but it linearly drops as the radius increases.

On the other hand, when the stroke of translator, L_S, is accounted for, the total volume of iron and magnet material yields to:

$$V_{Fe,tot} \cong 2\pi R_m(2L_{ac} + L_S)d_c \tag{7}$$

$$V_{PM,tot} \cong 2\pi R_m(2L_{ac} + L_S)h_M \tag{8}$$

At constant shear stress, when the rotor radius is increased, both the pull-out force and total iron and magnet volume increase in linear proportion with the radius. However, when the active length is increased, although the force increases in linear

proportion with the length, the material consumption increases at a lower rate, the amount of which depends on the stroke.

3.3.2. The effects of the helix non-ideality on the force and torque characteristics

Although an ideal TROMAG would employ ideal helical magnets, in practice, the TROMAG may need to be manufactured using blocks of rare earth material magnets that are commercially available. A turn of an ideal helix can then be replaced by a discretized helix which consists of two half-helices, each spanning 180 electrical degrees. The two half-helices are placed such that the second one begins from the end of the first one, without being shifted longitudinally. However, each half-helix is formed by a number of segments, each of which is displaced longitudinally with respect to its neighbors. The amount of displacement equals one half of the helix lead divided by the number of segments minus one. For example, when 20 PM blocks with 9° arc are used to form one turn of a helix with 20 mm lead, then each segment of a half-helix is displaced 10/19 mm with respect to its neighbor.

The more segments which are used, the closer the approximation of an ideal helix will be attained. Nonetheless, employing a lower number of segments would ease the fabrication process. Therefore, it is essential to investigate the effect of helix non-ideality on the device characteristic to enable making a wise decision on the number of segments. To study the effect of non-ideal helices, several segment arcs in the range of 9° to 60° are studied. Fig. 30 shows the resultant arrangement of the magnets in four cases. In all cases, the arc of the segments for both the rotor and translator is assumed to be the same.

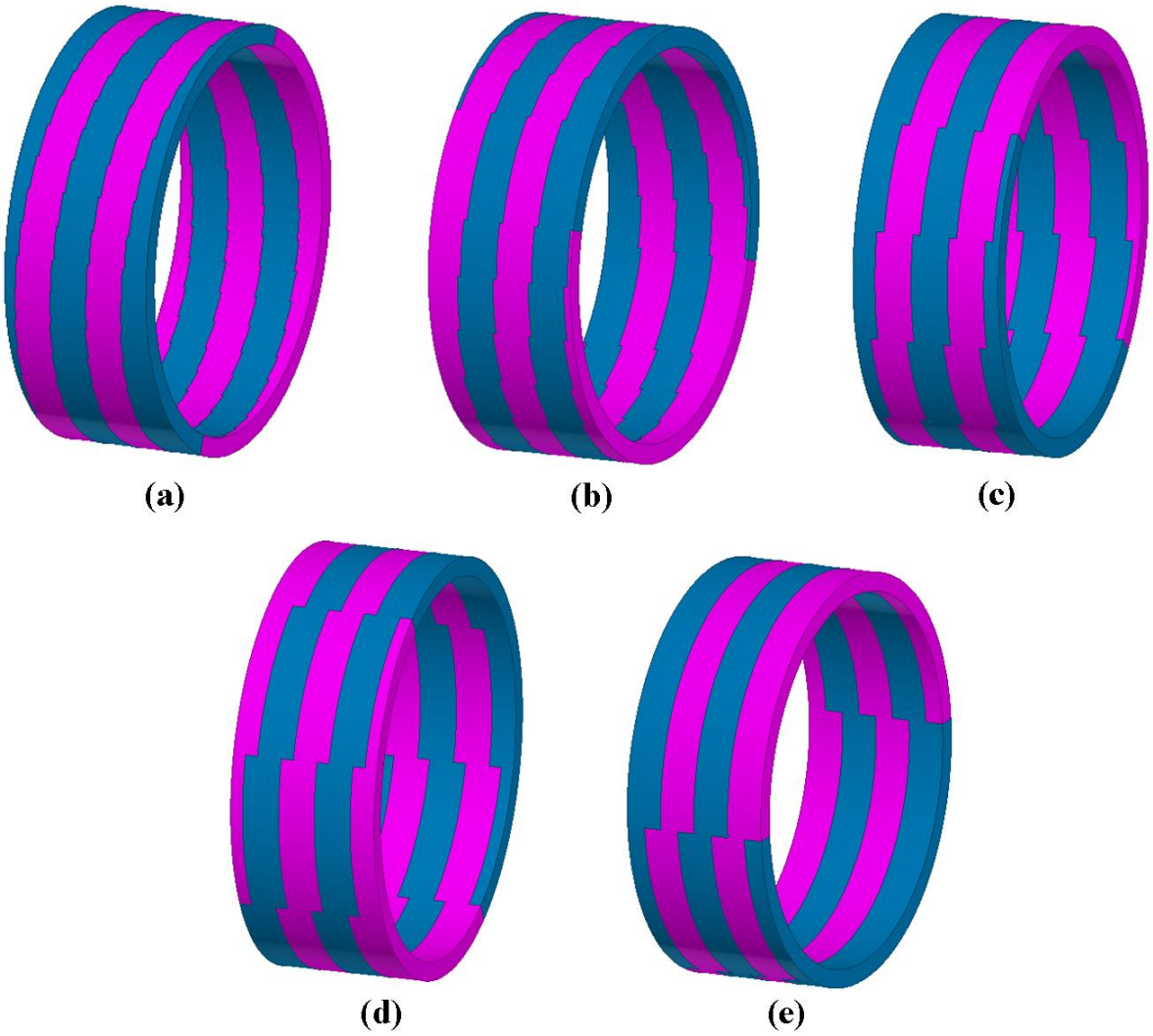

Fig. 30. TROMAGs with different segment arcs. (a) 9 degrees. (b) 15 degrees. (c) 30 degrees. (d) 45 degrees. (e) 60 degrees.

The torque and force profiles, obtained by 3D FEA, are given in Fig. 31. It is observed that the number of steps in each waveform corresponds to the segment arc chosen. For example, a total of eight steps are observed in the profiles corresponding to 45° segment arc. Scrutiny of Fig. 31 suggests that as a discretized helix further moves away from an ideal helical shape, two consequences follow: reduction of the pull-out

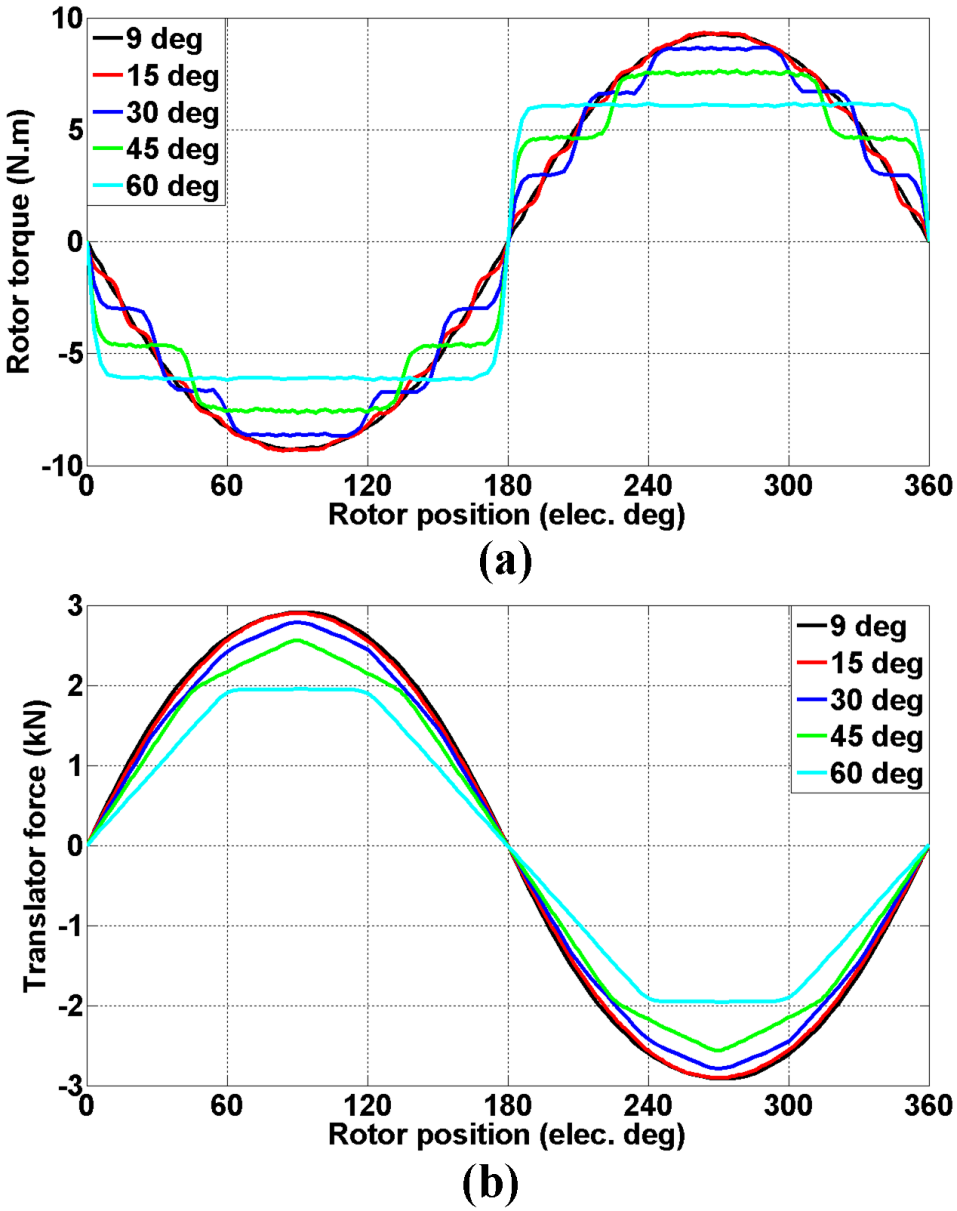

Fig. 31. Characteristics of TROMAGs with different amounts of segment arc. (a) rotor torque. (b) translator force.

force, and change in waveforms of the force and torque profiles. As a lower number of wider segments is used to shape the helix, the force profile tends to become trapezoidal, whereas the torque profile approaches a rectangular waveform. Non-ideal torque and

force profiles imply that the gear ratio is no longer a constant, as opposed to the case of an ideal helix TROMAG in which the gear ratio, according to (1), is merely determined by the lead. As observed in Fig. 31, the ratio of the translator force to the rotor torque largely varies with the relative position of the rotor and translator. Therefore, the actual gear ratio would be dependent on the load.

Another point to make about Fig. 31 is that the torque and force characteristics do not exhibit a noticeable change as the segment arc drops below 15°. This observation suggests that 15° may be considered a reasonable choice for the segment arc. For the rest of this study, it is assumed that the helices closely follow an ideal form.

3.3.3. The effects of design parameters on the shear stress

3.3.3.1. The pole pitch, magnet thickness, and air gap length

The analytical model mentioned in Section 3.2 is adopted to study the influence of pole pitch, magnet thickness, and air gap length on the shear stress. Fig. 32(a) shows variation of maximum shear stress with pole pitch for several values of magnet thickness. In this section, magnets are assumed to be full pitch, that is, the magnet coverage is 100%. The magnet material is given in Table 1. The air gap length is fixed at 1 mm while the magnet thickness is increased from 1 mm to 10 mm with steps of 1 mm. Two main conclusions can be drawn from this diagram. First, for any given air gap length and magnet thickness there is an optimum pole pitch for which the shear stress is maximized. For example, for the case of 1 mm air gap and 5 mm thick magnets, the optimum pitch would be 10 mm, and the resultant shear stress would be about 230 kN/m^2. As a second conclusion, for a given air gap length and pole pitch, increasing the

magnet thickness increases the shear stress. However, the effect will saturate beyond some point. As seen, by moving up on the diagram, the distance between consecutive curves decreases, although the increments of magnet thickness are constant. This result was not unexpected, as increasing the magnet thickness increases the reluctance of the flux path as well.

Due to manufacturing tolerances, the air gap length has to be increased as the TROMAG is designed for larger sizes. The effect of increasing the air gap length on the shear stress is shown in Fig. 32(b). To obtain this diagram, the pole pitch is kept constant at 10 mm, the air gap length is increased from 1 mm to 5 mm, and the shear stress is calculated for values of magnet thickness in the range of 1 mm to 10 mm. It is observed that increasing the air gap length at a constant magnet thickness reduces the shear stress. The curves presented in Fig. 32(b) may also be looked upon as another form of demonstrating the second conclusion made from Fig. 32(a): for a given air gap length, increasing the magnet thickness increases the shear stress up to some point and then the effect becomes insignificant. Therefore, increasing the magnet thickness may not be an effective solution to overcome the reduction of shear stress due to an increased air gap length.

To maintain the shear stress constant as the air gap length increases, both magnet thickness and pole pitch have to be increased proportionally. However, increasing the magnet thickness adversely affects the cost. Moreover, increasing the pole pitch may have two potentially adverse consequences. Larger pole pitch means, according to (1), a

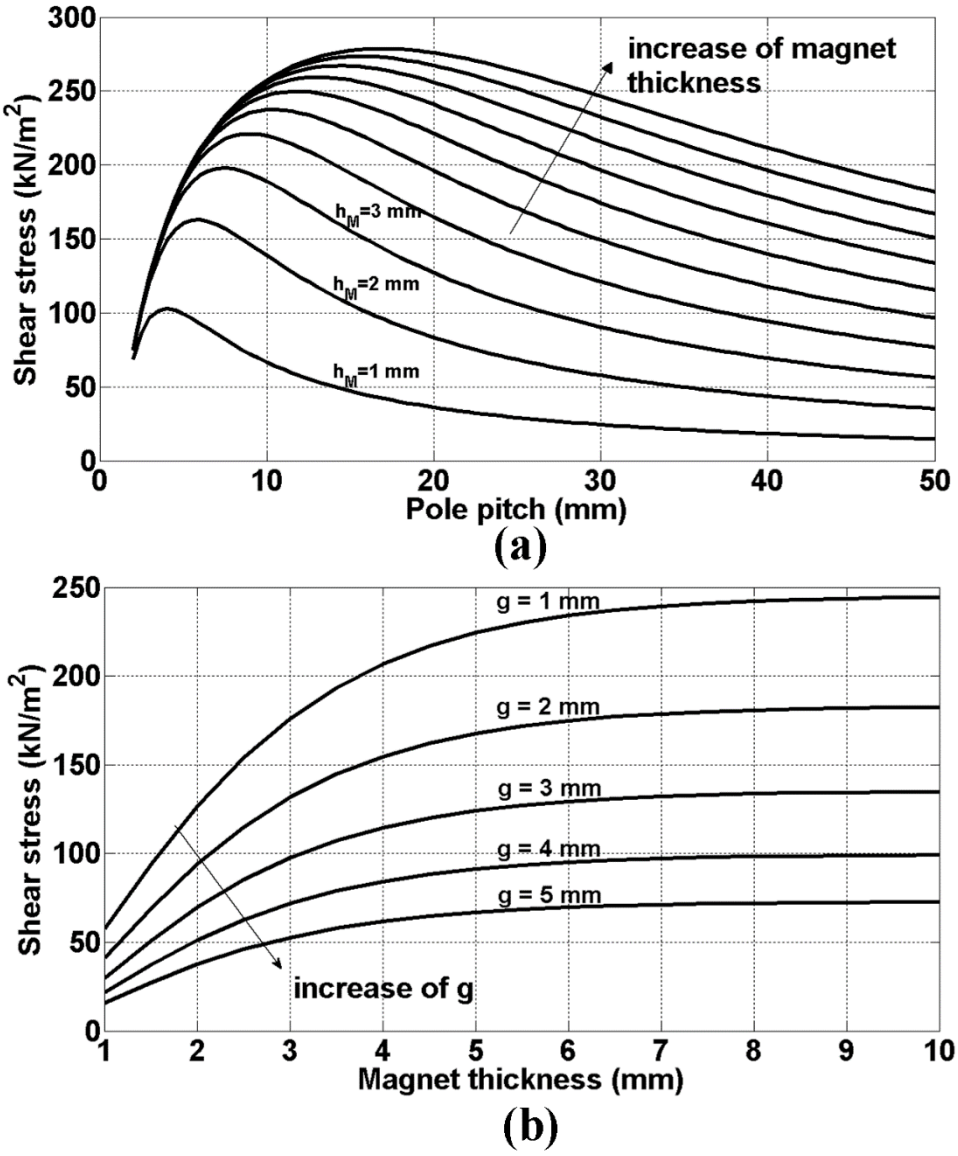

Fig. 32. Variations of the shear stress. (a) shear stress vs. magnet pole pitch for several values of magnet thickness. (b) shear stress vs. magnet thickness for several values of air gap length.

lower gear ratio. When dynamical effects associated with the load are neglected, it can be stated that a lower gear ratio results in a higher rotor torque and therefore, a higher demand on the machine side when the TROMAG is used in combination with a rotary

machine. In addition, an increased magnet width requires thicker core to carry the resultant flux.

3.3.3.2. The magnet coverage

The effect of the magnet coverage on the shear stress is examined by using the analytical model and is illustrated in Fig. 33. The air gap length is fixed at 1 mm and the magnet coverage has been increased from 10% to 100% of the pole pitch, set at 10 mm, for different values of magnet thickness, from 1 mm to 10 mm. As seen, for each magnet thickness there is a range of magnet coverage over which the shear stress increases almost in linear proportion with the magnet coverage. The extent of that range depends on the magnet thickness. Moreover, the rate of rise of shear stress due to the increase of the magnet coverage tends to saturate as the coverage approaches unity because the leakage flux between adjacent magnets increases. For example, when the magnet thickness is 5 mm, reducing the coverage from 1 to 0.75 (saving 25% on magnet material), results in only an 11% reduction in shear stress, from 230 kN/m2 to 205 kN/m2. However, when the coverage is further reduced to 50%, the drop of shear stress (compared to the case of unity coverage), is almost 50%. Therefore, it is concluded that for any given pole pitch (corresponding to a given gear ratio) and air gap length, a certain combination of magnet thickness and magnet coverage can maximize the resultant shear stress with respect to the amount of PM material consumed. Fig. 34 shows variations of the force per active magnet volume versus magnet thickness and magnet coverage for the case of 10 mm pole pitch and 1 mm air gap length. The highest force per active magnet volume achieved in this case is about 40 MN/m^3, and occurs

when the magnet thickness and coverage are almost 1.6 mm and 66%, respectively. In this case, the resultant shear stress is 85.4 kN/m^2.

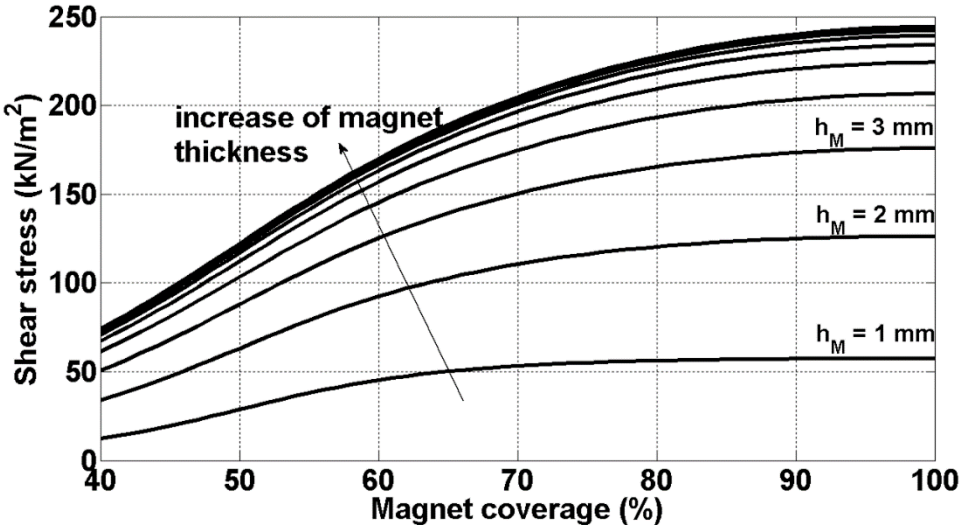

Fig. 33. Shear stress vs. magnet coverage for several values of magnet thickness.

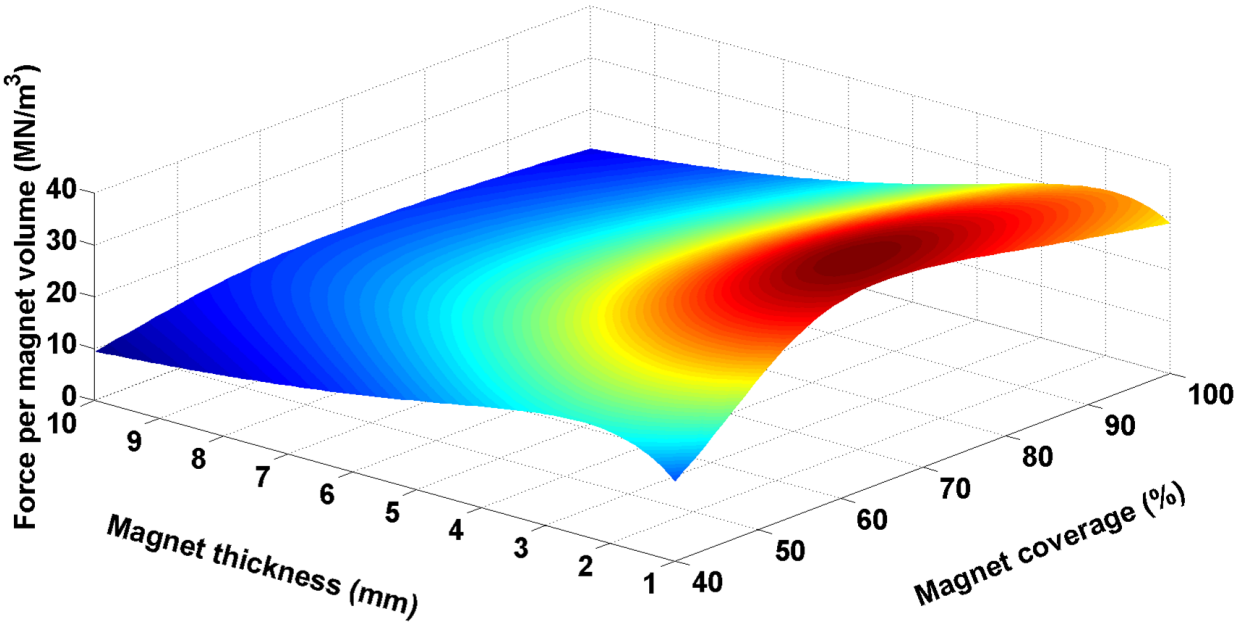

Fig. 34. Variation of force per volume of PM material vs. magnet thickness and magnet coverage for 10 mm pitch and 1 mm air gap length.

3.3.4. Demagnetization

Due to their high coercivity, high energy density PM materials are known to withstand large demagnetizing fields. However, confrontation of two sets of rare-earth PM poles in a TROMAG may result in demagnetization when the issue is not properly addressed in the design.

Irreversible demagnetization occurs when the operating point of a PM drops below the knee-point of its B-H characteristic. For the rare-earth PM material, at room temperature, the flux density corresponding to the knee-point, $B_{D,}$ generally falls in the third quadrant (it is negative). B_D, however, climbs up toward the second quadrant as the temperature increases. Other than temperature, the value of B_D depends on the type of magnet (Nd-Fe-B or Sm-Co) and the material grade; however, for conventional Nd-Fe-B magnets, zero to 0.1 T may be an approximate range for B_D at 40 $^{\circ}$C.

Intuitively speaking, confrontation of two sets of magnets with unequal thickness can result in demagnetization of the thin magnets. Consider a TROMAG with 20 mm pole pitch and unity magnet coverage, with the thicknesses of rotor PMs, h_r, and translator PMs, h_t, being set at 5 mm and 4 mm, respectively. Fig. 35 shows the 2D model of this TROMAG and the corresponding flux lines at three different relative positions of the rotor and translator. Periodic boundary conditions are imposed to exclude the end effects originating from the open-ended structure of the device. At both aligned and unaligned positions, the force and torque are zero, while at the half-way position, the TROMAG operates at its pull-out values of force and torque.

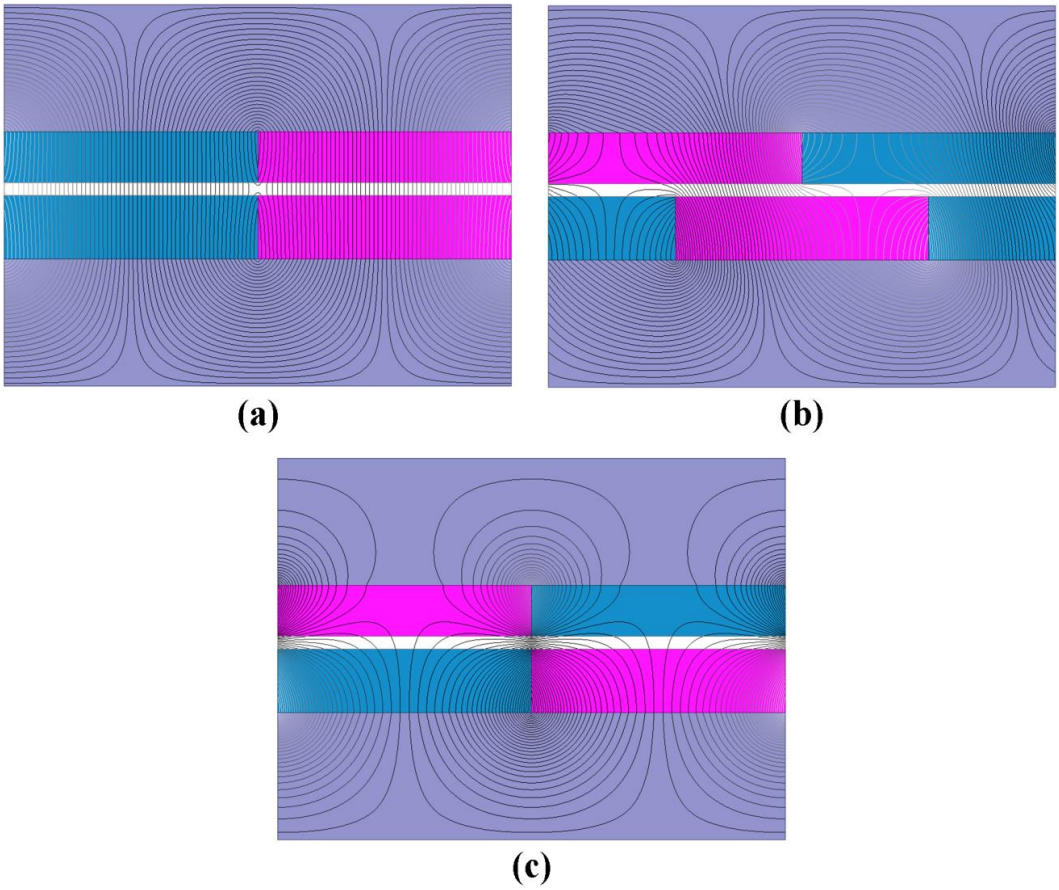

Fig. 35. Flux lines in a TROMAG with unequal magnet thickness on rotor and translator. (a) aligned. (b) half-way. (c) unaligned position.

Normal (radial) component of the flux density, B_r, on the lines spanning two pole pitches over the surface and middle of the thinner magnets are obtained from 2D FEA and are shown in Fig. 36 for the three positions above. As expected, the unaligned position is the worst case for demagnetization, because in that position the opposite poles of the rotor and translator fully confront. Therefore, only the unaligned position is considered in the rest of this study. It is observed in Fig. 36 that when the TROMAG is in an unaligned position, B_r, clearly becomes negative at the surface of the thinner

magnets, and close to zero (but still negative) at their middle; thereby, demagnetization may occur. When the thicknesses of the magnets of both arrays are set at 5 mm, B_r is about 0.02 T at the surface. This means that even with equally thick magnets, demagnetization can be possible, depending on the magnet grade and temperature.

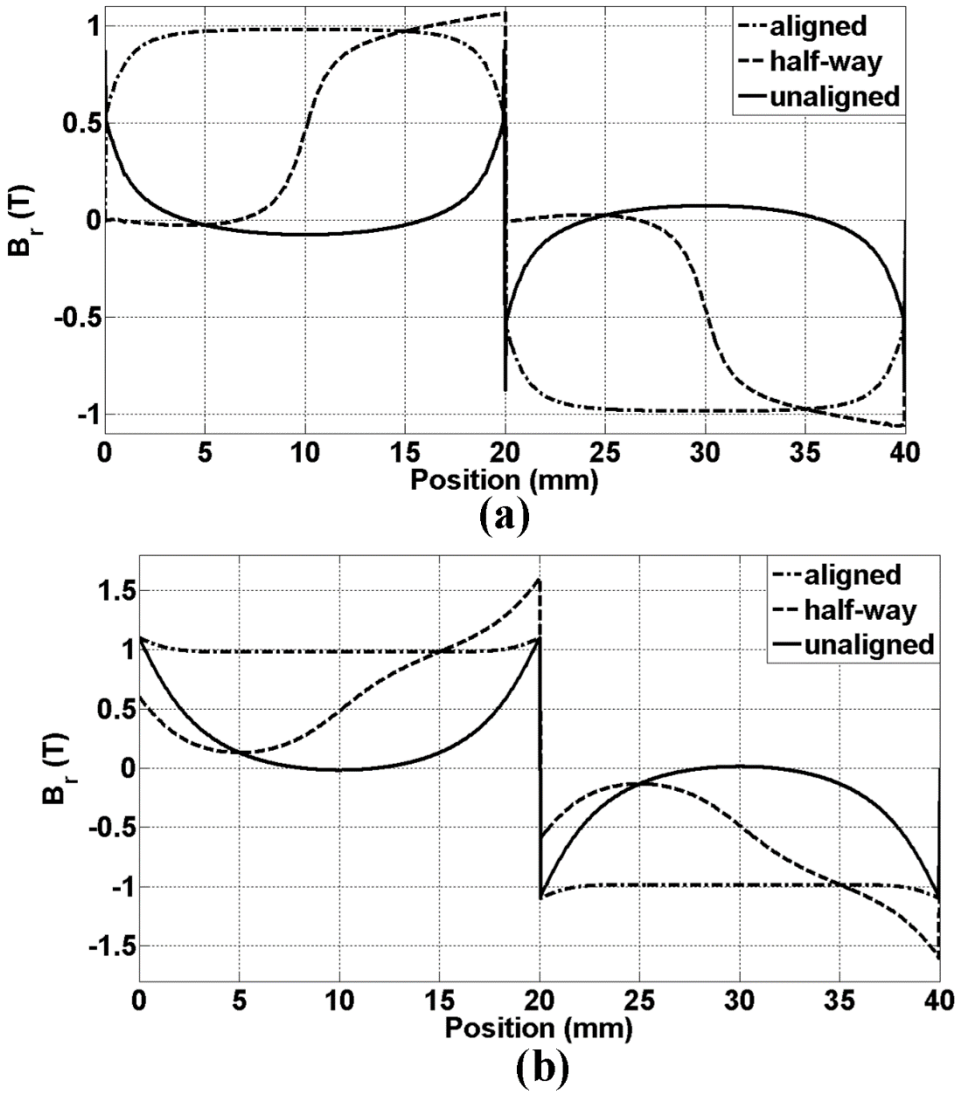

Fig. 36. Normal component of flux density in the thinner magnets at aligned, half-way, and unaligned positions. (a) surface. (b) middle.

To investigate the effect of magnet coverage on the extent of demagnetization, the system of Fig. 35(c) is simulated for different values of magnet coverage. The maximum demagnetizing flux density at the surface of the rotor magnets, B_r, shown in Fig. 37, implies that a lower magnet coverage results in a smaller demagnetizing field. Unity magnet coverage, thus, is the worst design regarding demagnetization.

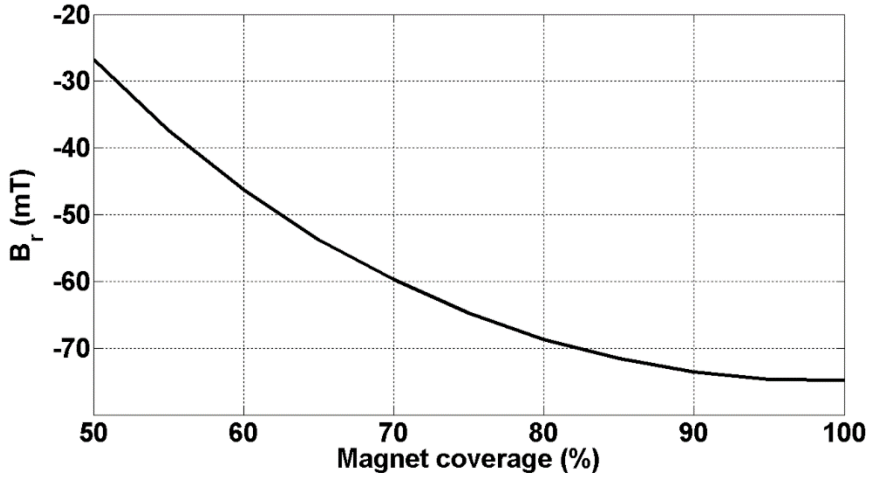

Fig. 37. Variation of normal component of flux density at the magnets surface vs. magnet coverage.

To study the influence of pole pitch and magnet thickness on demagnetization, the air gap length, g, is kept constant at 1 mm and the pole pitch is varied over the range of 5 mm to 30 mm, assuming unity magnet coverage. In one case, the corresponding results of which are presented in Fig. 38(a), the magnets of the rotor and translator have the same thickness ($h_r=h_t=h$). In another case, whose corresponding results are depicted in Fig. 38(b), the thickness of the translator magnets is fixed at 5 mm while the thickness

of the rotor magnets holds several smaller values ($h_r \neq h_t$). In both cases B_r is obtained versus the pole pitch.

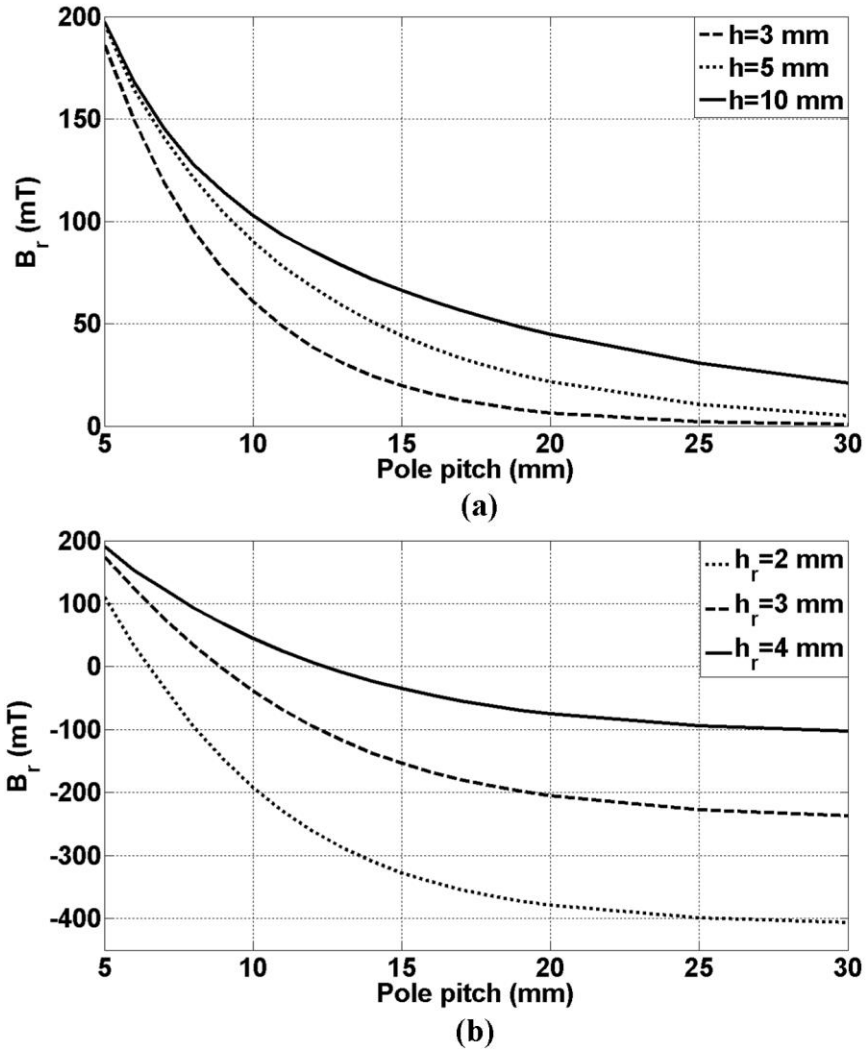

Fig. 38. Variations of normal component of flux density at the magnets surface vs magnet dimensions. (a) magnets with equal thickness on rotor and translator. (b) 5 mm thick magnets on rotor and thinner magnets on translator.

Scrutiny of the results reveals that demagnetization is a function of magnet dimensions ratio, as well as the air gap length. It is observed that thinner and wider

magnets are more prone to demagnetization. In other words, at a given magnet thickness to air gap length ratio, h/g, increasing the ratio of the pole pitch to magnet thickness, τ_P/h, results in increase of the demagnetizing field.

In order to prevent demagnetization of PMs, therefore, it is advisable to employ magnets of similar material grade and thickness for both rotor and translator to ensure that all over the magnets, the flux density remains in the second quadrant at any relative position of the rotor and translator. Moreover, the knee-point of the PM B-H characteristic at practical operating temperatures must be checked against the value of demagnetizing flux density.

3.3.5. Core thickness

The 2D model of the TROMAG can be used to calculate approximately the required core thickness, d_c, to achieve a desired flux density in the core, B_c. The magnetic equivalent circuit of the model presented in Fig. 35(a) is shown in Fig. 39, in which the iron is assumed to be infinitely permeable, both inner and outer parts are assumed to be infinitely long, and the magnets on both parts have the same thickness.

Values of the circuit elements are given in (9). F_{PM} is the magnet mmf, R_{PM} is the magnet reluctance, and R_g is the air gap reluctance.

$$F_{PM} = \frac{B_r h_M}{\mu_0 \mu_r} \tag{9-a}$$

$$R_{PM} = \frac{h_M}{\mu_0 \mu_r A_{PM}} \tag{9-b}$$

$$R_g = \frac{g}{\mu_0 A_g} \tag{9-c}$$

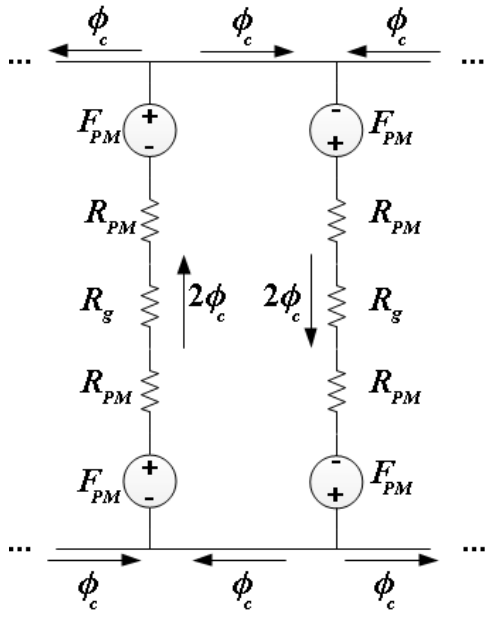

Fig. 39. Magnetic equivalent circuit of the 2D model of the TROMAG in aligned position.

A_g and A_{PM} are the areas of air gap and magnet used for calculating the flux path reluctance. The cross-sectional area of the cores, A_c, is also roughly approximated by assuming $R_m >> h_M$ and $R_m >> d_c$.

$$A_g \cong 2\pi R_m \tau_P \tag{10-a}$$

$$A_{PM} \cong 2\pi R_m w \tag{10-b}$$

$$A_c \cong 2\pi R_m d_c \tag{10-c}$$

From the magnetic equivalent circuit, the average flux passing through the core, φ_c, is given by:

$$\varphi_c = \frac{F_{PM}}{2R_{PM} + R_g} \tag{11}$$

By substituting (9) and (10) in (11), and knowing that $\varphi_c = B_c A_c$, the average core flux density for a given core thickness is obtained from (12).

$$B_c = \frac{B_r h_M}{d_c \left(\frac{2h_M}{w} + \frac{\mu_r g}{\tau_P} \right)} \tag{12}$$

Fig. 40 (b) shows the normal component of flux density in the core of the outer part of the TROMAG of Fig. 40(a), on a vertical line drawn at the middle of the core (on the centerline between the two magnets) from the bottom to the top. The FEA is performed in a Cartesian coordinate system. The TROMAG quantities are the same as those given in Table 1, except for the magnet coverage which is 70% here, and the core thickness which is set at 5 mm. From (12), B_c works out to 0.717 T, whereas 2D FEA calculates B_c to be 0.721 T. A very close agreement is observed between the results obtained from the simple 2D magnetic equivalent circuit model and the 2D FEA.

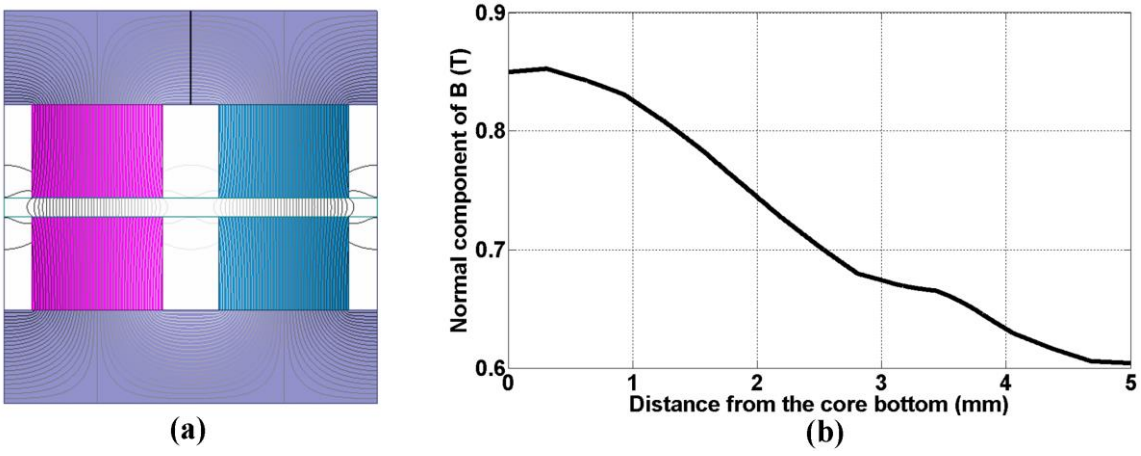

Fig. 40. Flux in the core of a TROMAG in aligned position. (a) flux lines. (b) normal flux density on a vertical line in the core.

3.4. Integration of the TROMAG with a rotary electric machine

This section aims to show that for a high-force, low-speed load characteristic, an electric machine integrated with a TROMAG, which is called MITROMAG hereafter for the ease of reference, can significantly save on the weight and cost of the required magnetically involved material (ferromagnetic iron, copper, and magnet) compared to a conventional direct drive linear PM machine that is designed for the same force and speed. The material that is required for building the structure is not accounted for in this study. In order to compare the two technologies, the approach taken here is to optimally design a MITROMAG for a constant force and speed, and compare it (in terms of weight, volume, and cost of the material), with a linear machine that is optimally designed for the same specifications. The optimization problem framed for each topology has identical set of objectives, constraints, and materials employed, thus making a fair comparison between the two. Multi-objective optimization to achieve lighter and less costly designs, which are referred to as "Pareto-optimal" designs, is performed by using GOSET 2.4, a population-based genetic algorithm (GA) toolbox [50]. First, the design constraints, design constants, design variables, and the design procedure for a MITROMAG are explained. Next, the same is presented for the benchmark linear machine. Then, the results of design optimization are demonstrated and discussed.

3.4.1. Optimal design of the MITROMAG

MITROMAG consists of a TROMAG and a rotary machine that is coupled to the shaft of the rotor of the TROMAG. The MITROMAG design starts with designing a

TROMAG for the given force and speed, as the design constraints. The choice of gear ratio for the TROMAG determines the torque and rotational speed for which the rotary machine has to be designed. According to (1), choosing a narrower thread (shorter pole pitch), τ_P, results in a larger gear ratio and therefore, a lower torque and a higher speed for the rotary machine, which means a higher power density design can be achieved for the rotary machine. However, a large rotational speed may cause rotor vibrations when the TROMAG is not perfectly concentric [51]. Moreover, considering the low stiffness of the TROMAG, a large rotational speed may also cause difficulties in controlling the system.

In addition, as evident from Fig. 32, a narrow thread can result in a poor force density for the TROMAG. In particular, as the air gap is increased for larger systems, there is a need for a longer pole pitch to maintain optimum shear stress. Note that a longer pole pitch results in a lower gear ratio and a larger torque demand on the rotary machine side of the MITROMAG.

Given the discussions above, it is clear that in general, optimal design of the MITROMAG entails simultaneous design of both the TROMAG and the rotary machine part. Another issue that mandates the simultaneous design of both parts is the dynamic performance, which is application-specific. Depending on the load dynamics, the TROMAG effective gear ratio "seen" by the rotary machine can be different from the rated gear ratio given by (1). For example, it is shown in Chapter 4 that in an application such as wave energy, the rotor moment of inertia would significantly affect the effective gear ratio. Such factors must be considered when designing for a specific application.

In this study, however, designs are performed for a constant speed of 1 m/s, and several values of constant force. It has also been decided to set the rotor speed at 3000 rpm. This way, the gear ratio of the TROMAG is fixed at 100π for all cases, and designs of the TROMAG and the rotary machine become mutually exclusive. Therefore, the TROMAG and rotary machine are designed separately, thus reducing the complexity of the optimization problem.

An electric machine may be designed such that it can temporarily deliver more than its rated power upon injecting higher current. On the other hand, a TROMAG force cannot exceed the pull-out value which is determined by its magnetic design and is not controllable. To enable a fair comparison, for each case the TROMAG is designed for a pull-out force that is 25% larger than the rated force for which the linear machine is designed. This assures that the TROMAG can operate at forces up to 25% higher than its rated value without slipping.

The best choice for a rotary machine configuration, overall, depends on the application and optimization objectives. In this dissertation, a V-shaped interior permanent magnet machine (IPM) is selected for the rotary machine part of the MITROMAG. This choice achieves good torque density and efficiency at the rated operating point. Note, however, that depending on the specific application for which the MITROMAG is designed, surface-mount configuration or buried PM rotor configurations other than V-shaped, such as trough-shaped or PM-assisted synchronous reluctance, may be superior to the V-shaped IPM.

In the following, design constraints, variables, and constants are given as well as a general design procedure for a MITROMAG.

3.4.1.1. Design constraints, constants, and variables of the MITROMAG

Design of a MITROMAG is performed for a given rated force and speed as the constraints. The speed is set at 1 m/s for all designs. Several levels of pull-out force are considered, from 1.25 kN to 125 kN (each 25% above the rated force of the corresponding PM LTM), which are corresponding to 1 kW to 100 kW power. Moreover, the winding maximum temperature is restricted to 180 $^{\circ}$C.

As explained earlier, the TROMAG gear ratio is fixed at 100π. Therefore, in each case a 2-pole TROMAG with 10 mm pole pitch has to be optimally designed for the given force. Design variables for the TROMAG are then the magnet thickness, magnet coverage, and the rotor radius.

A 2D view of one pole of a V-shaped IPM, along with its geometrical design variables, is shown in Fig. 41. For the IPM, the selected design variables are the slot-pole combination, (N_S, N_P); magnet thickness, h_M; magnet angle, α_V; rotor inner radius, R_{ri}; rotor outer radius, R_{ro}; split ratio (ratio of stator outer radius to the rotor outer radius), SR; stator core thickness, d_{cs}; tooth width, W_t; slot opening, b_0; slot tip height, H_{s0}; slot wedge height, H_{s1}; and the conductor current density, J. Rotor length is assumed to equal the stator stack length. Bridge width t_b is set at a constant value for all the designs of a power level. In addition, to avoid high switching frequencies, the maximum supply frequency is limited to 300 Hz. With 3000 rpm as the top speed, the

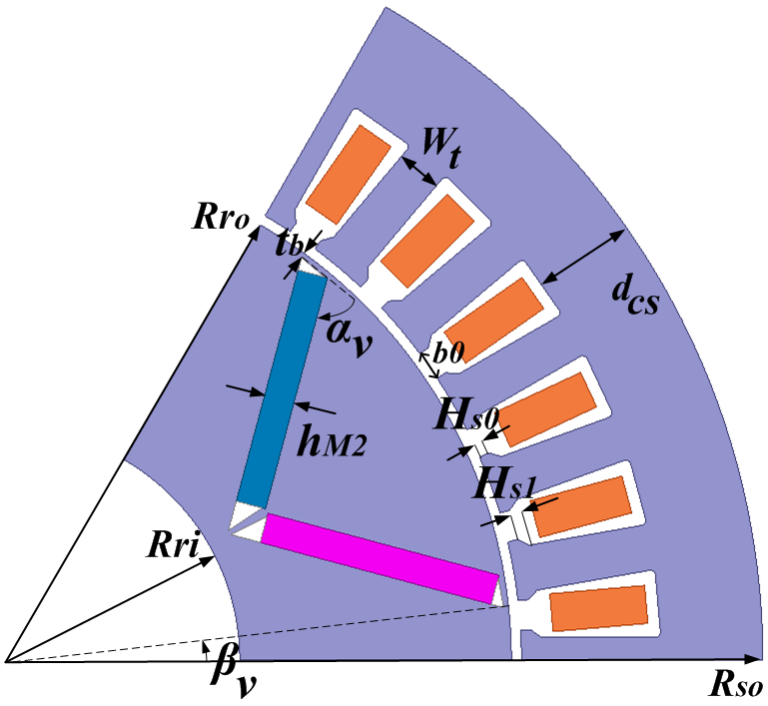

Fig. 41. One pole of a V-shaped rotary IPM and its geometrical design variables.

maximum number of the IPM poles will be restricted to 12. The values considered for the "slot per pole per phase" are 1, 1.5, 2, and 3, respectively.

In all designs, the air gap length for both the IPM and TROMAG is set at 1 mm. Moreover, M19 laminations with 0.5 mm thickness and a stack factor of 95% are used for the IPM. Ferromagnetic iron such as 1020 steel can be employed for the TROMAG. NdFeB magnets with B_r = 1.1 T and μ_r = 1.05 are considered for both the rotary machine and the TROMAG. The ambient temperature, T_{amb}, is set at 40 $^{\circ}$C.

It is decided to account for the efficiency by adding the cost of electricity over a 5-year time period [29]. This cost represents the energy lost to losses if the system was used as a motor, or the energy that would not be harvested if the system was used as a

generator. Electricity price is set at a constant value of 5 cents per kWh. The cost of iron, copper, and magnet is assumed to be 3, 8, and 90 $/kg, respectively.

3.4.1.2. Design procedure of the MITROMAG

A. Design of the TROMAG

Aspects of the magnetic design of the TROMAG were presented in Section 3.3. Restrictions on outer radius and total length are imposed by the space restrictions of a certain application. Even without any space restrictions, very long rotors with a small radius should be avoided as they are more prone to rotor deflection and consequent unbalanced radial forces [39]. In the studied TROMAG, it is assumed that the outer part is the translator and it is longer than the rotor by the amount of stroke. The rotor length-to-radius ratio is also set at 12. In each design case, magnet thickness and coverage are varied and the total weight and cost of the material are obtained. The analytical model discussed in Section 3.2 is used for calculating the TROMAG axial force.

It was shown in Chapter 2 that in an ideal TROMAG, as long as the rotor and translator are moving in synchronism, which is the case in steady state operation, the relative position of rotor magnets and translator magnets remains constant. Therefore, the losses in magnets and iron cores are expected to be insignificant. The main losses of a TROMAG are then attributed to the bearings. The 17 kN lab prototype presented in [39] has exhibited an efficiency of over 90% at most operating points. Higher efficiencies are expected as the technology matures. In this study, efficiency of the TROMAG is assumed to be independent from the magnetic design, and is set at 95%, 92%, 90%, and 80% for force levels of 100 kN, 50 kN, 10 kN, and 1 kN, respectively.

B. Design of the IPM

In each case, the IPM rated torque is obtained from (1) by knowing the gear ratio (fixed at 100π) and the rated force for which the MITROMAG is designed. Notice that a 25% margin is not considered for the rotary machine because, similar to the LTM, it can be designed to be capable of delivering higher power for short periods of time. The IPM speed is also set at 3000 rpm for all designs. The GA is used to achieve an optimum design for the IPM. Each "individual" generated by the GA is evaluated by employing two-dimensional (2D) thermal and magnetic FEA.

The first step in analyzing each GA-generated individual is to create the slot geometry and populate the slots with wires accounting for the wire enamel, varnish, and slot lining [52]. The inter-strand distance is calculated based on practical data from manufactured machines. The conductor fill factor can then be obtained by dividing the area occupied by copper to the whole slot area. In addition, once the slot is populated, the heat generated in the slot (slot copper losses) is calculated for an arbitrary current density. Assuming a unity stack length, a thermal FEA is then performed to obtain the resultant temperature distribution in the slot. Upon dividing the highest temperature in the slot, T_{spot}, by the slot copper loss, the thermal resistivity from the hot spot to the core $\rho_{th,spot}$, is obtained in $^{\circ}$C.m/W. Average temperature of the slot is also calculated and divided by the slot heat to obtain the average thermal resistance from the winding to the core, $\rho_{th,avg}$. While the latter parameter is later used for calculating the average temperature of the slot to find the average copper resistivity, the former parameter is

used for calculating the winding hot spot to ensure the insulation thermal limit is respected.

The next step is to create the IPM geometry for performing a magnetic FEA. In order to save on computation time, anti-periodic boundary conditions are imposed, so analyzing a fraction pole of the machine suffices. By knowing the current density, as an attribute of each individual, and conductor fill from the previous step, the phase current can be calculated. Since the selected machine configuration has saliency, the maximum torque position depends on the d-axis and q-axis inductances, L_d and L_q. Therefore, a magnetic FEA is run to obtain L_d and L_q at the given phase current. Moreover, the phase current is injected in the negative d-axis direction and the flux density distribution in the PM is obtained to ensure demagnetization will not occur. To obtain the average torque, accounting for the torque ripple, the rotor is rotated by 180 electrical degrees over six equal steps. At each step, a static 2D magnetic FEA is performed and the torque per unit of stack length is calculated. Iron losses, P_{Fe}, including hysteresis, classic eddy, and excess eddy losses, are also calculated at each step by using the conventional iron loss model.

The required stack length, L_{stack}, to yield the desired torque can then be calculated. The total copper loss, P_{cu}, is calculated accounting for the end winding length. Afterward, the winding hot spot temperature is checked against the maximum temperature constraint. To calculate T_{spot}, first the core temperature, T_{core} is obtained from (13).

$$T_{core} = T_{amb} + R_{th,core} \times (P_{Cu} + P_{Fe}) \tag{13}$$

In (13), $R_{th,core}$ is the thermal resistance between the stator housing and the ambient, and is given in (14).

$$R_{th,core} = 1/(hA) \tag{14}$$

In (14), A is the housing area and h is the heat transfer coefficient in W/(m^2.$^\circ$C). The coefficient h is calculated through an empirical thermal model, assuming a TEFC structure [53]. The fluid velocity at the surface of the housing, required for calculation of h, is roughly approximated to be 10, 15, 20, and 30 m/s for 1, 10, 50, and 100 kW machines rotating at 3000 rpm, based on the experimental data available for induction motors. Also, the outer area of the stator core is roughly taken as the housing area.

Once the core temperature is known, the winding hot spot temperature can be obtained from (15) to ensure that it is below the maximum permissible temperature for the insulation. Otherwise, the individual is discarded.

$$T_{spot} = T_{core} + \left(\rho_{th,spot}/L_{stack}\right) \times P_{Cu} \tag{15}$$

Eventually, the cost of the materials, C_m, and their weight, M_{tot}, are calculated, as well as the cost of losses, C_e. The GA objective is to minimize both quantities.

3.4.2. Optimal design of the PM LTM

Although both the flat and tubular PM linear machines have been practically employed for buoys, here the PM linear machine with tubular structure is considered as the benchmark against which the MITROMAG is compared because of the similarity of its structure to the TROMAG. In this structure there are no end windings, which is an advantage over a flat structure.

The approach taken here for optimal design of a PM LTM, similar to the rotary IPM, is the use of 2D thermal and magnetic FEA for evaluation of each individual generated by the GA. To enable a fair comparison with the rotary machine, a similar thermal analysis is performed, assuming the same air velocities over the stator core of the LTM as those of the rotary IPM. Note, however, that incorporating the efficiency in the cost calculation results in the current density being mainly capped by the efficiency-tied cost of the system, not by the temperature limit.

3.4.2.1. Design constraints, constants, and variables of the PM LTM

Design constraints of the LTM are the same as those of the MITROMAG: the speed is set at 1 m/s for all designs, and four levels of force are considered: 1 kN, 10 kN, 50 kN, and 100 kN. The winding maximum temperature is limited to 180 $^{\circ}$C. No restrictions are posed on the radius and length of the machine.

An LTM is shown in Fig. 42 along with its geometrical design variables. Given the tubular structure of the machine, only full pitch windings with one slot per pole per phase are considered [54]. The selected design variables are the rotor outer radius, R_m; pole pitch, τ_P; magnet thickness, h_M; magnet coverage (ratio of magnet width to pole pitch τ_m / τ_P), α; tooth width, W_t; winding height, h_W; slot opening, b_0; slot tip height, H_{s0}; slot wedge height, H_{s1}; translator core thickness, d_{ct}; stator core thickness, d_{cs}; and the conductor current density, J. Lamination material and thickness, stack factor, magnet material, cost of material and electricity, air gap length, and the ambient temperature are assumed equal to the corresponding values for the rotary IPM.

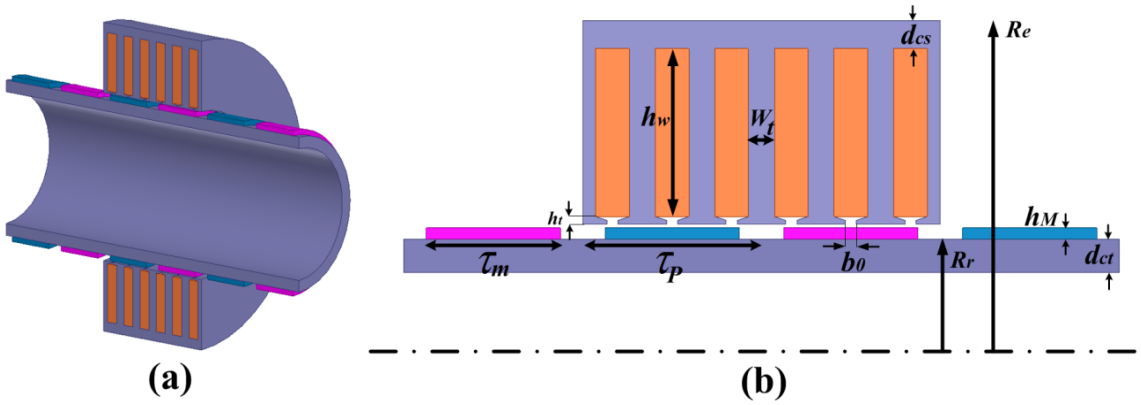

Fig. 42. A PM LTM. (a) cut-away view. (b) 2D view with geometrical design parameters.

3.4.2.2. Design procedure of the PM LTM

Similar to the rotary IPM, the first step of evaluating each individual is to create its slot geometry and populate the slots to obtain the conductor fill factor. Thermal FEA is then run and the thermal resistivity between the slot and core is calculated. By knowing the current density of the individual and its conductor fill factor, the copper losses of one pole is calculated. Low speed of the motion implies negligible iron losses; hence, only the copper losses are accounted for in calculating the winding hot spot temperature and ensuring that the insulation thermal limit is respected.

In the next step, geometry of one pole of the machine is created in axis-symmetric magnetic FEA and phase currents and anti-periodic boundary conditions are applied. Afterward, the translator is moved by one slot pitch and the average force generated by one pole, F_{pole}, is calculated. Moreover, the flux density vector is extracted for iron loss calculations.

By knowing F_{pole}, the total number of poles required to achieve the desired force can be obtained. Eventually, the total weight and cost of iron, copper, and magnet are calculated. Losses are incorporated in total cost calculation considering a five-year time period.

3.4.3. Comparison of the MITROMAG and the PM LTM

Fig. 43 and Fig. 44 show the force per cost and force per weight of the TROMAG of Table 1 versus magnet thickness and magnet coverage, assuming no stroke. The last assumption makes the plots independent from the force for which the design is performed. Contour plots are also presented to better illustrate the ranges of magnet thickness and coverage for optimum material cost and weight. Core thickness is set at 10 mm for both the rotor and translator. A maximum of 47 N/$ is achieved for the force per cost with 2.2 mm thick magnets and 70% coverage. The force per weight for the given magnet thickness and coverage works out to 0.7 kN/kg. On the other hand, maximum force per weight of 1 kN/kg occurs when magnets turn out to be 4.9 mm thick and cover 90% of the pitch. Such a design would result in force per cost of 34 N/$. It must be noticed, however, that with the assumed efficiencies, the cost of electricity associated with losses dominates the material cost. For the case of 125 kN TROMAG, assuming that it operates at 100 kW, 5% loss translates to about $11,000 over five years, whereas the material cost assuming 34 N/$ would be only $3,700. Therefore, under the made assumptions, designs that minimize the weight can be picked without significantly compromising the overall cost.

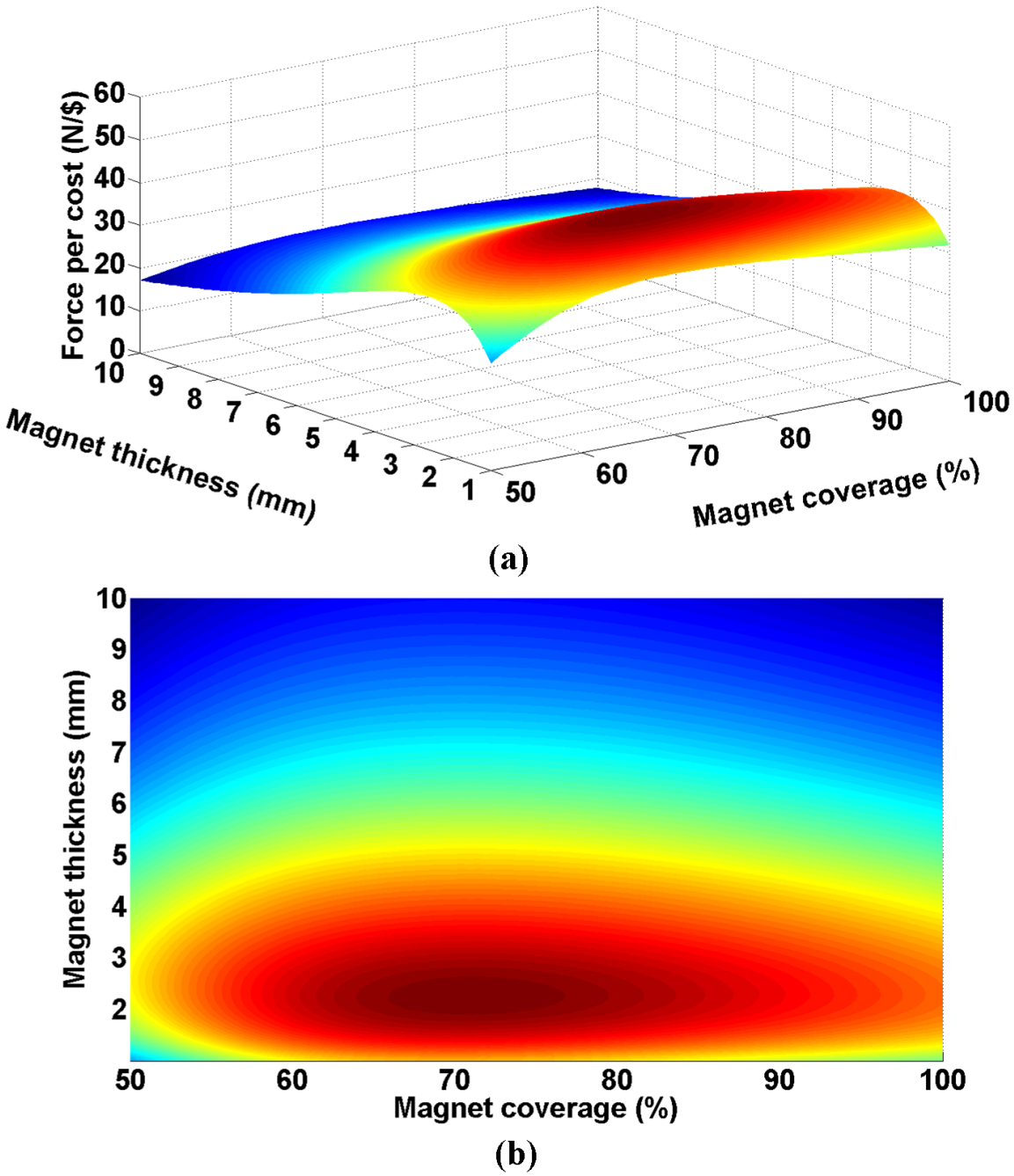

Fig. 43. Variations of force per cost of a TROMAG with zero stroke. (a) force per cost vs. magnet thickness and coverage. (b) contour plot of (a).

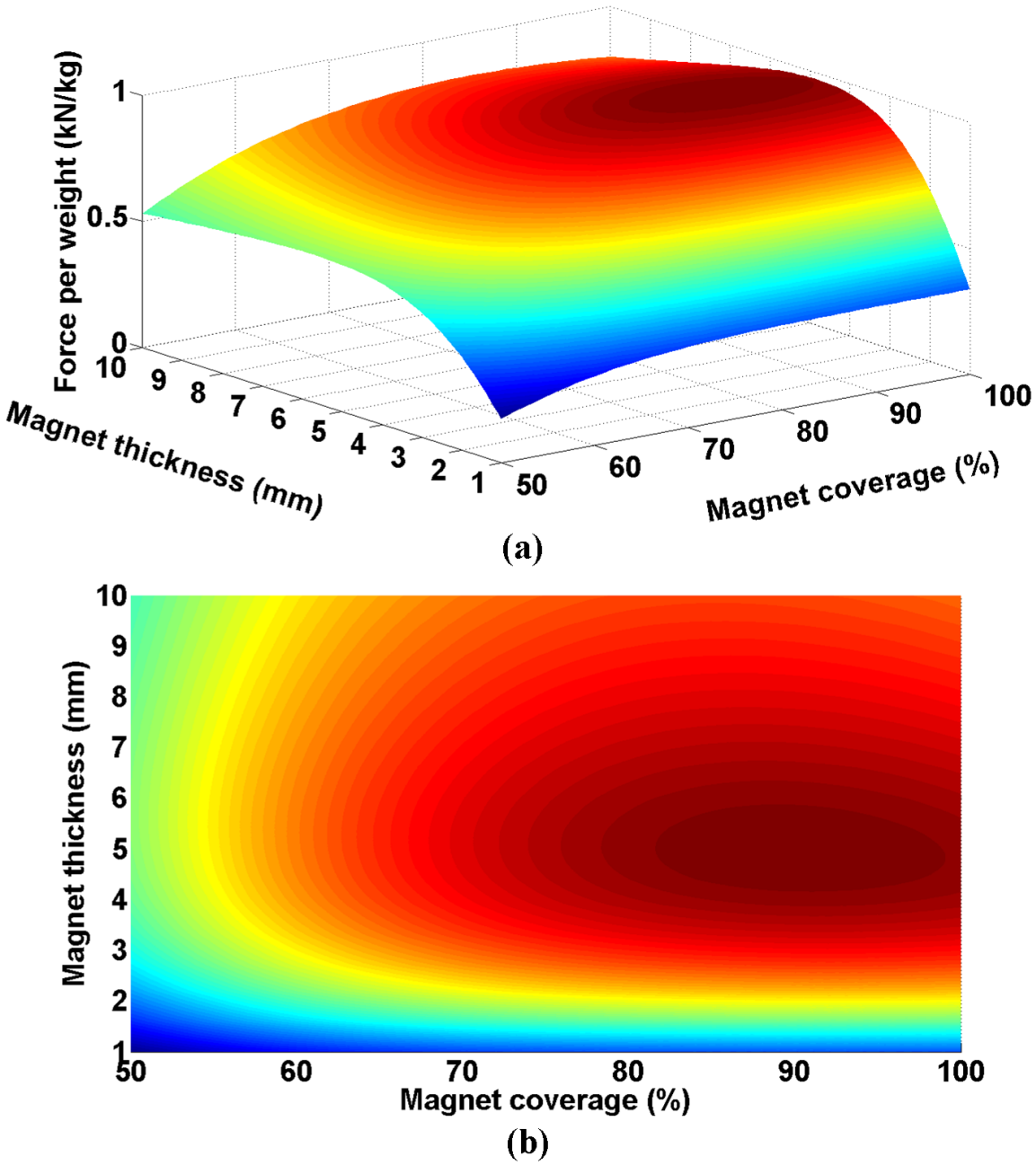

Fig. 44. Variations of force per weight of a TROMAG with zero stroke. (a) force per weight vs. magnet thickness and coverage. (b) contour plot of (a).

When accounting for the stroke, the individual values of radius and length affect the material weight and cost, and the optimum design would depend on the desired pull-out force as well. For 125 kN pull-out force, stroke of 1 m, and rotor length to radius ratio of 12, the optimum values of the magnet thickness, magnet coverage, and active length of the device (the length of the shorter part) to minimize the cost are 1.9 mm, 70%, and 1.5 m, respectively. This design results in force per cost of 35 N/$ and force per weight of 0.44 kN/kg. To minimize the weight, the optimum values are 4.5 mm, 90%, and 1.1 m, which yield force per cost of 24 N/$ and force per weight of 0.65 kN/kg.

Compared to the case of zero stroke, the optimum values of magnet thickness and coverage have slightly changed and the increase in weight and cost is noticeable. In the presented case, the stroke is not very different from the optimum values for the active length. As the stroke increases, the cost and weight associated with it would gradually overshadow those of the magnetically engaged part (active length). Design details of the 125 kN TROMAG, above, for the cases of optimum cost and optimum weight are summarized in Table 2. Note that subscript "*a*" denotes the association of a quantity with the active material, that is, material which is magnetically engaged and is not used to provide the stroke. L_a, M_a, and C_a denote the length, mass, and cost of the magnetically engaged parts, while M_{stroke} and C_{stroke} denote the weight and cost associated with the material added to provide the stroke. C_e signifies the cost pertinent to losses, and C_{tot} represents the total cost. To calculate the volume, V_{tot}, largest length and radius of the design are considered.

Optimal design of rotary IPM for 100/(100π) kN.m is performed through the GA over 20 generations of 200 individuals. The Pareto-optimal front is shown in Fig. 45. The conflict of cost and weight as optimization objectives is clearly observed.

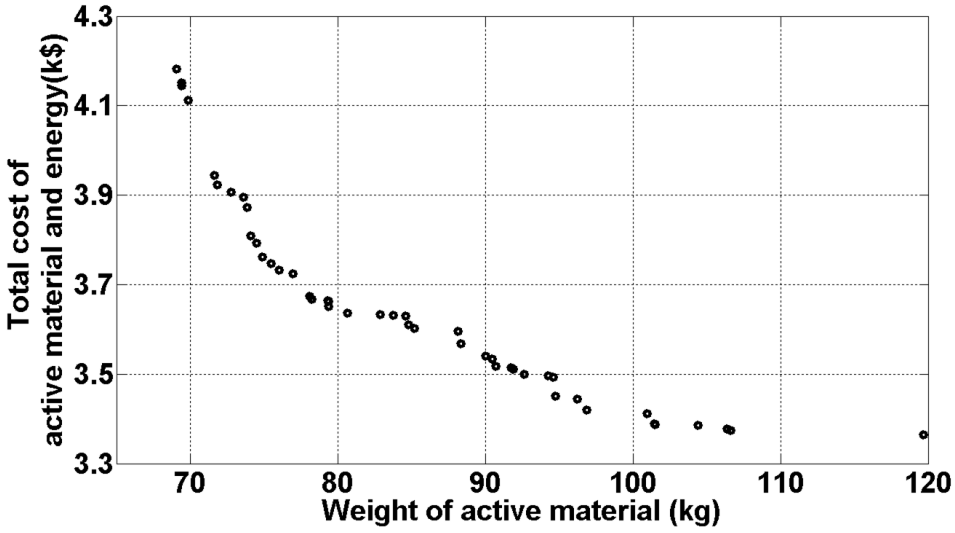

Fig. 45. Pareto-optimal front of the 100 kW rotary IPM.

Three designs are picked from the Pareto-optimal front: a design with low cost, a design with low weight, and a design which exhibits a compromise between the two objectives. Main details of the three designs are presented in Table 3 along with their corresponding weight, cost, and efficiency. C_m denotes the cost of the active material. For IPM #2, a populated slot and its temperature distribution for an arbitrary current density of 12 A/mm^2 (obtained from thermal FEA) is shown in Fig. 46, as well as the design geometry and mesh in magnetic FEA.

Table 2. Design details of a 125 kN TROMAG with 1 mm air gap, 1 m stroke, and length to radius ratio of 12

	Optimum cost	Optimum weight
h_M (mm)	1.9	4.5
α	0.7	0.9
R_m (mm)	126	88
L_a(m)	1.5	1.1
F/C (N/$)	35	24
F/W (N/kg)	441	650
V_{tot} (Lit)	151	69
M_a (kg)	210	127
M_{stroke} (kg)	73	66
M_{tot} (kg)	283	192
C_a (k$)	2.7	3.5
C_{stroke} (k$)	0.9	1.7
C_e (k$)	10.9	10.9
C_{tot} (k$)	14.5	16.1

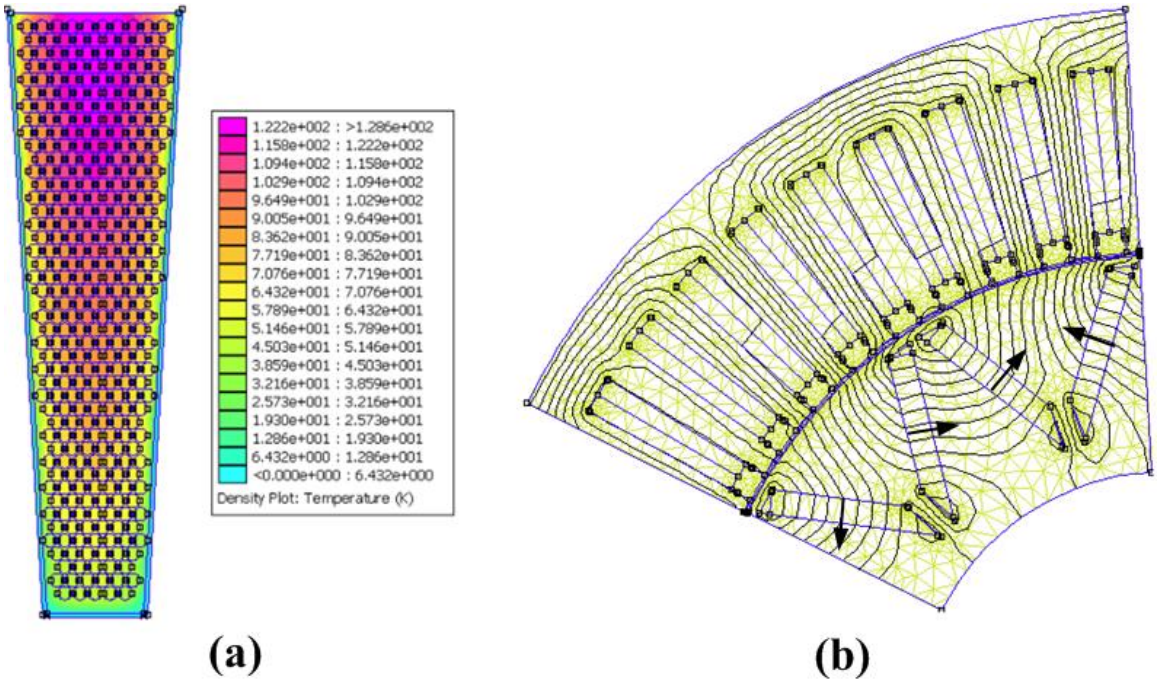

Fig. 46. Thermal and magnetic FEA of IPM design #2. (a) a populated slot and its temperature distribution. (b) mesh and flux lines in magnetic FEA.

Weight and cost of the three IPM designs presented in Table 3 are added to those of a 125 kN TROMAG with 1 m stroke to yield the total MITROMAG cost and weight. For the TROMAG, design with optimum weight is picked. Results, graphically presented in Fig. 47, are given in Table 4. Note that at this force level, while the rotary machine has a weight comparable to that of the TROMAG, its contribution to the overall cost of a MITROMAG is less significant. The reason lies within the extensive use of costly rare-earth magnet material by the TROMAG, as opposed to the dominance of iron and copper in the IPM design. Also, the magnetically engaged material dominates the material used for the stroke. Moreover, for both the TROMAG and IPM, loss-related cost is noticeably greater than the material cost.

Table 3. Design details of three optimally designed IPM from the Pareto-optimal front

IPM Design #	1	2	3
N_S , N_P	36 , 8	54 , 12	72 , 12
R_{ri} (mm)	48.3	61.7	44.0
R_{ro} (mm)	170	175.1	151.8
h_M (mm)	6.1	6.1	6.3
SR	1.4	1.3	1.4
W_t (mm)	9.9	7.1	4.1
d_{cs} (mm)	19.7	14.2	10.2
b_0 (mm)	7.2	7.2	4.9
H_{s0} (mm)	3.1	3.2	2.6
H_{s1} (mm)	1.5	1.6	2.6
J (A/mm^2)	4.4	4.7	5.7
K_f	0.56	0.59	0.56
eff (%)	98.9	98.8	98.6
V_{tot} (Lit)	16.5	13.1	11.7
M_{tot} (kg)	105	79	70
C_m (k$)	1.1	1.0	1.0
C_e (k$)	2.3	2.7	3.1
C_{tot} (k$)	3.4	3.7	4.1

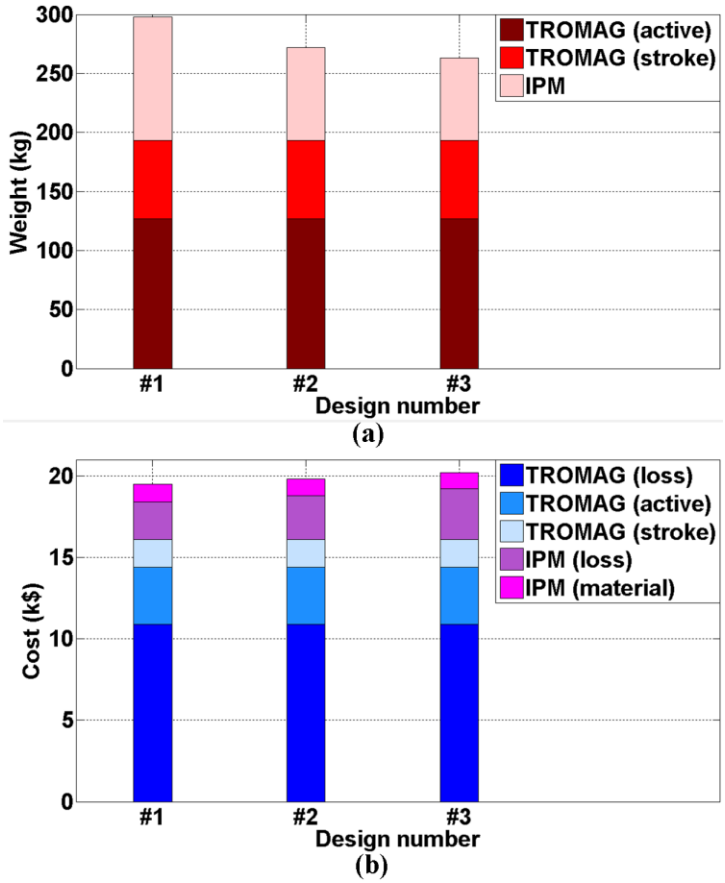

Fig. 47. Weights and costs of three designs of a 100 kW MITROMAG. (a) weight of active and stroke material. (b) cost of active and stroke material and energy.

Table 4. Volume, weight, and cost of three 100 kW MITROMAGs corresponding to optimum IPMs of Table 3

Design #	#1	#2	#3
V_{tot} (Lit)	85.5	82.1	80.7
M_{eng} (kg)	231.5	206.2	197.1
M_{stroke} (kg)	66	66	66
M_{tot} (kg)	297.5	272.2	263.1
C_{eng} (k$)	4.6	4.5	4.5
C_{stroke} (k$)	1.7	1.7	1.7
C_e (k$)	13.2	13.6	14.0
C_{tot} (k$)	19.5	19.8	20.2

Similarly, an LTM is optimally designed for 100 kN and 1 m stroke. Minimum core thickness for both stator and translator is set at 10 mm. Table 5 presents details of three designs picked from the Pareto-optimal front, and Fig. 48 shows LTM#2 in magnetic FEA. For better clarification, weights and costs of the three LTM designs are shown in Fig. 49. Clearly, less costly designs use lower current density to reduce the loss-related cost. Moreover, they tend to have larger radius, longer pole pitch, and larger volume. Lighter designs are longer and more compact, with higher current density and lower efficiency. The winding temperature approaches the maximum permissible value for lighter designs; but for cost effective designs, it remains well below that value.

It is also interesting to learn that, in contrast to the TROMAG, the cost and weight associated with the material required for the stroke is very small compared to those of the magnetically engaged material. In addition to very large shear stress of a TROMAG compared to that of a PM LTM, this is due to the fact that length-to-radius ratio of the LTM is not restricted, and the Pareto-optimal designs tend to have large lengths, several times the stroke. Comparing Table 4 and Table 5 clearly indicates the superiority of the MITROMAG over the LTM. For example, in Design #1, the MITROMAG is an order of magnitude lighter and more compact than the corresponding LTM, while its cost is less than one-half that of the LTM. Also notice that inactive material required for maintaining the air gap is not considered when comparing the weights of the two systems. As mentioned earlier in Section 1.3, for large direct drive systems, the inactive material could contribute the most to the system's total weight. Since MITROMAG is

much lighter and more compact, it is likely to need less inactive material compared to the LTM; thus, its overall weight would be further reduced.

Table 5. Design details of three optimally designed LTM from the Pareto-optimal front

LTM	1	2	3
R_m (mm)	161	160	93.5
τ_P (mm)	48.6	37.3	30
h_M (mm)	5.2	3.6	4.5
α	0.84	0.68	0.74
W_t (mm)	8.0	5.3	4.4
h_W (mm)	77.4	32.0	35.9
b_0 (mm)	2.5	3.2	3.3
H_{s0} (mm)	0.6	0.8	0.6
H_{s1} (mm)	2.0	2.1	0.8
d_{ct} (mm)	13.1	10	10
d_{cs} (mm)	10	10	10
J (A/mm^2)	2.0	4.2	6.5
K_f	0.55	0.48	0.49
F_{pole} (N)	1404	796	685
eff (%)	88.3	78.1	64.0
V_{tot} (Lit)	897	764	344
M_{eng} (kg)	2973	1862	1178
M_{stroke} (kg)	123	89	53
M_{tot} (kg)	3096	1951	1231
C_{eng} (k$)	23.0	15.1	10.4
C_{stroke} (k$)	3.2	1.9	1.4
C_e (k$)	25.6	48.1	78.7
C_{tot} (k$)	51.8	65.1	90.5
T_{spot} ($^\circ$C)	66	91	167

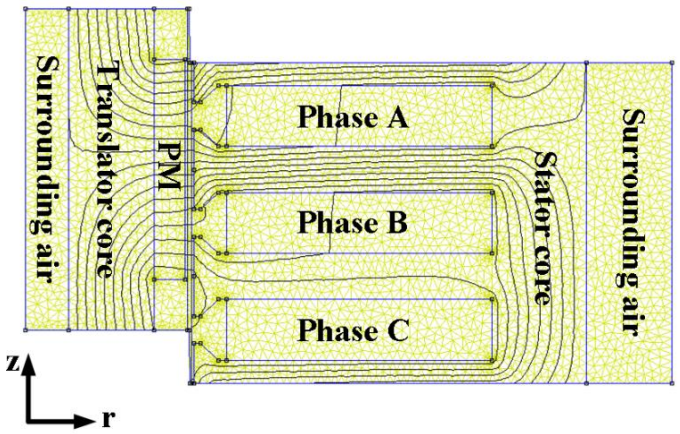

Fig. 48. Mesh and flux lines of LTM design #2 in magnetic FEA.

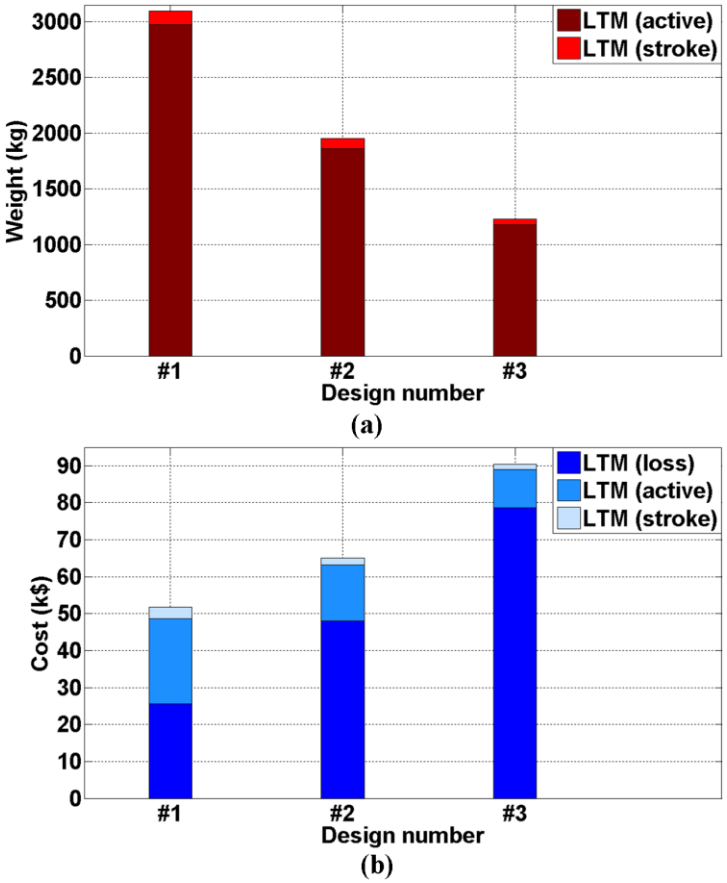

Fig. 49. Weights and costs of the active material of three designs of a 100 kW LTM. (a) weight. (b) cost.

Designs are repeated for power levels of 50, 10, and 1 kW for the same stroke and air gap length. Weight and cost of MITROMAG and LTM is compared in Fig. 50. As the force level decreases with the stroke length being constant, the MITROMAG significant margin of advantage over the LTM gradually shrinks. At 1 kN, for example, the stroke length of TROMAG turns out to be more than 10 times its magnetically engaged length. With the efficiency assumed for TROMAG at this force level, the MITROMAG cost approaches that of the LTM, although its weight and volume are still lower than those of the LTM.

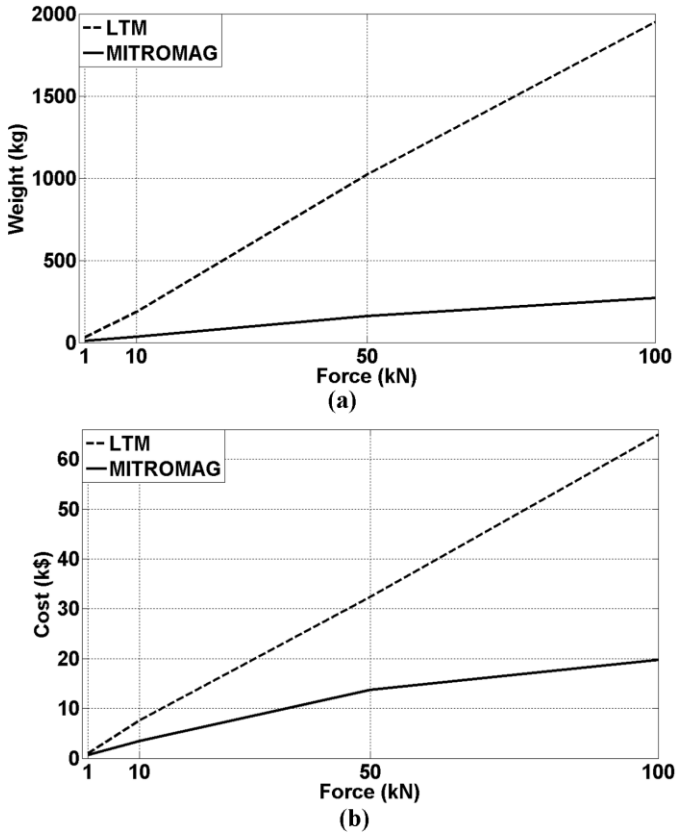

Fig. 50. Comparison of MITROMAG and PM LTM at four levels of force with similar speed and stroke. (a) weight. (b) cost.

3.5. Summary

Aspects of magnetic design of the TROMAG were investigated in this chapter. Scaling rules of the TROMAG were presented. Also, 3D FEA was employed to study the influence of the helix non-ideality. It was shown that a discretized helix, formed by a low number of segments, far from an ideal one, would not only reduce the force transmission capability of the device but also change the force characteristic waveform and make the gear ratio load-dependent.

The 2D model of the TROMAG was shown to closely approximate the force. An analytical model, derived from solving the Laplace and Poisson's equations in a cylindrical coordinate system, was then used to sweep design variables, such as the pole pitch; magnet thickness; magnet coverage; and air gap length, and study their effects on the pull-out force. It was observed that for a given magnet thickness and air gap length, there is a particular pole pitch that maximizes the shear stress. Moreover, the shear stress increases as the magnet thickness increases; however, the effect tends to saturate beyond a point. In addition, it was shown that for a given pole pitch and air gap length, there is a particular magnet coverage that minimizes the magnet material required to achieve a desired pull-out force.

Concerning demagnetization, 2D FEA was employed to study the flux density in the magnets. It was shown that to avoid demagnetization of the magnets, they should be of the same thickness and material grade.

A formula was presented for calculating the required core thickness to achieve a desired flux density in the core. The formula is derived from the 2D model of the TROMAG, and its predictions are in very close agreement with 2D FEA.

Eventually, design of a MITROMAG for several values of force was performed. A population-based GA was used for optimal design of the rotary machine to be used with the TROMAG. Each individual was evaluated by using 2D magnetic and thermal FEA. The same method was adopted to optimally design a PM LTM for the same values of force and speed. The weight, volume, and cost of the required active material were compared for the two systems, and the comparison revealed the superiority of the MITROMAG.

4. DYNAMIC MODELING OF THE TROMAG

4.1. Introduction

Controlling the motion of a drive train that includes the TROMAG entails knowledge of the dynamic behavior of this device. This chapter, therefore, proposes a nonlinear analytical model for describing the TROMAG dynamics. Then the model is linearized about a stable equilibrium point.

Examples are given about how the proposed model can be employed to analyze the drive trains that include the TROMAG. The equation of motion for the rotor and translator in a motoring mode drive train are developed. Moreover, to show the effectiveness of the model, its prediction of the TROMAG behavior in a rotor oscillation test is compared with that of a 3D FEA.

Furthermore, the linearized model of a buoy is presented along with a brief explanation of the main control strategies adopted for these energy conversion systems. Eventually, to investigate the changes that the system dynamics undergo upon replacing a DDLG with a MITROMAG, the linearized model of the TROMAG is combined with that of the buoy, and the characteristics of the entire system are studied. The control strategy and the incident wave determine the force by which the PTO has to react to the wave (referred to as the "reference translator force" or the "reference force" hereafter). In a PTO that contains a vector-controlled DDLG, the translator force is linearly proportional to the force-generating component of the stator current, i_q [55]. Therefore, after the reference force is determined, it can be generated simply by controlling i_q.

When a MITROMAG forms the PTO, the reference force has to be tracked by the translator of the TROMAG. However, what can be directly controlled through the power electronics converter is the rotary generator torque. Although the generator torque can be set to a desired value simply by controlling the torque generating component of its current, the resultant torque is not related to the translator force through a simple proportionality factor. It is shown in this chapter that, upon linearization, a 4^{th} order transfer function relates the generator torque to the translator force.

4.2. Dynamic model of a TROMAG

4.2.1. Analytical model

Fig. 51 shows the force and torque characteristics of the TROMAG whose parameters are given in Table 1, assuming that it has a right-handed helix. The characteristics cross zero at two points, both of which are referred to as the equilibrium points. The equilibrium point at rotor position of 0° corresponds to the relative position of the rotor and translator in which magnets of the same polarity on the two parts are fully aligned, similar to Fig. 35(a). The equilibrium point at rotor position of 180° corresponds to the relative position of the rotor and translator in which magnets of the same polarity on the two parts are fully unaligned, similar to Fig. 35(c). While the former equilibrium point is stable, the latter one is unstable.

Similar to field-modulated magnetic gears, from a dynamic viewpoint, a TROMAG may be looked upon as a spring with non-linear stiffness [56]. Based on the models developed for drive trains with non-infinitely stiff couplings [15], magnetic

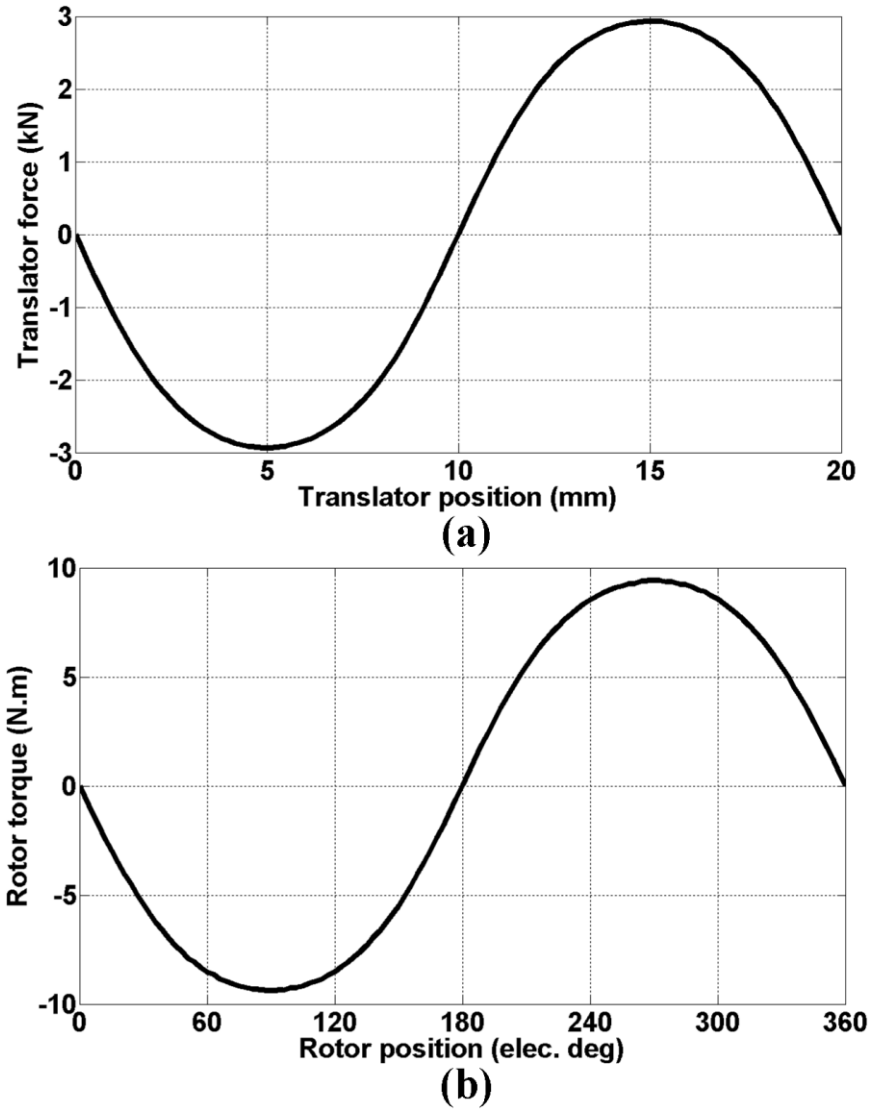

Fig. 51. Characteristics of the TROMAG of Table 1 with a right-handed helix. (a) rotor torque. (b) translator force.

couplings [16], and magnetic gears [17], the following nonlinear model can be proposed for a 2-pole TROMAG.

$$T_r = -T_m \sin(\theta + Gz) \tag{16-a}$$

$$F_t = GT_r = -GT_m \sin(\theta + Gz) \tag{16-a}$$

In (16), θ and z are the rotor and translator positions with respect to a stable equilibrium point, respectively, and $\theta+Gz$ indicates the relative position between the rotor and translator. The stable and unstable equilibrium points are located at $\theta+Gz=0^{\circ}$ and $\theta+Gz=180^{\circ}$, respectively.

The proposed nonlinear model can be linearized about the stable equilibrium point. By doing so, further insight can be gained into the system dynamics. Moreover, the TROMAG model can be represented in the Laplace domain. The linear model is presented in (17).

$$T_r \cong -T_m(\theta + Gz) \tag{17-a}$$

$$F_t = GT_r \cong -GT_m(\theta + Gz) \tag{17-a}$$

4.2.2. TROMAG in a motoring mode drive train

As an example, a drive train consisting of a TROMAG, a rotary electric motor, and a translating load is considered. The rotary motor drives the rotor of the TROMAG by applying the torque, T_{mot}, and the translator of the TROMAG propels a load force, F_L. The equations of motion of the rotor and translator, assuming that the damping torque can be expressed as linearly proportional to the rotor speed and that the damping force can be expressed as linearly proportional to the translator speed, are given in (18-a) and (18-b), respectively. J is the total moment of inertia of the rotating parts, M_t is the total mass of the translating parts, B_r is the damping coefficient associated with rotation of the rotors, accounting for friction and eddy currents, and B_t is the damping coefficient

associated with the translation of the translator and load. The single upper dot indicates first time derivative, and the double upper dots indicate second time derivative.

$$T_{mot} + T_r = J\ddot{\theta} + B_r\dot{\theta} \tag{18-a}$$

$$F_t + F_L = M_t\ddot{z} + B_t\dot{z} \tag{18-b}$$

By substituting (16) in (18), the system dynamics can be represented through a set of nonlinear second order differential equations as presented in (19).

$$T_{mot} - T_m \sin(\theta + Gz) = J\ddot{\theta} + B_r\dot{\theta} \tag{19-a}$$

$$-GT_m \sin(\theta + Gz) + F_L = M_t\ddot{z} + B_t\dot{z} \tag{19-b}$$

When the linearized dynamic model of the TROMAG is considered, the overall system dynamics can be obtained by substituting (17) in (18), as below:

$$T_{mot} - T_m(\theta + Gz) \cong J\ddot{\theta} + B_r\dot{\theta} \tag{20-a}$$

$$-GT_m(\theta + Gz) + F_L \cong M_t\ddot{z} + B_t\dot{z} \tag{20-b}$$

The system block diagram in the Laplace domain, by assuming zero initial conditions (zero position and speed), is depicted in Fig. 52. The motor torque can be thought of as the control effort through which the output, which can be the translator force and/or speed, is adjusted. The load force may be looked upon as a disturbance despite of which the output must track a reference value.

The transfer functions from the control effort and disturbance to the translator force, translator speed, and rotor speed are presented in (21) to (27).

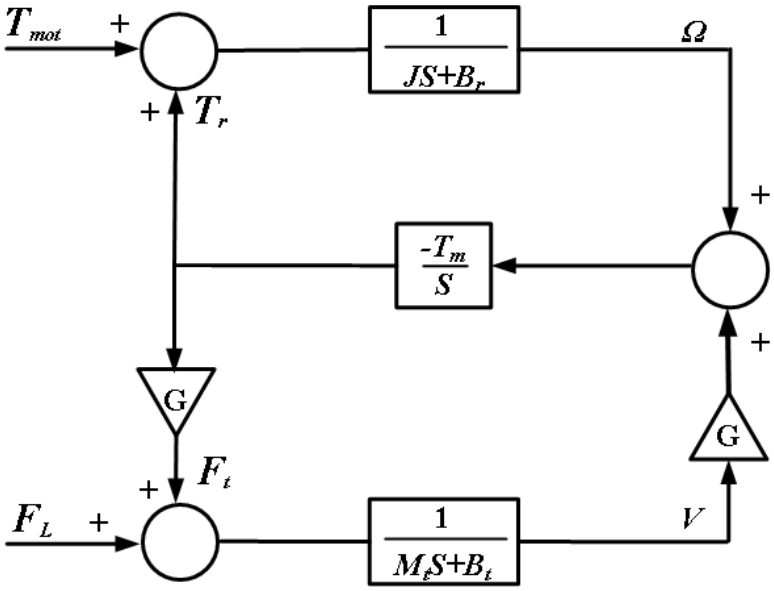

Fig. 52. Block diagram of the drive train consisting of a TROMAG, a rotary motor, and a load.

$$\frac{F_t}{T_{mot}} = -GT_m \frac{M_tS + B_t}{den(S)} \tag{21}$$

$$\frac{\mathrm{V}}{T_{mot}} = -\frac{GT_m}{den(S)} \tag{22}$$

$$\frac{\Omega}{T_{mot}} = \frac{M_tS^2 + B_tS + G^2T_m}{den(S)} \tag{23}$$

$$\frac{F_t}{F_L} = -G^2T_m \frac{JS + B_r}{den(S)} \tag{24}$$

$$\frac{\mathrm{V}}{F_L} = \frac{JS^2 + B_rS + T_m}{den(S)} \tag{25}$$

$$\frac{\Omega}{F_L} = -\frac{GT_m}{den(S)} \tag{26}$$

The system characteristic equation is:

$$den(S) = JM_tS^3 + (JB_t + M_tB_r)S^2 + \tag{27}$$

$$[(JG^2 + M_t)T_m + B_rB_t]S + (G^2B_r + B_t)T_m$$

If the damping coefficients are neglected, the characteristic equation is given by:

$$den(S) \cong JM_tS^3 + (JG^2 + M_t)T_mS \tag{28}$$

The TROMAG natural frequency, ω_n, then would be:

$$\omega_n = \sqrt{\left(\frac{1}{J} + \frac{G^2}{M_t}\right)T_m} \tag{29}$$

4.2.3. Oscillation tests on the TROMAG

As another example of how the proposed dynamic model can be used for predicting the TROMAG behavior, an oscillation test on the rotor is considered: the translator is locked at z=0, the rotor is pulled to a maximum torque position, $\theta(0)$=-π/2, and then it is released to freely oscillate until it settles down to a stable equilibrium point. By setting T_{mot}=0 in (19-a), the rotor equation of motion is obtained as a nonlinear, second order differential equation, which can be solved numerically.

$$\ddot{\theta} + \frac{B_r}{J}\dot{\theta} + \frac{T_m}{J}\sin\theta = 0; \quad \theta(0) = -\frac{\pi}{2}; \quad \dot{\theta}(0) = 0 \tag{30}$$

The outer part of the TROMAG detailed in Table 1 is defined as the rotor, and its moment of inertia and damping coefficient are set at 0.006 N.m.s^2 and 0.01 N.m.s, respectively. The rotor position during a rotor oscillation test is obtained from both 3D FEA and non-linear analytical model of (30), and the results are compared in Fig. 53. The rotor torque and translator force follow a pattern similar to that of the rotor position.

A very close agreement is observed between the nonlinear analytical model and 3D FEA results, except for when the rotor approaches its final position. The difference may be attributed to the fact that, in the FEA model, an ideal helix is replaced by a discretized helix in which small segments are placed, with a step displacement, next to each other to create an approximation of the ideal helix. Each small segment is a piece of a cylinder, so its arc follows a circular path instead of a helical path. As the amplitude of oscillation decays, the effect of step displacement between adjacent segments and circular approximation of a spiral become more visible.

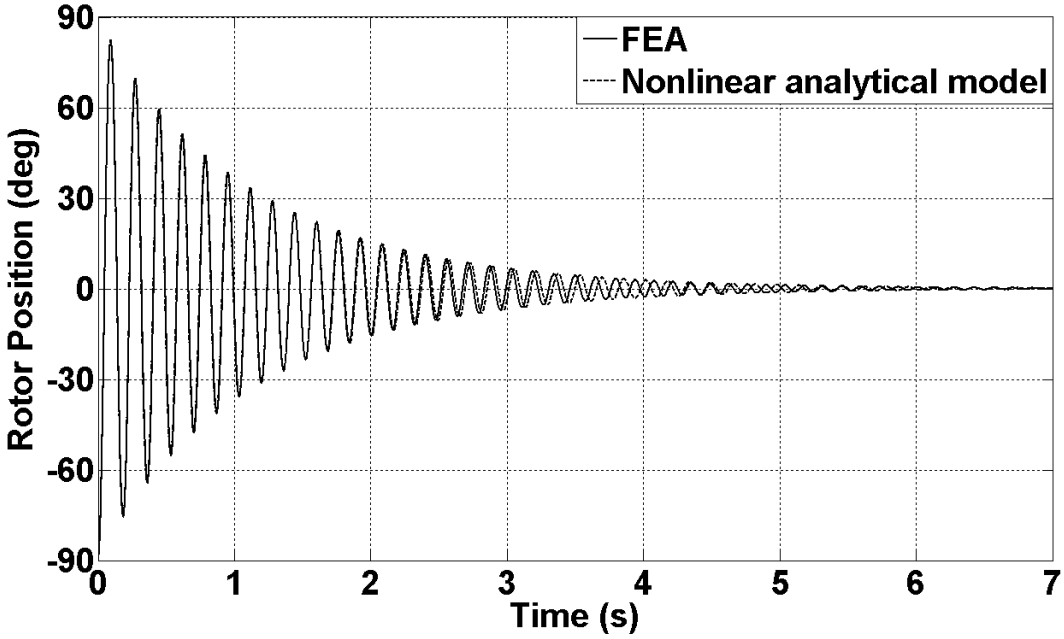

Fig. 53. Rotor position during a rotor oscillation test; comparison of the nonlinear analytical model and 3D FEA.

On the other hand, when the linearized model of the TROMAG is used, that is, by setting T_{mot}=0 in (20-a), the rotor equation of motion during a rotor oscillation test yields to a linear, second order differential equation presented in (31).

$$\ddot{\theta} + \frac{B_r}{J}\dot{\theta} + \frac{T_m}{J}\theta = 0; \quad \theta(0) = -\frac{\pi}{2}; \quad \dot{\theta}(0) = 0 \tag{31}$$

The closed form solution to (31) is given in (32).

$$\theta(t) = \theta(0)e^{-\alpha_r t}\left(\cos\beta_r t + \frac{B_r}{2J\beta_r}\sin\beta_r t\right);$$
$$\alpha_r = \frac{B_r}{2J}; \quad \beta_r = \frac{1}{2}\sqrt{\frac{4T_m}{J} - \left(\frac{B_r}{J}\right)^2}, \tag{32}$$

and the rotor torque is obtained from:

$$T_r(t) \cong -T_m\theta(t) \tag{33}$$

Fig. 54 compares the results of the linearized analytical model with the nonlinear analytical model for two different initial positions of rotor, -90° and -30°. For both initial positions the amplitude, frequency, and settling time of oscillation are the same for each of the two models. However, a large phase difference is observed between the results of the two models when the rotor starts from its maximum torque position. The cause lies within the large linearization error that appears when θ is farther from zero.

When damping is neglected, the rotor oscillates according to (34), where ω_r is the rotor oscillation frequency.

$$\theta(t) \cong \theta(0)\cos\omega_r t; \quad \omega_r = \sqrt{\frac{T_m}{J}} \tag{34}$$

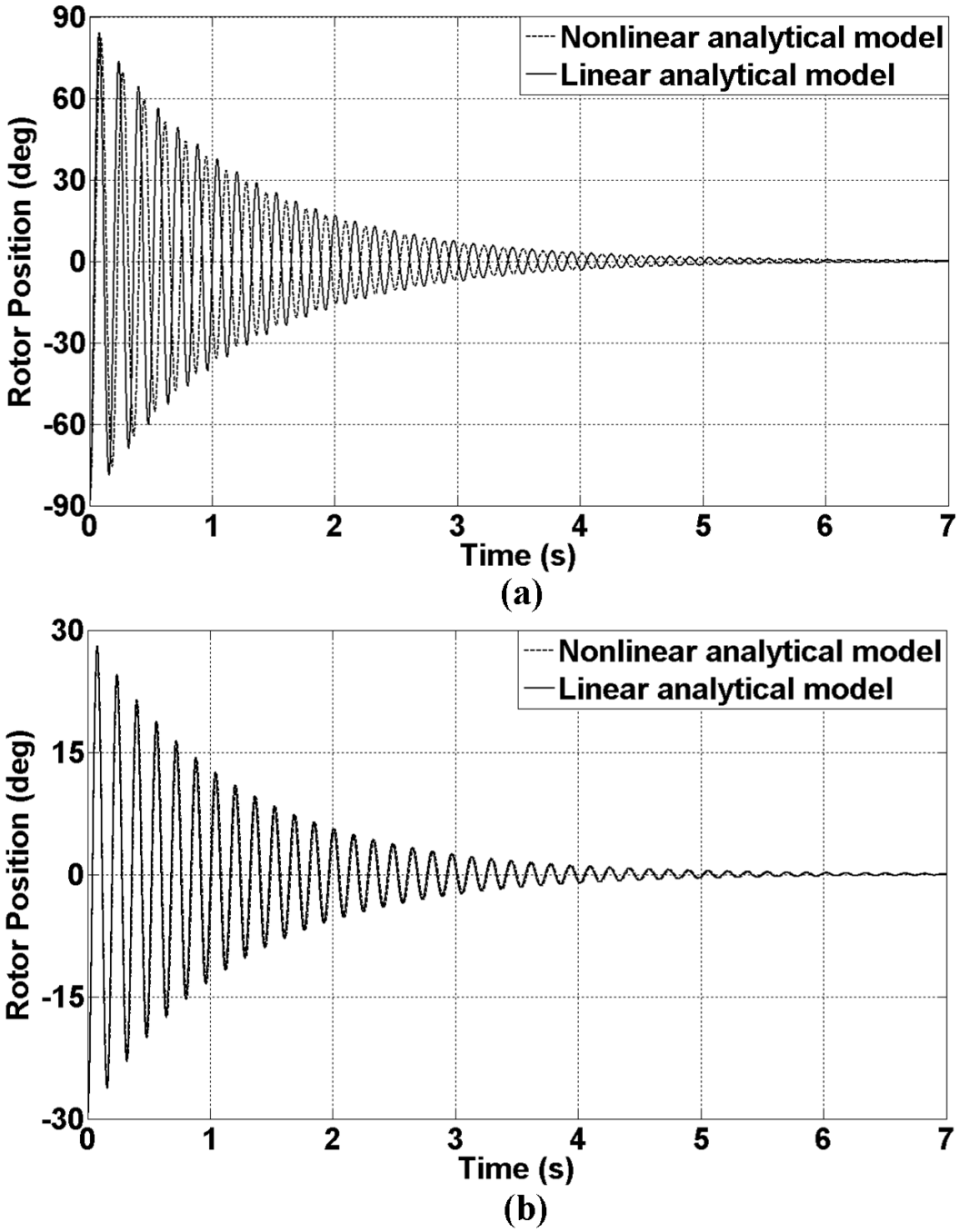

Fig. 54. Rotor position during a rotor oscillation test obtained from nonlinear and linearized analytical models. (a) rotor starting from -90 degrees. (b) rotor starting from -30 degrees.

Similarly, an oscillation test on the translator can be considered in which the rotor is locked at θ=0, the translator is pulled to a maximum force position, such as $z(0)=\tau_P/2$, and then it is released to oscillate freely (F_L=0) until it reaches a stable equilibrium point. Upon setting F_L=0 in (19-b) and (20-b), the nonlinear and linearized equations of motion of the translator can be obtained, as given in (35) and (36), respectively.

$$\ddot{z} + \frac{B_t}{M_t}\dot{z} + \frac{GT_m}{M_t}\sin(Gz) = 0; \quad z(0) = \frac{\tau_P}{2}; \quad \dot{z}(0) = 0; \tag{35}$$

$$\ddot{z} + \frac{B_t}{M_t}\dot{z} + \frac{G^2T_m}{M_t}z = 0; \quad z(0) = \frac{\tau_P}{2}; \quad \dot{z}(0) = 0 \tag{36}$$

The closed-form solution of the linearized equation (36) is given in (37):

$$\begin{gathered} z(t) = z(0)e^{-\alpha_t t}\left(\cos\beta_t t + \frac{\frac{B_t}{M} - \alpha_t}{\beta_t}\sin\beta_t t\right); \\ \alpha_t = \frac{B_t}{2M_t}; \quad \beta_t = \frac{1}{2}\sqrt{\frac{4G^2T_m}{M_t} - \left(\frac{B_t}{M_t}\right)^2} \end{gathered} \tag{37}$$

By assuming zero damping, that is, α_t=0, the translator equation of motion and its oscillation frequency, ω_t, work out to:

$$z(t) \cong z(0)\cos\omega_t t; \quad \omega_t = G\sqrt{\frac{T_m}{M_t}} \tag{38}$$

Notice that the TROMAG natural frequency, ω_n, is related to the rotor's oscillation frequency, ω_r, and the translator's oscillation frequency, ω_t, in the following form:

$$\omega_n^2 = \omega_r^2 + \omega_t^2 \tag{39}$$

4.3. Dynamic model of a buoy

Assuming plane progressive waves, infinite water depth, small motion amplitude, and a linearized system, the interaction of a buoy, waves, and the direct drive linear generator may be described as below [57], [58]:

$$F_w + F_g = (m + A)\ddot{z}_b + (B_{rad} + B_v)\dot{z}_b + Kz_b \tag{40}$$

In (40), z_b is the buoy position with respect to the mean surface level, F_w is the wave excitation force, F_g is the generator force opposing the wave force, m is the buoy mass, and A signifies the added mass. The added mass models the extra force required to move the body in water when compared to moving it in air. B_{rad} is called radiation resistance [57] or intrinsic resistance [12] and models the power radiated back to the water by the radiated waves while B_v is the viscous resistance. Both the added mass and radiation resistance vary with the wave frequency. K is the hydrostatic stiffness, and Kz_b models the buoyancy force of the buoy.

For simplicity, the definitions $m+A \equiv M$ and $B_{rad}+B_v \equiv B$ are made. B can be called the mechanical damping coefficient [59]. Assuming a monochromatic wave climate (steady state sinusoidal wave with a single frequency component) and approximating frequency-dependent terms of $A(\omega)$ and $B_{rad}(\omega)$ with constants A and B, (40) can be written in phasor form as in (41) [11]. In (41), phasors are indicated by an upper dash, ω is the wave frequency, and $\bar{V}$ is the phasor of the buoy speed.

$$\bar{F}_w + \bar{F}_g = j\omega M\bar{V} + B\bar{V} + (K/j\omega)\bar{V} \tag{41}$$

The equivalent circuit and the block diagram representing (41) are shown in Fig. 55. In this circuit, the voltage and current are analogous to the force and speed, respectively. The resistance, inductance, and inverse of capacitance are also analogous to the mechanical damping, mass, and hydrostatic stiffness, respectively.

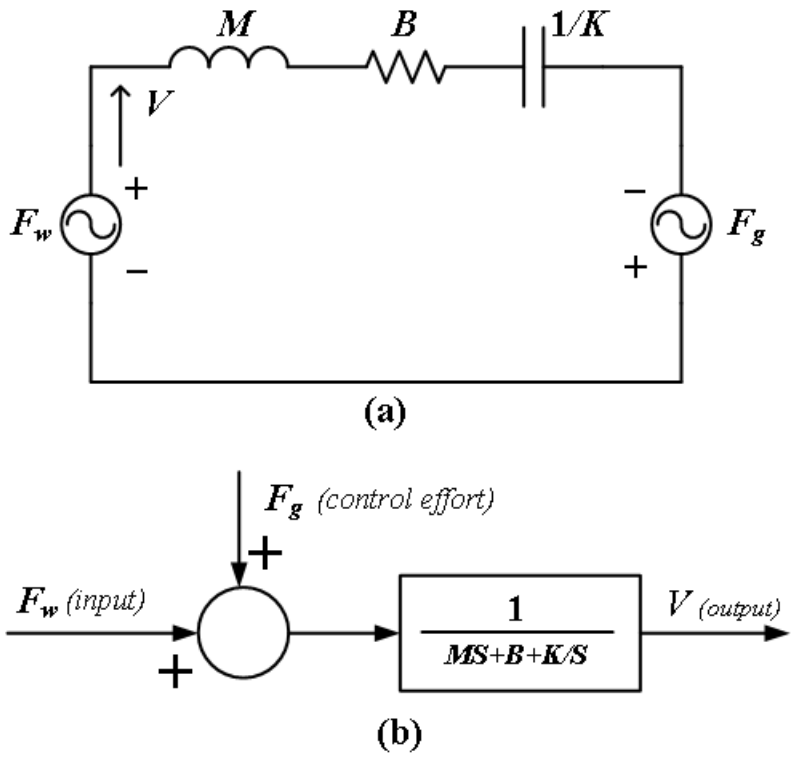

Fig. 55. Interaction of a buoy and a generator. (a) equivalent circuit. (b) block diagram representation.

The equivalent impedance of the buoy, Z_b, is called the hydrodynamic impedance [11] or intrinsic impedance [12] of the buoy:

$$\bar{Z}_b = B + j\omega M + \frac{K}{j\omega} = B + j(\omega M - K/\omega) \tag{42}$$

Then the natural frequency of the buoy, the frequency at which the reactive term of the intrinsic impedance is zero, is given by:

$$\omega_b = \sqrt{\frac{K}{M}} \tag{43}$$

The desired generator force is set according to the control strategy. To maximize the absorbed power from an incident wave (while respecting the system constraints such as velocity, stroke, and rating of the PTO), the force with which the buoy reacts to the wave excitation force must be properly controlled. The desired amplitude and phase of the buoy force (the reference force) is determined by the adopted control strategy. Generally, the control strategies for buoys can be divided into two main groups: reactive control and resistive damping control [11]. The reactive control method is also called optimal control, as it results in maximization of the absorbed power from the incident wave. The power extracted from an incident wave is maximized when the natural frequency of the buoy matches the frequency of the incident wave; that is, resonance occurs between the buoy and the wave. Given the low frequency of the ocean waves, buoys would be prohibitively heavy to fulfill this requirement [60], [61]. Therefore, in practice, the PTO is controlled in such a manner as to cause the resonance. To that end, the generator force must be set such that the equivalent impedance seen by the source (wave force) is purely resistive so the absorbed power from the incoming wave becomes

maximized. To achieve this goal, the generator equivalent impedance, $\bar{Z}_g$, must equal the complex conjugate of the buoy intrinsic impedance.

$$\bar{Z}_g = \bar{Z}_b^* \tag{44}$$

Consequently, the generator hydrodynamic reactance, $X_g=M_g\omega-K_g/\omega$, would cancel the intrinsic reactance of the buoy. The reference generator force that yields such a condition is then:

$$\bar{F}_{g,ref} = \bar{Z}_b^* \bar{V} \tag{45}$$

This condition results in a purely resistive load seen by the wave excitation force, and, therefore, the wave excitation force would be in phase with the buoy velocity (unity mechanical power factor); hence, maximum power would be absorbed from the incident wave. Since one of the requirements to fulfill (45) is to set $B_g=B$, the buoy speed in this condition is given by:

$$\bar{V} = \bar{F}_w/(2B) \tag{46}$$

By substituting (46) in (45), the reference force that the generator has to track equals:

$$\bar{F}_{g,ref} = -\frac{1}{2B}[B - j(\omega M - K/\omega)]\bar{F}_w \tag{47}$$

Although this method maximizes the power absorbed from an incident wave, it entails bi-directional flow of power between the buoy and the PTO, as well as large energy storage requirement, large peak-to-average power ratio for the PTO, and large ratio of PTO force to incident wave force [11]. On the other hand, in the resistive damping control strategies such as amplitude control [12] and phase control [60],

although the absorbed power is not maximized, the PTO rating, velocity, and stroke are significantly reduced compared to the reactive control method. In the amplitude control strategy, also referred to as the passive loading [59], resistive loading [12], and non-reactive damping [62], the reference of the generator force is set proportional to the buoy velocity [12], so those two quantities are always in phase.

$$\bar{F}_g = B_g \bar{V} \tag{48}$$

Therefore, the power of PTO always holds the same sign; in other words, the power flows only from the ocean to the PTO, and no reactive power is involved. It can be shown that under the condition of zero reactive power, the optimum proportionality factor, B_g, which results in maximum power absorption from the incident wave equals the magnitude of the buoy intrinsic impedance.

$$B_g = |Z_b| = \sqrt{B^2 + \left(\omega M - \frac{K}{\omega}\right)^2} = B\sqrt{1 + \left(\frac{\omega M - \frac{K}{\omega}}{B}\right)^2}\ ; \tag{49}$$

$$M_g = 0; \quad K_g = 0$$

For this study, the L10 buoy developed at the Oregon State University has been picked. Although some of the buoy parameters vary with wave frequency, in this study it was decided to consider only the effect of TROMAG parameters on the system characteristics. Therefore, frequency-independent parameters B=5000 N.s/m, M=11492 kg, and K=96743 N/m are considered as the rated values. The rated force and the stroke are assumed to be 50 kN and 1 m, respectively [63]. From (43), the natural frequency of the buoy works out to 2.9 rad/s.

4.4. Characteristics of the system comprising a MITROMAG and a buoy

4.4.1. Dynamic model and transfer functions

The model of the entire system, consisting of a MITROMAG and a buoy, is developed by replacing the generator force F_g in (41) with the translator force of the TROMAG F_t. The open loop block diagram of the system is given in Fig. 56. In this system, the generator torque, T_g, is the input to the system, and the translator force is its output while the wave excitation force acts as the disturbance. Notice that eventually the translator force is supposed to track a reference value, $F_{t,ref}$ (not shown), that is determined based on the control strategy and the wave excitation force amplitude and frequency. To that end, the control loop may be closed on F_t. The error will then be passed through a controller whose output is the reference of the generator torque (control effort) required to create the desired translator force. The internal dynamics of the rotary generator and power electronics converter are not considered in this study, as they are much faster than the variations of the ocean waves.

The open loop transfer functions from the input, T_g, to the translator force, F_t, translator speed, V, and rotor speed, Ω, are given in (50) to (52):

$$\frac{F_t}{T_g} = -GT_m \frac{MS^2 + BS + K}{D(S)} \tag{50}$$

$$\frac{\mathrm{V}}{T_g} = -\frac{GT_m S}{D(S)} \tag{51}$$

$$\frac{\Omega}{T_g} = \frac{S(MS^2 + BS + K + G^2 T_m)}{D(S)} \tag{52}$$

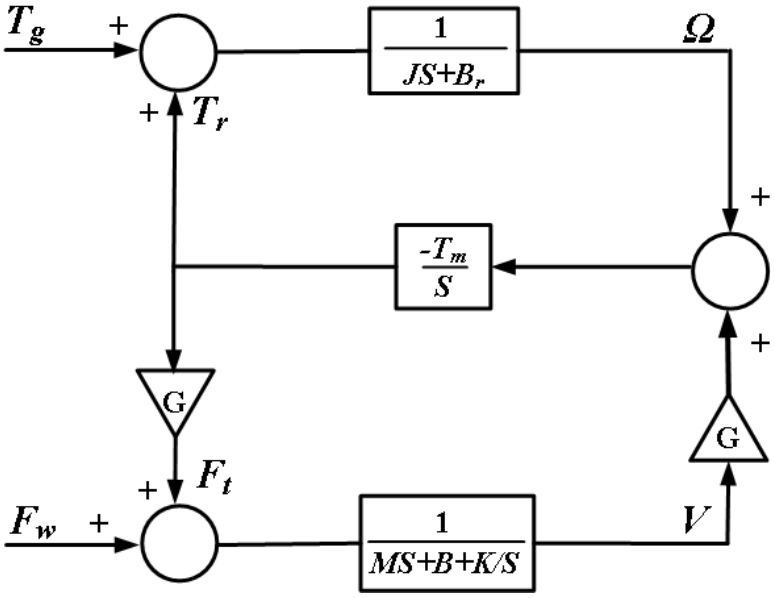

Fig. 56. Block diagram of the energy conversion system consisting of a buoy and a MITROMAG.

Given in (53) to (55) are the open loop transfer functions from the disturbance, F_w, to the translator force, translator speed, and rotor speed:

$$\frac{F_t}{F_w} = -G^2 T_m \frac{S(JS + B_r)}{D(S)} \tag{53}$$

$$\frac{\mathrm{V}}{F_w} = \frac{S(JS^2 + B_r S + T_m)}{D(S)} \tag{54}$$

$$\frac{\Omega}{F_w} = -\frac{GT_m S}{D(S)} \tag{55}$$

The open loop system characteristic equation, D(S) is:

$$D(S) = JM\left\{S^4 + \left(\frac{B}{M} + \frac{B_r}{J}\right)S^3 + \left(\left(\frac{G^2}{M} + \frac{1}{J}\right)T_m + \frac{K}{M} + \frac{B_r B}{JM}\right)S^2 + \left(\frac{(B + G^2 B_r)T_m + B_r K}{JM}\right)S + \frac{KT_m}{JM}\right\} \quad (56)$$

Two components contribute to the translator force: one comes from the wave force and the other from the generator torque. Let F_{tw} signify the former component, that is, the translator force in the absence of generator torque. Then from (53):

$$F_{tw} = \left(\frac{F_t}{F_w}\right)F_w = -G^2 T_m \frac{S(JS + B_r)}{D(S)}F_w \quad (57)$$

From (50), the component of the translator force due to the generator torque, F_{tg}, is given by:

$$F_{tg} = \left(\frac{F_t}{T_g}\right)T_g = -GT_m \frac{MS^2 + BS + K}{D(S)}T_g \quad (58)$$

To achieve a reference translator force, the part of the translator force that is created by the wave force can be subtracted from the reference value; the result is the force that must be created by the generator torque. Therefore, the required translator force to be created by the generator torque, $F_{tg,ref}$, yields to:

$$F_{tg,ref} = F_{t,ref} - F_{tw} \quad (59)$$

The required generator torque, $T_{g,ref}$, which is the torque that is required for creating the required translator force, $F_{tg,ref}$, can be obtained from:

$$T_{g,ref} = \frac{F_{tg,ref}}{\left(\frac{F_t}{T_g}\right)} = \frac{F_{t,ref} - F_{tw}}{-GT_m \frac{MS^2 + BS + K}{D(S)}} \quad (60)$$

The dynamics of the rotary machine and the power converter associated with it are neglected, and it is assumed that once the required generator torque is set by the controller, it is immediately produced by the machine.

4.4.2. Open loop system characteristics

Before proceeding, a MITROMAG is designed for the buoy under study. Since the rated force is 50 kN, the TROMAG is designed for the pull-out force of 62.5 kN to provide a 25% safety margin and avoid "slipping" due to overload percentages up to 25%. Therefore, the TROMAG will mainly operate within the range for which linearization of the motion equations results in negligible error. The inner part of the TROMAG is set to be the rotor and the outer part to be the translator. Aspects of magnetic design of the TROMAG were detailed in Chapter 3.

Here, the TROMAG is designed for the gear ratio of G=100π m^{-1} (corresponding to the translator pole pitch of 10 mm); therefore, the rotor pull-out torque is T_m=199 N.m. With magnet residual flux density of 1.2 T, air gap length of 2 mm, the magnet thickness and coverage are set at 5 mm and 80%, respectively. The resultant shear stress is 190 kN/m^2. The rotor outer radius is set at 75 mm, so the active length works out to about 0.7 m. To allow for the complete engagement between the rotor and translator as the latter one reciprocates, the stroke length must be added to either of them. In this design, the stroke length is added to the active length of the translator, so the rotor length is 0.7 and the translator length is 1.7 m. The translator mass is thus 105 kg, which is added to the buoy mass; hence M works out to 11597 kg.

A PM machine is also designed for the rated torque of (50 kN)/(100π m^{-1}). The overall moment of inertia of the two rotors is about 0.2 N.m.s^2. The value of J would change when different values are considered for the radius and length of the rotor of the TROMAG or when alternative designs are considered for the rotary machine. Therefore, this parameter will be swept over a range to study its effects on the system characteristics. It will be shown that the moment of inertia has a profound impact on the open loop system gains.

The open loop system characteristic equation given in (56) can be written in the following form:

$$D(S) = JM[(S+\alpha_1)^2 + \beta_1^2][(S+\alpha_2)^2 + \beta_2^2] \tag{61}$$

where $-\alpha_1 \pm j\beta_1$ and $-\alpha_2 \pm j\beta_2$ are the open loop poles. By assuming that B_r is negligible, and using the values given above (M=11597 kg, B=5000 N.s/m, K=96743 N/m, J=0.2 N.m.s^2, T_m=199 N.m, and G=100 π.m^{-1}, that are referred to as the rated values) the open loop poles are $P_1 = -\alpha_1 \pm j\beta_1$=-0.14±j51.9 and $P_2 = -\alpha_2 \pm j\beta_2$=-0.08±j1.75. All poles, although stable, have small real parts.

The Bode plots of the transfer functions from the generator torque to the translator force, F_t/T_g, and from the wave excitation force to the translator force, F_t/F_w, are of special interest as they determine how much generator torque is needed to create a given translator force when the disturbance exists. The range of 0.3 to 2 rad/s may be considered as reasonable for the ocean wave frequency spectrum; however, in Fig. 57 the Bode plot is shown for a wide range of frequencies, from 0.1 to 100 rad/s.

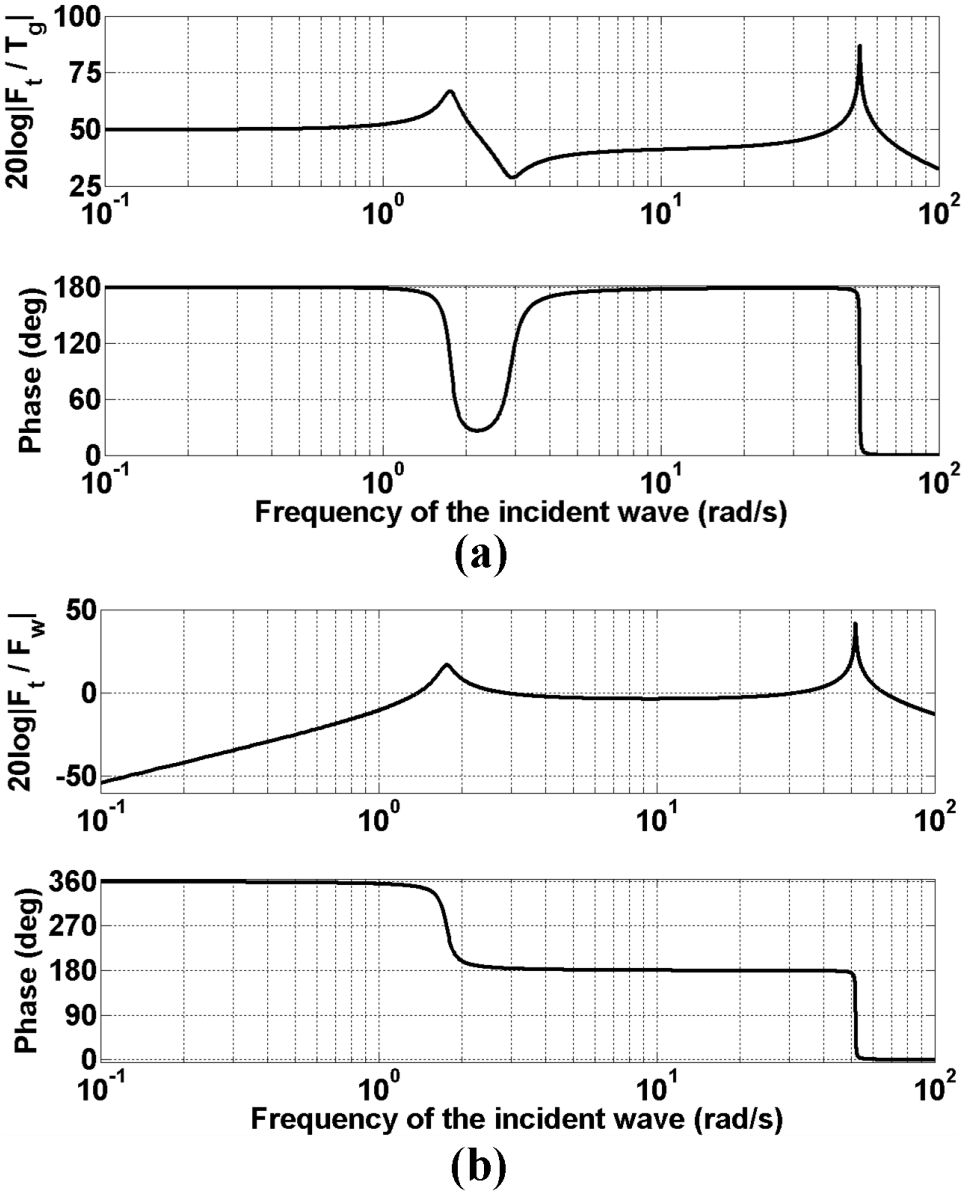

Fig. 57. Bode plots of the open loop transfer functions. (a) generator torque to translator force. (b) wave force to translator force.

In the Bode plot of F_t/T_g, it is observed that for the wave frequencies up to about 0.5 rad/s, the open loop gain remains almost constant at the rated value (the gear ratio for which the TROMG is designed, G=100π). Beyond that point, the system gain starts to

increase and reaches its maximum at $\omega=\beta_2$=1.75 rad/s, which is the low frequency open loop pole. Then it starts to decline and eventually falls below the rated gear ratio at about ω=2.1 rad/s. The system gain from generator torque to translator force may be called the "effective gear ratio," G_e. Notably, depending on the system parameters, over a certain frequency range (in this case, from 0.5 to 2.1 rad/s) the system can exhibit an effective gear ratio that is significantly higher than the TROMAG rated gear ratio.

For example, at the incident wave frequency of ω=1.5 rad/s, the effective gear ratio is 2.6 times the rated value. A large effective gear ratio could imply less torque demand on the rotary machine and reduce its size and cost. On the other hand, the effective gear ratio falls below the rated value at ω=2.1 rad/s. So for wave frequencies larger than this value, the generator torque may need to be rated at values larger than 1/G times the translator rated force.

In the Bode plot of F_t/F_w, it is observed that for frequencies up to about 1.38 rad/s the translator force due to an incident wave has an amplitude smaller than that of the incident wave, and is in phase with it. At $\omega= \beta_2$=1.75 rad/s, the open loop gain of F_t/F_w maximizes, but the phase of F_{tw} is 90 degrees behind the phase of F_w at this frequency.

The influence of several MITROMAG parameters on the effective gear ratio is illustrated in Fig. 58. It is observed that increase of the rotor damping coefficient reduces the maximum achievable effective gear ratio; however, it has a small effect on the frequency at which the resonance occurs and on the effective gear ratio at other frequencies. A poorly manufactured TROMAG with large friction can exhibit an

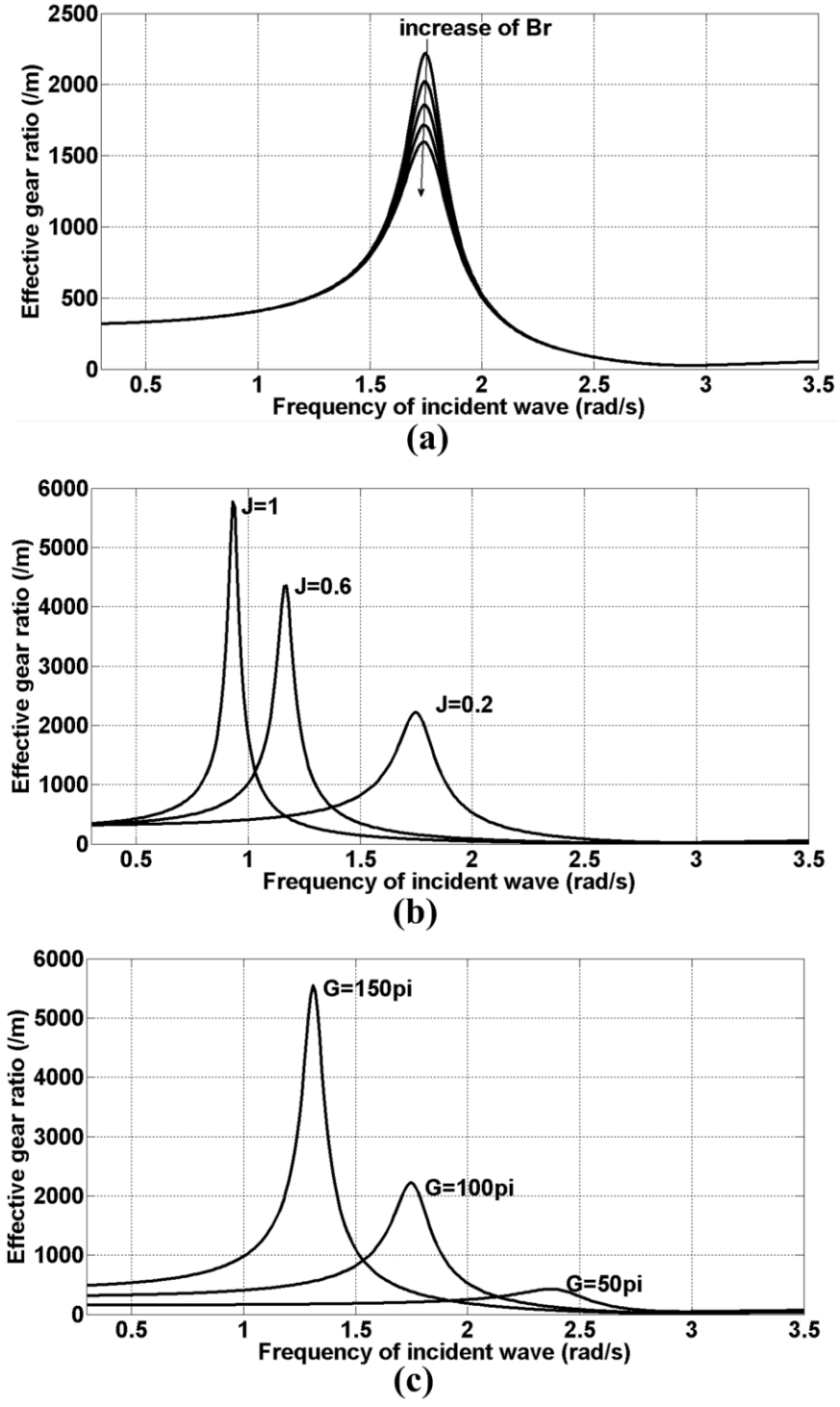

Fig. 58. Variations of the effective gear ratio with several parameters. (a) increase of B_r from 0 to 0.02 at steps of 0.005. (b) increase of J from 0.2 to 1. (c) increase of G from 50π to 150π.

effective gear ratio below the rated value over a wide range of frequencies. The impact of increasing moment of inertia and the rated gear ratio are similar in that they both not only increase the effective gear ratio at the resonance frequency, but also push the resonance frequency down to the common range of the ocean wave frequencies.

4.4.3. Force and power

As an example of variations of force and power with time, the reactive control method is assumed, and (50) to (60) are used to obtain $F_{t,ref}$, F_{tw}, F_{tg}, $T_{g,req}$, the peak power of the translator, $P_{t,peak}$, and the peak power of the generator, $P_{g,peak}$, versus the incident wave frequency. The translator peak power indicates the demand of peak power on a DDLG, should it be used rather than a MITROMAG. In this control strategy, the average power is independent of the frequency as the buoy and its PTO resonate irrespective of the incident wave frequency. The results are shown in Fig. 59 for the rated conditions and the wave excitation force amplitude of F_w=1 N. The given values of force and torque scale linearly with the wave force amplitude, while the power values scale with the square of the wave force amplitude. It is noticed that, while the reference translator force holds its minimum value at the buoy natural frequency (ω=2.9 rad/s), the required generator torque to achieve the reference value holds its minimum at the system resonance frequency of ω=1.75 rad/s. Also, it can be seen that the generator used along with the TROMAG requires less peak power than a corresponding DDLG for wave frequencies less than 2.1 rad/s.

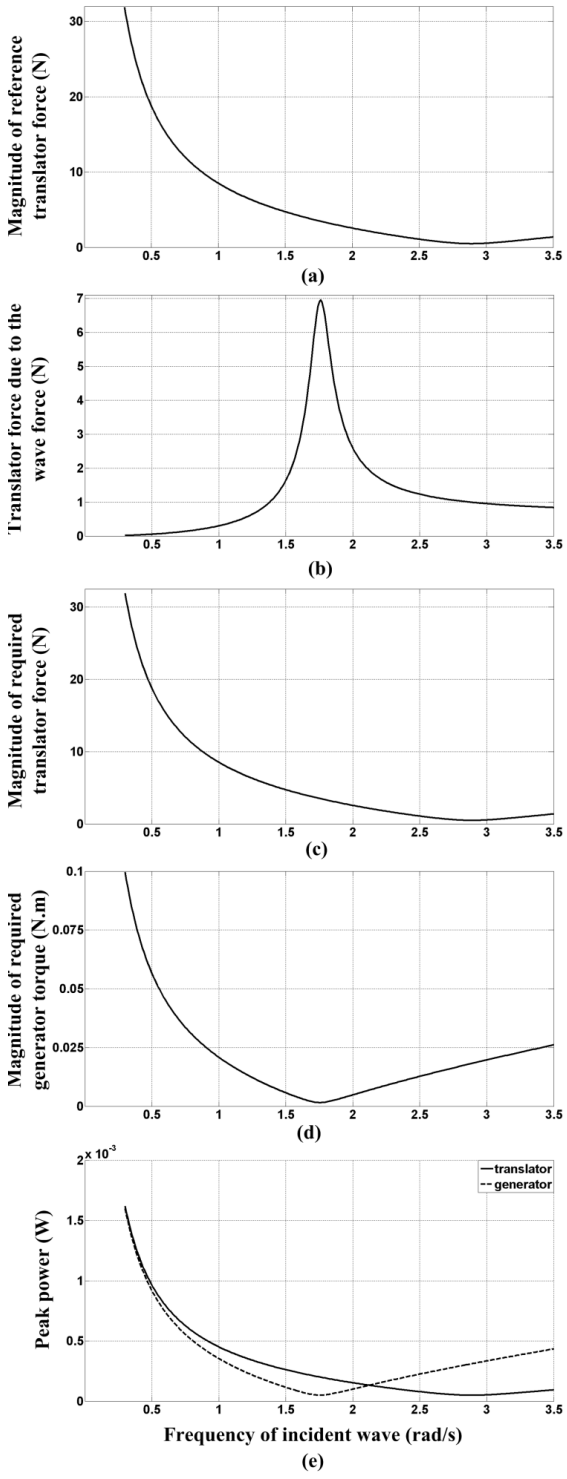

Fig. 59. Variations of the system quantities with wave frequency under the reactive control strategy. (a) reference translator force. (b) translator force due to the incident wave. (c) translator force to be created through the generator. (d) required generator torque.

The entire system is simulated in MATLAB SIMULINK™, and the quantities mentioned above are obtained in the time domain for an incident wave with amplitude and frequency of 10 kN and 1.5 rad/s. The nonlinear representation of the TROMAG is used for time domain simulations. Fig. 60, Fig. 61, and Fig. 62 present the waveforms. As seen in Fig. 60, the reference translator force for realizing the reactive control is almost 4.7 times the incident wave in amplitude and 96° behind it in phase. The translator force due to the wave excitation force (obtained by setting the generator torque to zero) has the amplitude of 16 kN, and lags the wave force by 16 degrees. While the reference translator force is about 47 kN, the required generator torque to create this reference force is about 58 N.m. Notice that with the rated gear ratio of 100π, the rotor torque corresponding to 47 kN translator force yields to (47 kN)/(100π /s) = 150 N.m. Moreover, the translator force clearly contains a component with frequency of β_1=51.9 rad/s. Fig. 60(c) and Fig. 60(f) show F_{tw} and F_t during the first 10 s. Comparing the last two figures indicates that the high frequency term mainly arises from the interaction of the TROMAG with the generator. This component damps down after a few cycles.

In addition, as shown in Fig. 61, the translator speed is in phase with the wave excitation force, indicating that the reactive control method has been successfully applied and the power absorbed from the incident wave is maximized. The translator speed amplitude, 1 m/s, matches the values obtained from (46) with F_w=10 kN and B=5000 N.s/m. The rotor speed, as expected from a TROMAG with right-handed helix, is 180° phase shifted with respect to the translator speed.

The instantaneous power associated with the incident wave, P_w, the translator, P_t, the rotor of the TROMAG, P_r, and the rotary generator, P_g, are shown in Fig. 62. The incident wave has a peak value of 10 kW and average value of 5 kW. The average power absorbed by the translator is half the incident wave average power, as expected in the reactive control strategy. Since no losses are considered for the TROMAG, the average power of the rotor of the TROMAG and the generator are the same as that of the translator. The peak power of the rotary generator, however, is almost one-half of that of the translator, as can be deduced from Fig. 59(e) as well.

The moment of inertia of the rotor of the MITROMAG has a noticeable influence on F_{tw}, $T_{g,ref}$, and $P_{g,peak}$. Variations of the above-mentioned quantities with J are depicted in Fig. 63. These observations indicate that, when designing a MITROMAG and power converter for a buoy, the dynamic interactions between the two systems, as well as the wave frequency spectrum must be taken into account.

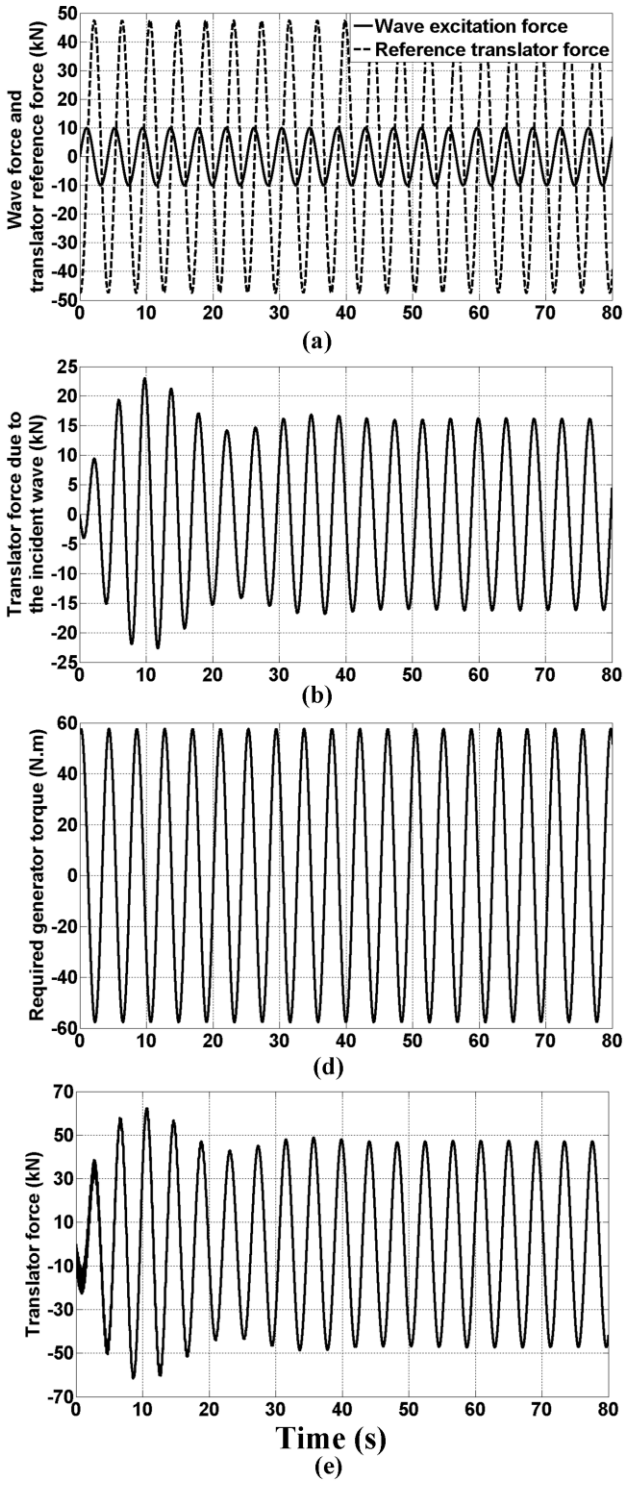

Fig. 60. Waveforms under reactive control strategy. (a) wave excitation force and the corresponding reference translator force. (b) translator force due to the wave force. (c) zoomed-in view of (b). (d) required generator torque. (e) translator force, and (f) zoomed-in view of (e).

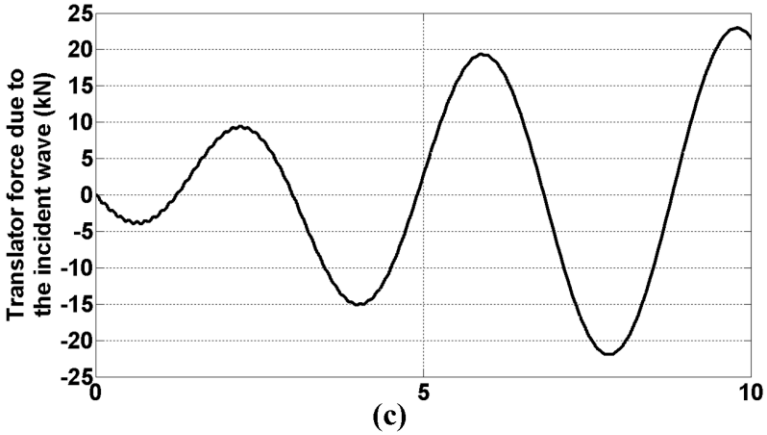

(c)

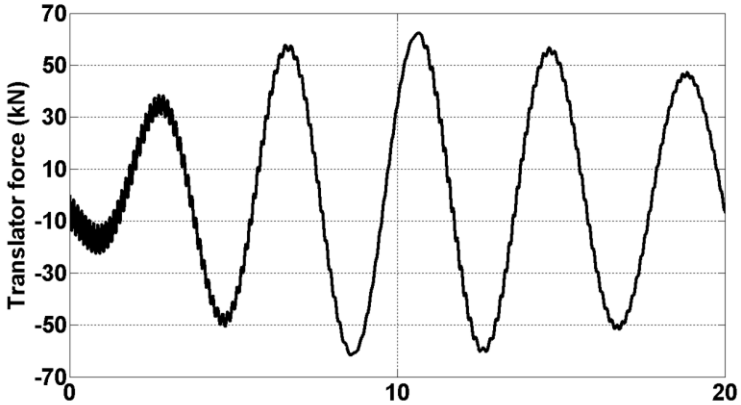

(f)

Fig. 60. Continued.

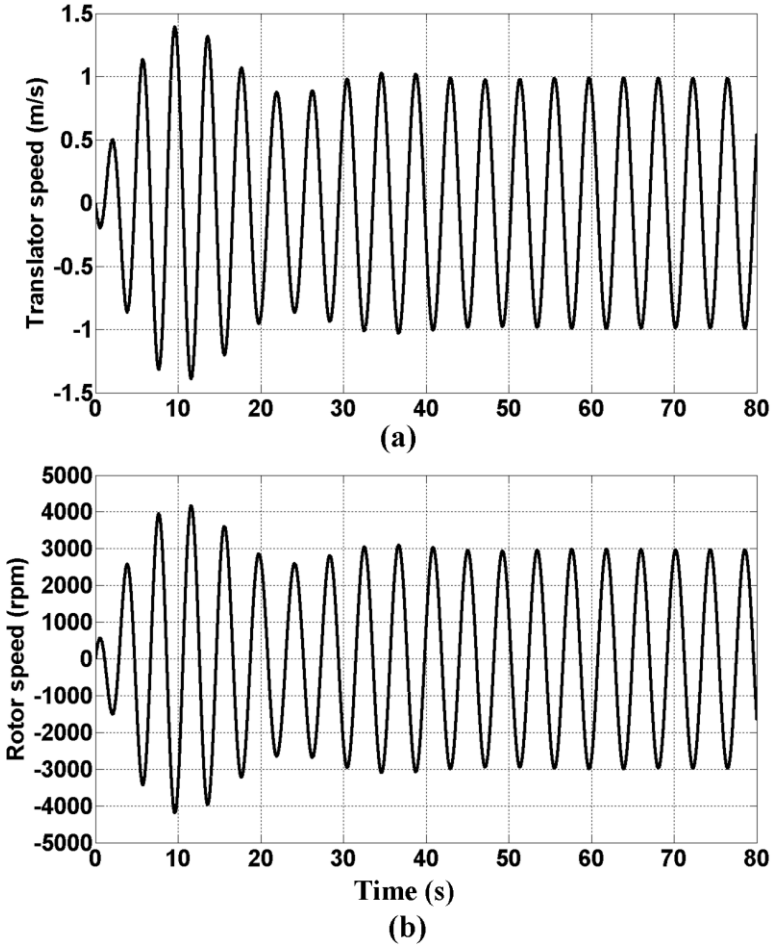

Fig. 61. TROMAG speed under reactive control strategy. (a) translator. (b) rotor.

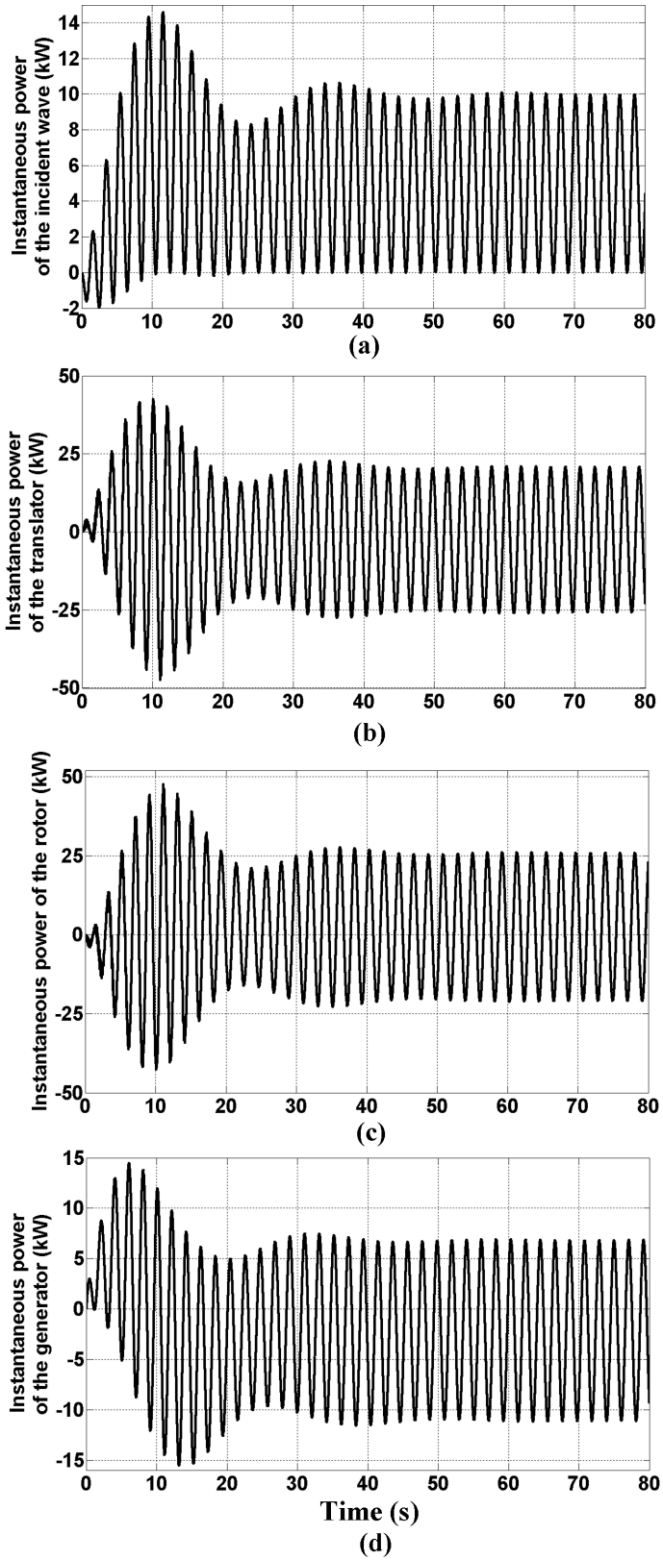

Fig. 62. Instantaneous power. (a) wave. (b) translator. (c) rotor. (d) generator.

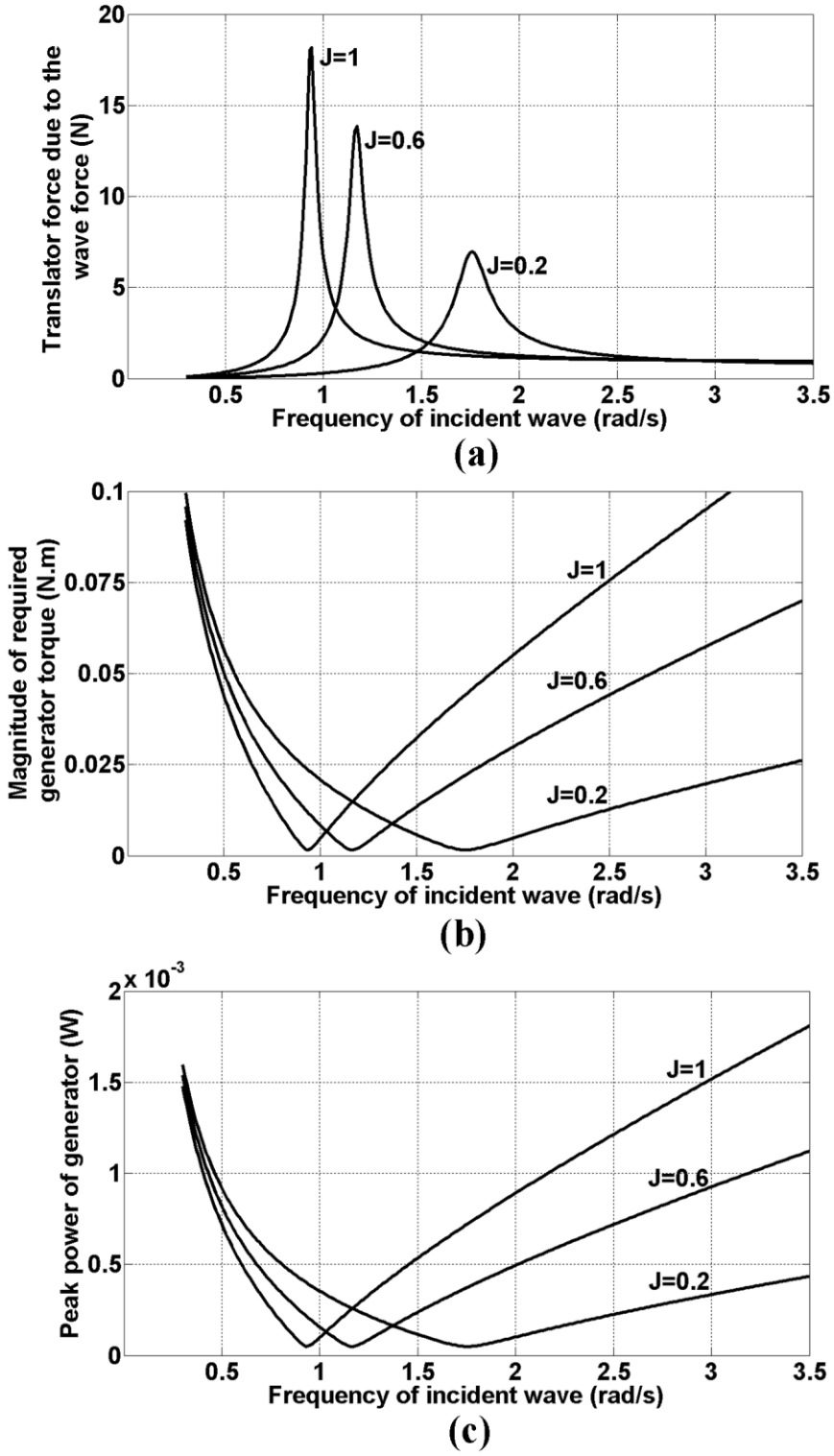

Fig. 63. Influence of rotor moment of inertia. (a) F_{tw}. (b) $T_{g,ref}$. (c) generator peak power.

4.5. Summary

A nonlinear analytical model was proposed for the TROMAG in this chapter. The model describes the TROMAG as a system of springs with nonlinear stiffness. As verification, the model was used to obtain the rotor position during an oscillation test, and the results were compared with those of the 3D FEA. The model was then linearized about a stable equilibrium point, and the error due to the linearization was studied. The closer the operating point gets to the pull-out values, the larger the error will be.

A linear model describing the interaction between a buoy and an incident wave was presented, as well as the main control strategies for buoys. Thereafter, the model was combined with the linearized model of the TROMAG to yield a 4^{th} order system, and the system open loop transfer functions were then derived. It was revealed that the translator force to rotor torque ratio is a function of the incident wave frequency. This frequency-dependent quantity was defined as the effective gear ratio; and its variations with the wave frequency as well as other system parameters, such as the rated gear ratio, the rotor moment of inertia, and the rotor damping coefficient were studied.

Afterward, the reactive control strategy was considered as an example, and the reference force determined based on this strategy was used to further study the system behavior. It was shown that, depending on the wave frequency, the required peak power capability of the rotary generator that is employed along with the TROMAG can be noticeably smaller than a DDLG used in a similar system.

5. FABRICATION OF A TROMAG

5.1. Introduction

This chapter reports on the fabrication of a TROMAG prototype, and the results of the experiments performed on the set-up. A static test was performed to obtain the force characteristic. Moreover, oscillation tests on the rotor and translator were conducted, and the results are reported.

5.2. Prototype

The set-up assembly was first designed in SolidWorks® as illustrated in Fig. 64. The prototyped TROMAG is decided to have a long inner part as the rotor and a short outer part as the translator. The rotor, a hollow cylinder, is equipped with an end-cap and a shaft at each end. Each end shaft of the rotor is supported by a rotary ball bearing. To drive the rotor, it is coupled, through flexible couplings and a torque transducer, to a rotary machine. The translator, similar to the rotor, is a hollow cylinder, and it is press-fit into a rectangle-cubical flange. Linear ball bearings are attached to the bottom of the translator flange at both sides, so the translator can slide on the two rails. In order for the translator to be coupled to a load, its flange is connected to another flange, called the end-flange, through two connecting rods. The end-flange is also mounted on the rails through two linear ball bearings. The force transducer is attached to the end-flange.

Both the rotor and translator cores are made of 1020 steel material. To ease the fabrication, flexible strips of magnets, made of a mixture of Nd-Fe-B and some elastic materials are employed. The remanent flux density of the employed magnet material is

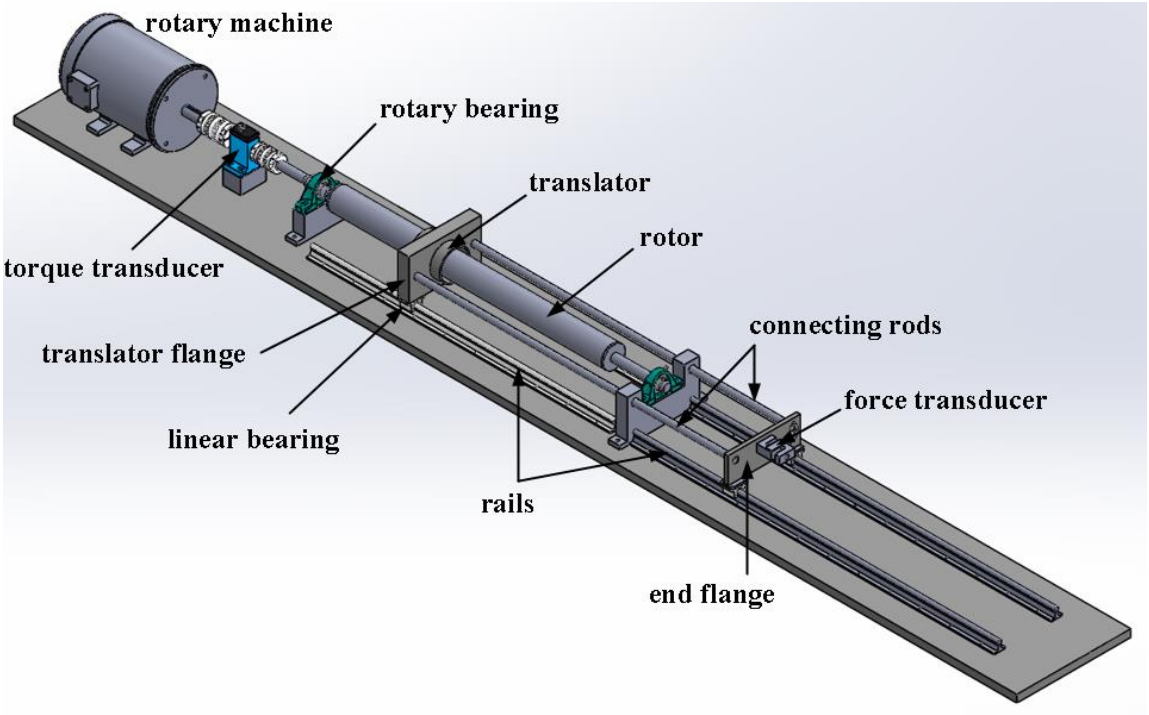

Fig. 64. Set-up assembly in SolidWorks®.

roughly 0.45 T, and its mass density is 5234 kg/m^3. Moreover, they are not electrically conductive; hence, no eddy current losses are expected in the magnets. Shallow, double start threads are grooved on both the rotor and translator cores to facilitate placing and pasting the magnet strips. Fig. 65(a) and Fig. 65(b) show the rotor and the translator before magnet strips were pasted on them. Fig. 65(c) shows the translator with its pasted magnets, press-fit in the flange.

The translator flange and the end-flange, as well as the connecting rods, are made of aluminum; whereas, the rotor end-caps and shafts are made of stainless steel. Four springs, two on each connecting rod, are provided to prevent the translator from hitting

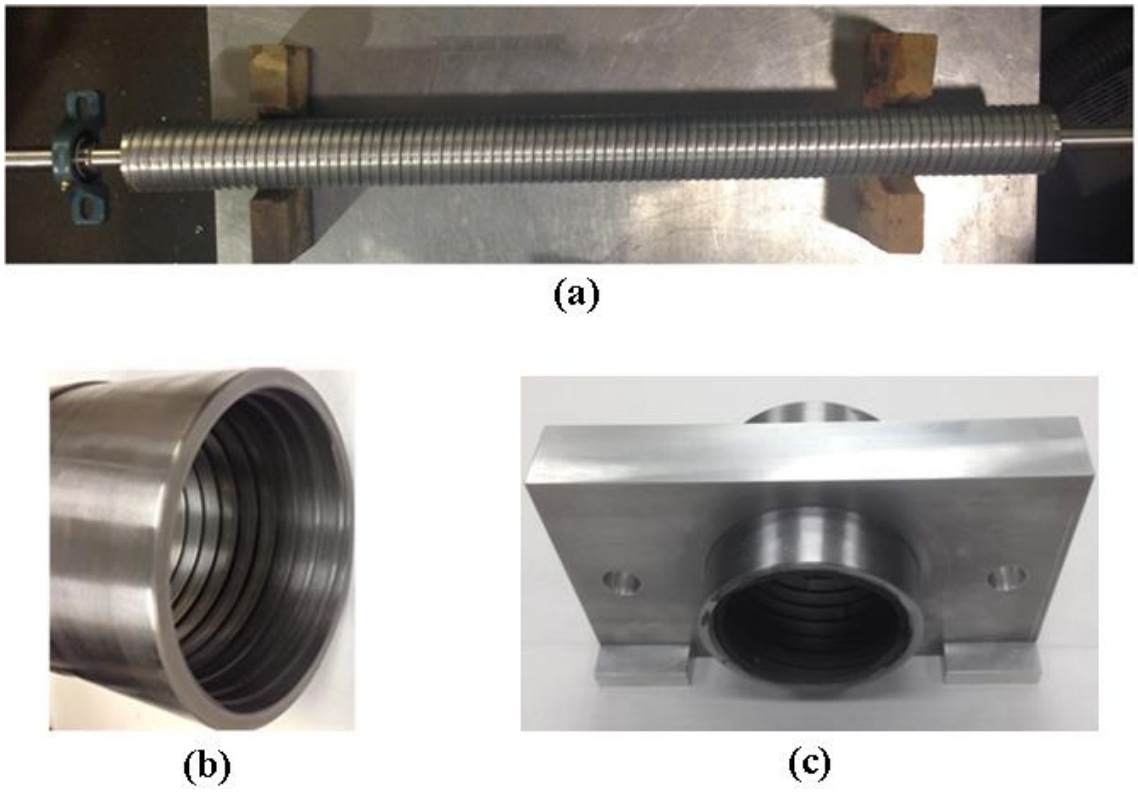

Fig. 65. Rotor and translator cores. (a) rotor. (b) translator core. (c) translator core (with magnets pasted on the inner surface), press-fit into the flange.

the rotary bearing stands, in case the control system fails to stop the translator at the desired position. Fig. 66 shows a picture of the setup assembly in which the rotor is partially covered by magnet strips. A shaft encoder is provided for measuring the rotor position, while a linear magnetic encoder is attached to the translator flange for measuring the translator position. The magnetic tape, required for the operation of the linear encoder, is pasted on the test bed, in parallel with the rails. Principal dimensions of the fabricated TROMAG are given in Table 6. The long lathe employed for making the rotor was equipped with Imperial units only; that is why some dimensions are given in the SI system and the others in the Imperial system of units. Notice that the pole pitch

is 0.4 inches which, from (2), yields a gear ratio of $G=2\pi/(2\times0.4\times0.0254)=309.2$ m^{-1}. The calculated moment of inertia of the rotor of the TROMAG is about 0.012421 N.m.s^2. The measured mass of the translating bodies, (including the translator and its magnets, the two flanges, the connecting rods, and the linear bearings) is 7.8 kg.

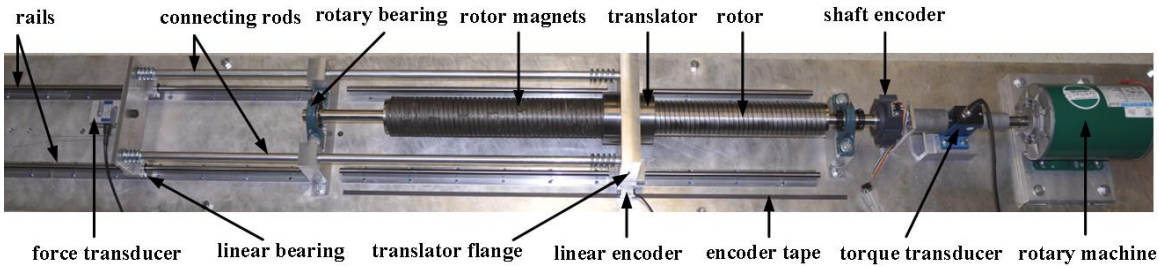

Fig. 66. Set-up assembly.

Table 6. Principal dimensions of the prototyped TROMAG shown in Fig. 66

Quantity	**Value**
Magnet thickness on translator and rotor (mm)	5
Magnet width (mm)	8
Pole pitch (inch)	0.4
Outer radius of rotor core at groove peaks (inch)	1.439
Inner radius of translator core at groove peaks (inch)	1.813
Groove depth on the rotor (inch)	0.051
Groove depth on the translator (inch)	0.048
Air gap length (mm)	2
Translator length (inch)	4
Rotor length (inch)	36

5.3. Experimental results

5.3.1. Static force measurement

To obtain the force characteristic, the rotor is rotated manually by 90 degrees, while the translator is prevented from motion through an angle-shaped aluminum hurdle (not shown in Fig. 66) against which the force transducer is pressed. The rotor position is measured by the shaft encoder whose output is fed to the eQEP™ module of a Texas Instruments Piccolo™ DSP. The measured force, whose peak value is 670 N, is presented in Fig. 67. With 0.45 T as the remanent flux density, the pull-out force of 675 N is obtained from a 3D FEA model with discretized helix, 700 N from 2D FEA, and 717 N from the 2D analytical model. A close agreement is observed between the experiment and analysis.

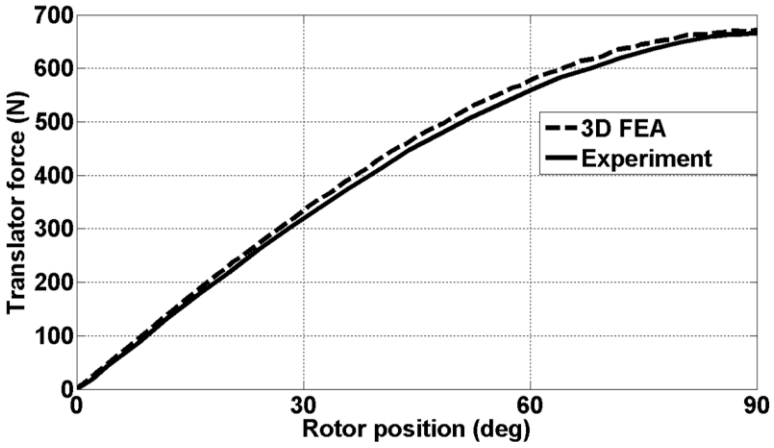

Fig. 67. Force characteristic of the prototyped TROMAG.

5.3.2. Oscillation test

5.3.2.1. Rotor oscillation test

To perform the rotor oscillation test, the translator is bolted to the hurdle mentioned in Section 5.3.1. The rotor is pulled to θ=90°, and then it is released to oscillate. The shaft encoder output is demonstrated in Fig. 68(a). Due to the large static friction, the waveform is initially flat. Moreover, as the oscillations damp down and the rotor approaches the equilibrium point, it suddenly stops at a final position, rather than decaying gradually.

To be able to compare the experimental results with the analytical model, the rotor damping coefficient, B_r, must be known. To estimate B_r, the linearized analytical model given in (31) is employed. The settling time of an under-damped second order system, t_s, is roughly 4 times the system time constant. The time constant equals the inverse of the absolute value of the real part of the system poles. Therefore, from (32):

$$t_s \cong \frac{4}{\alpha_r} = \frac{4}{B_r/(2J)} \Rightarrow B_r \cong \frac{8J}{t_s} \tag{62}$$

From Fig. 68(a), the settling time is about 3.5 s. Thus, B_r works out to about 0.0284 N.m.s. The resultant damping coefficient looks too large to be only due to the friction in the bearings. The reason for such a large B_r was found to be rooted in the translator motions: a close observation revealed that the translator had not been perfectly locked, and it was moving during the test. It is speculated that the motion of the translator dissipated a noticeable part of the rotor potential energy in the locking mechanism.

The rotor position during the rotor oscillation test, obtained from the nonlinear analytical model presented in (30) using the values of 0.0284 and 0.012421 for B_r and J, is shown in Fig. 68(b). A reasonable agreement is observed between the experiment and the analysis. The small discrepancies can be attributed to factors such as the static friction not being accounted for in the analytical model, speed-dependent friction of the prototype, and inaccuracy in the calculated value of the rotor moment of inertia.

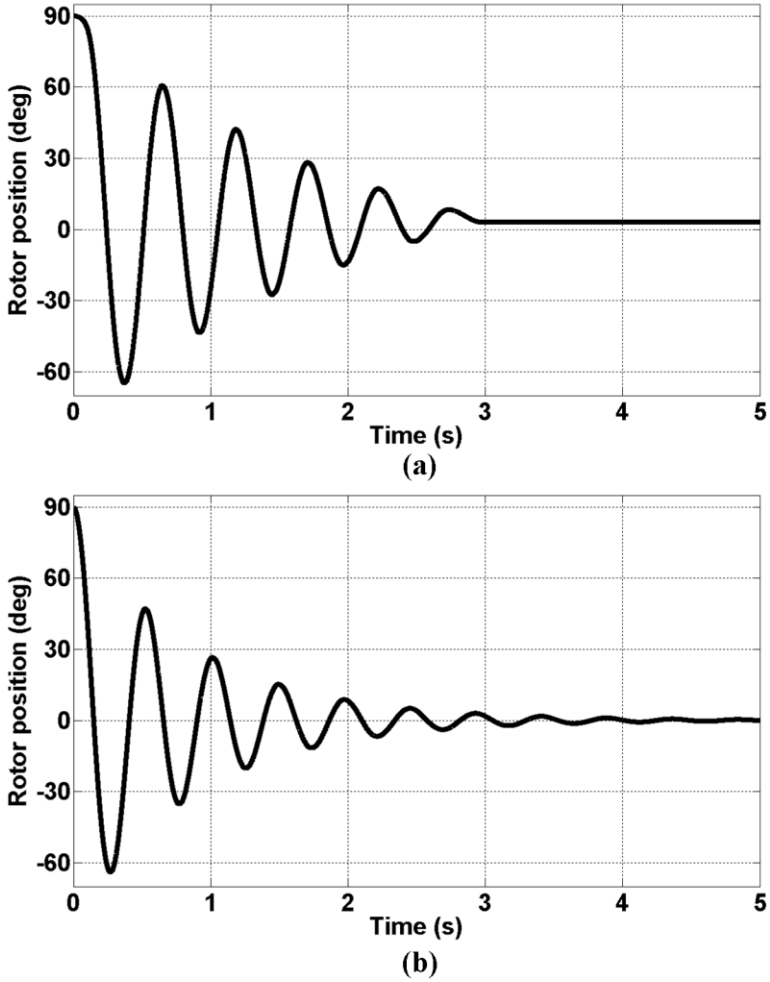

Fig. 68. Rotor position during a rotor oscillation test. (a) measured. (b) calculated by the nonlinear analytical model.

5.3.2.2. Translator oscillation test

The translator oscillation test is experimentally run as follows: the rotor is rotated manually until the translator reaches the hurdle. The rotor and translator positions when the translator is flush with the hurdle are assumed to be $\theta=0^{\circ}$ and $z=0$ mm. Further rotation of the rotor from $\theta=0^{\circ}$ in clockwise (positive θ) direction pushes the translator in the –Z direction against the hurdle, until the rotor reaches (ideally) $\theta=180^{\circ}$, which is an unstable equilibrium point. Meanwhile, since the translator is fixed, z remains constant at zero, and hence $\theta+Gz$ increases from 0 to π. Given the characteristics of Fig. 51, when $\theta+Gz$ is between 0 and π, the rotor torque and translator force are both negative. Once $\theta+Gz$ crosses π, T_r and F_t become positive. The rotor is held in hand tightly to prevent it from rotation; however, the translator which is now experiencing a positive force is free to move in +Z direction. At this point, motion of the translator in +Z direction while θ is fixed increases F_t according to Fig. 51. Increase of F_t, in its own right, further pushes the translator in +Z direction and further moves the translator away from the unstable equilibrium point. The translator eventually reaches $z=10$ mm ($\theta+Gz=2\pi$), which is a stable equilibrium point. Due to its inertia, however, the translator crosses this point and oscillates about it before settling down.

Fig. 69(a) shows the translator position during the test outlined above, measured by the linear encoder. Similar to the case of rotor oscillation test, the measured settling time and the linearized model can be used to approximate the damping coefficient associated with the translator, B_t. By assuming that the measured settling time is almost 4 times the linearized system time constant, from (37), B_t is obtained as follows:

$$B_t \cong \frac{8M}{t_s} \tag{63}$$

In Fig. 69(a), the settling time is about 0.7 s. The translator damping coefficient, B_t, thus works out to 89.1 N.s/m. With this value, the test is simulated in SIMULINK™, and the result is depicted in Fig. 69(b). As seen, the experimental results verify the analytical model.

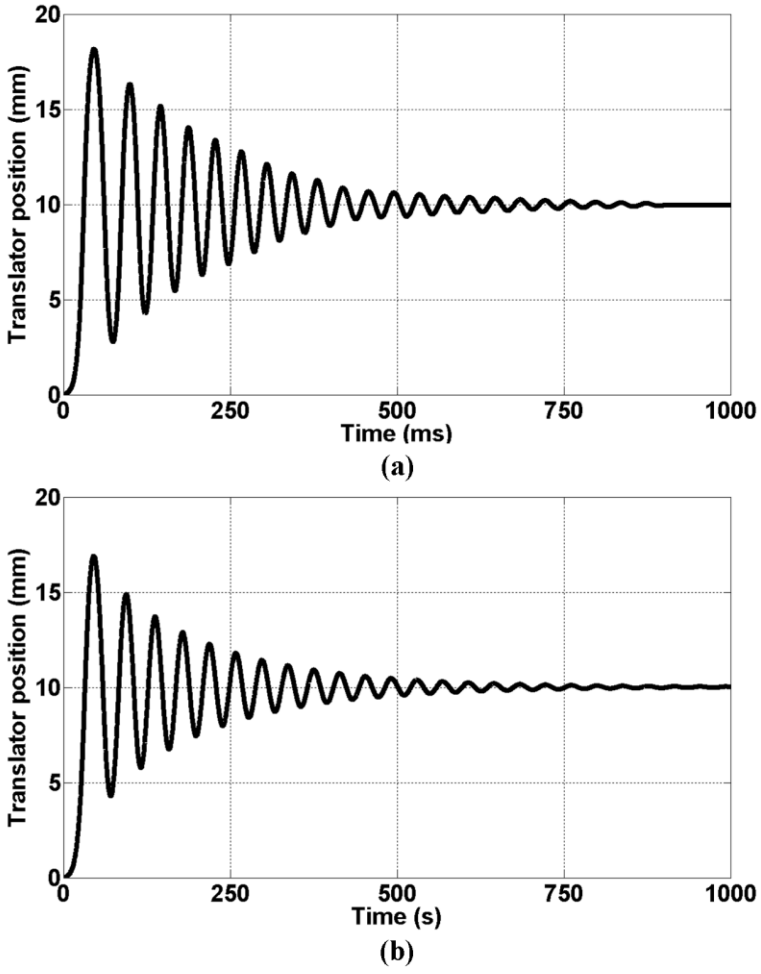

Fig. 69. Translator position during a translator oscillation test. (a) measured. (b) calculated by the nonlinear analytical model.

5.4. Summary

A TROMAG was prototyped with a short outer part as the translator and a long inner part as the rotor. The force characteristic of the prototype was obtained by rotating the rotor while the translator was locked through a force transducer. Moreover, the oscillation tests were performed on both the rotor and translator. The close agreement between the experimental and theoretical results verified the concept of the TROMAG, as well the analyses performed throughout the dissertation.

6. CONCLUSIONS AND FUTURE WORK

In this dissertation, the TROMAG was introduced as a reliable, efficient, and cost-effective magnetic device to tackle the problem of low-speed, high-force motion characteristic of buoys. In addition to presenting the structure and principles of operation, it was shown how the device can be considered as two arrays of skewed, alternating polarity magnets, so better insight into device operation can be gained.

Aspects of the magnetic design were investigated: variations of the shear stress with pole pitch, magnet dimensions, and air gap length, as well as the effects of helix non-ideality and the possibility of demagnetization. It was shown that, for a given magnet thickness and air gap length, there is an optimum pole pitch for which the shear stress is maximized. Similarly, for a given pole pitch, magnet thickness, and air gap length, there is an optimum magnet coverage for which the pull-out force per volume of magnet material is maximized. Also revealed was that deviation from an ideal helix path would corrupt the force and torque characteristics, both their waveforms and pull-out values. Another concluded hint for the design was to use magnets of the same thickness and material grade for both the rotor and translator. Moreover, a MITROMAG was compared with a DDLM for several values of force to show that the system proposed in this dissertation far surpasses a traditional DDLM in terms of weight, volume, and cost of the active material. The MITROMAG can be an order of magnitude lighter and more compact than a DDLM, while costing less than one-half that of the DDLM.

Furthermore, a nonlinear analytical model was proposed for describing the TROMAG dynamics. The model was then linearized. Both the nonlinear and linearized models were used to predict the rotor position during an oscillation test, and the results were compared with 3D FEA to show the effectiveness of the analytical model. The linearized model was used along with the linearized model of a buoy to develop a Laplace domain representation for the dynamics of the entire system. The open loop system characteristics were studied and it was shown that, when used along with a generator to drive a buoy, the TROMAG would exhibit a frequency-dependent gear ratio which is different from the rated gear ratio for which it is designed. The effects of several system parameters, such as rotor moment of inertia, rated gear ratio, and rotor damping coefficient on the effective gear ratio, were studied. It was also shown that the rotary generator used with a TROMAG can have a noticeably smaller peak power requirement compared to a DDLM designed for the same system. Given these findings, it is clear that designing a MITROMAG for a buoy entails the study of the dynamic interaction between the two, while accounting for the ocean wave characteristics.

Eventually, a prototype was fabricated and the static force test, as well as the rotor and translator oscillation tests, was performed on it. Test results verified the results obtained from the analysis.

MITROMAG is a novel machine, and with a novel machine come numerous research opportunities. A few potential paths of research are suggested here:

- The embedded magnet design configuration for the TROMAG can be studied in terms of the magnetic design, as well as the opportunities and challenges that it offers for manufacturing.
- Aspects of mechanical design of the TROMAG, such as vibrations, mechanical losses, and structural design should be studied. Effective bearing layouts have to be devised, accounting for the environment in which the TROMAG is to be employed.
- In this dissertation, the ocean wave was assumed to be monochromatic. Although this is a viable assumption for establishing the research fundamentals, the behavior of the MITROMAG, when exposed to a spectrum of waves should be investigated.

REFERENCES

[1] B. Drew, A. Plummer, and M. N. Sahinkaya, "A review of wave energy converter technology," in *Proc. 2009 Inst. Mech. Eng., Part A-J Power Energy,* vol. 223, pp. 887-902.

[2] A. M. Cornett, "A global wave energy resource assessment," in *Proc. 2008 Int. offshore and polar Eng. Conf.,* pp. 318-326.

[3] T. Brekken, "Fundamentals of ocean wave energy conversion, modeling, and control," in *Proc. 2010 IEEE Int. Symp. Industrial Electron. (ISIE),* pp. 3921-3966.

[4] R. Pelc and R. M. Fujita, "Renewable energy from the ocean," *Marine Policy,* vol. 26, pp. 471-479, 2002.

[5] M. E. McCormick, *Ocean wave energy conversion*, Dover Publications, Mineola, New York, 2007.

[6] D. Bull, M. E. Ochs, D. L. Laird, B. Boren, and R. A. Jepsen, "Technological cost-reduction pathways for point absorber wave energy converters in the marine hydrokinetic environment," Sandia National Laboratories, Albuquerque, NM, SAND2013-7204, Sep. 2013.

[7] A. F. d. O. Falcão, "Wave energy utilization: A review of the technologies," *Renewable and Sustainable Energy Reviews*, vol. 14, no. 3, pp. 899-918, April 2010.

[8] M. A. Mueller, H. Polinder, and N. Baker, "Current and novel electrical generator technology for wave energy converters," in *Proc. 2007 IEEE Int. Electri. Mach. Drives Conf. (IEMDC),* pp. 1401-1406.

[9] M. Amundarain, M. Alberdi, A. J. Garrido, and I. Garrido, "Modeling and simulation of wave energy generation plants: Output power control," *IEEE Trans. Ind. Electron.,* vol. 58, pp. 105-117, 2011.

[10] M. French, "On the difficulty of inventing an economical sea wave energy converter: a personal view," *Proc. Inst. Mech. Eng., Part M-J Eng. Maritime Environment,* vol. 220, pp. 149-155, 2006.

[11] T. K. A. Brekken, A. Von Jouanne, and H. Hai-Yue, "Ocean wave energy overview and research at Oregon State University," in *Proc. 2009 IEEE Power Electron. Mach. Wind Appl.,* pp. 1-7.

[12] J. Hals, J. Falnes, and T. Moan, "A comparison of selected strategies for adaptive control of wave energy converters," *J. Offshore Mech. Arctic Eng.*, vol. 133, pp. 011401-1-011401-15, 2011.

[13] N. W. Frank and H. A. Toliyat, "Gearing ratios of a magnetic gear for wind turbines," in *Proc. 2009 IEEE Int. Electri. Mach. Drives Conf. (IEMDC),* pp. 1224-1230.

[14] M. A. Mueller, A. S. McDonald, and D. E. Macpherson, "Structural analysis of low-speed axial-flux permanent-magnet machines," in *Proc. Instit. Elec. Eng.-Elect. Power Appl.,* vol. 152, no. 6, pp. 1417-1426, 2005.

[15] N. W. Frank and H. A. Toliyat, "Gearing ratios of a magnetic gear for marine applications," in *Proc. 2009 IEEE Elect. Ship Tech. Symp. (ESTS),* pp. 477-481.

[16] N. W. Frank and H. A. Toliyat, "Analysis of the concentric planetary magnetic gear with strengthened stator and interior permanent magnet inner rotor," *IEEE Trans. Ind. Appl.* vol. 47, pp. 1652-1660, 2011.

[17] R. Montague, C. Bingham, and K. Atallah, "Servo control of magnetic gears," *IEEE/ASME Trans. Mechatronics,*, vol. 17, pp. 269-278, 2012.

[18] F. T. Jorgensen, T. O. Andersen, and P. O. Rasmussen, "The cycloid permanent magnetic gear," *IEEE Trans. Ind. Appl.*, vol. 44, pp. 1659-1665, 2008.

[19] J. Rens, K. Atallah, S. D. Calverley, and D. Howe, "A novel magnetic harmonic gear," *IEEE Trans. Ind. Appl.*, vol. 46, pp. 206-212, 2010.

[20] S. Kikuchi and K. Tsurumoto, "Design and characteristics of a new magnetic worm gear using permanent magnet," *IEEE Trans. Magn.*, vol. 29, pp. 2923-2925, 1993.

[21] K. Atallah and D. Howe, "A novel high-performance magnetic gear," *IEEE Trans. Magn.*, vol. 37, pp. 2844-2846, 2001.

[22] K. Atallah, J. Rens, S. Mezani, and D. Howe, "A novel pseudo direct-drive brushless permanent magnet machine," *IEEE Trans. Magn.*, vol. 44, pp. 4349-4352, 2008.

[23] K. T. Chau, Z. Dong, J. Z. Jiang, L. Chunhua, and Z. Yuejin, "Design of a magnetic-geared outer-rotor permanent-magnet brushless motor for electric vehicles," *IEEE Trans. Magn.*, vol. 43, pp. 2504-2506, 2007.

[24] P. O. Rasmussen, H. H. Mortensen, T. N. Matzen, T. M. Jahns, and H. A. Toliyat, "Motor integrated permanent magnet gear with a wide torque-speed

range," in *Proc. 2009 IEEE Energy Convers. Congr. Expo. (ECCE),* pp. 1510-1518.

[25] N. J. Baker, "Linear generators for direct drive marine renewable energy converters," Ph.D. dissertation, School of Engineering and Computing Sciences, Durham Univ., Dorham, UK, 2003.

[26] N. Hodgins, O. Keysan, A. S. McDonald, and M. A. Mueller, "Design and testing of a linear generator for wave-energy applications," *IEEE Trans. Ind. Electron.,* vol. 59, pp. 2094-2103, 2012.

[27] M. Mueller and N. Baker, "Direct drive electrical power take-off for offshore marine energy converters," *Proc. Inst. Mech. Eng., Part A-J Power Energy,* vol. 219, pp. 223-234, 2005.

[28] M. Mueller, "Electrical generators for direct drive wave energy converters," *Proc. IEE- Generation, Transmiss. Distrib.,* vol. 149, no. 4, pp. 446-456, 2002.

[29] H. Polinder, B. C. Mecrow, A. G. Jack, P. G. Dickinson, and M. A. Mueller, "Conventional and TFPM linear generators for direct-drive wave energy conversion," *IEEE Trans. Energy Convers.,* vol. 20, pp. 260-267, 2005.

[30] H. Polinder, M. E. C. Damen, and F. Gardner, "Linear PM Generator system for wave energy conversion in the AWS," *IEEE Trans. Energy Convers.,* vol. 19, pp. 583-589, 2004.

[31] J. Prudell, M. Stoddard, E. Amon, T. K. A. Brekken, and A. Von Jouanne, "A Permanent-magnet tubular linear generator for ocean wave energy conversion," *IEEE Trans. Ind. Appl.* vol. 46, pp. 2392-2400, 2010.

[32] H. Weh, H. Hoffman, and J. Landrath, "New permanent magnet excited synchronous machine with high efficiency at low speeds," in *Proc. 1988 Int. Conf. Electri. Machines (ICEM),* pp. 35-40.

[33] E. Spooner and L. Haydock, "Vernier hybrid machines," *Proc. Inst. Elect. Eng.-Electric Power Appl.,* vol. 150, no. 6, pp. 655-662, 2003.

[34] M. Mueller, A. McDonald, K. Ochije, and J. Jeffrey, "A novel lightweight permanent magnet generator for direct drive power take off in marine renewable energy converters," in *Proc. 2007 Eur. Wave and Tidal Energy Conf.*

[35] Y. Du, K. T. Chau, M. Cheng, and Y. Wang, "A linear magnetic-geared permanent magnet machine for wave energy generation," in *Proc. 2010 IEEE Int. Conf. Electr. Mach. Syst. (ICEMS),* pp. 1538-1541.

[36] R. C. Holehouse, K. Atallah, and W. Jiabin, "A linear magnetic gear," in *Proc. 2012 Int. Conf. Electri. Machines (ICEM)*, pp. 563-569.

[37] W. Li, S. Gao, D. Wu, and X. Zhang, "Design of a linear magnetic-geared free-piston generator for series hybrid electric vehicles," in *Proc. 2010 IEEE Vehicle Power and Propulsion Conf. (VPPC)*, pp. 1-6.

[38] J. Wang, K. Atallah, and W. Wang, "Analysis of a Magnetic Screw for High Force Density Linear Electromagnetic Actuators," *IEEE Trans. Magn.*, vol. 47, pp. 4477-4480, 2011.

[39] R. K. Holm, N. I. Berg, M. Walkusch, P. O. Rasmussen, and R. H. Hansen, "Design of a Magnetic Lead Screw for Wave Energy Conversion," *IEEE Trans. Ind. Appl.*, vol. 49, pp. 2699-2708, 2013.

[40] W. H. Keller and S. D. Sibley, "Reciprocating motor," US Patent 1043573, Nov. 5, 1912.

[41] B. Andrews, "Magnetic screw," US Patent 1562730, Nov. 24, 1925.

[42] H. T. Faus, "Magnetic transmission," US Patent 2371511, March 13, 1945.

[43] J. Gerrard and R. Paul, "Rectilinear screw-thread reluctance motor," in *Proc. Inst. Elect. Eng.*, vol. 118, no. 11, pp. 1575-1584, Nov. 1971.

[44] G. Dawkins and D. Rhodes, "An Electromagnetic Rotary-to-Linear Coupler," in *Proc. 1978 Int. Conf. Electri. Machines*, vol. 1, pp. 1-10.

[45] R. Paul, "Magnetic rotary-linear or linear-rotary converter," *IEE J. Elect. Power Appl.*, vol. 2, pp. 135-138, 1979.

[46] N. G. Vitale, "Rotary torque-to-axial force energy conversion apparatus," US Patent 6190409 B1, Feb. 20, 2001.

[47] K. Doi, W. A. Smith, H. Harasaki, M. Takagaki, Y. Ochiai *et al.*, "In vivo studies of the MagScrew total artificial heart in calves," *ASAIO J.*, vol. 48, pp. 222-225, 2002.

[48] J. Wang, G. W. Jewell, and D. Howe, "A general framework for the analysis and design of tubular linear permanent magnet machines," *IEEE Trans. Magn.*, vol. 35, pp. 1986-2000, 1999.

[49] R. K. Holm, N. I. Berg, M. Walkusch, P. O. Rasmussen, and R. H. Hansen, "Design of a magnetic lead screw for wave energy conversion," in *Proc. 2012 Int. Conf. Electr Machines (ICEM)*, pp. 618-626.

[50] *Genetic Optimization System Engineering Toolbox (GOSET) 2.6*. [online]. Available: https://engineering.purdue.edu/ECE/Research/Areas/PEDS/go_system_engineering_toolbox (URL), accessed June 2012.

[51] J. E. Heikkinen and S. Pakdelian, "Rotordynamics of a Trans-Rotary Magnetic Gear Rotor," in *Proc. 2013 ASME Int. Mech. Eng. Cong. Expo.*, pp. V04BT04A046-V04BT04A046.

[52] S. S. Nair, S. Nalakath, I. Santhi, S. Jabez Dhinagar, Y. B. Deshpande, and H. A. Toliyat, "Design aspects of high torque density-low speed permanent magnet motor for electric two wheeler applications," in *Proc. 2013 IEEE Electri. Mach. Drives Conf. (IEMDC)*, pp. 768-774.

[53] D. Staton, A. Boglietti, and A. Cavagnino, "Solving the more difficult aspects of electric motor thermal analysis in small and medium size industrial induction motors," *IEEE Trans. Energy Convers.*, vol. 20, pp. 620-628, 2005.

[54] J. Wang, and D. Howe, "Design optimization of radially magnetized, iron-cored, tubular permanent-magnet machines and drive systems," *IEEE Trans. Magn.*, vol. 40, pp. 3262-3277, 2004.

[55] J. K. H. Shek, D. E. Macpherson, M. A. Mueller, and J. Xiang, "Reaction force control of a linear electrical generator for direct drive wave energy conversion,", *IET Renew. Power Gener.*, vol. 1, no. 1, pp. 17-24, 2007.

[56] N. W. Frank, S. Pakdelian, and H. A. Toliyat, "Passive Suppression of Transient Oscillations in the Concentric Planetary Magnetic Gear," *IEEE Trans. Energy Convers.*, vol. 26, pp. 933-939, 2011.

[57] J. Falnes, *Ocean waves and oscillating systems*, Cambridge University Press, Cambridge, 2002.

[58] T. M. Lewis, A. Von Jouanne, and T. K. A. Brekken, "Wave Energy Converter with wideband power absorption," in *Proc. 2011 IEEE Energy Convers. Cong. Expo. (ECCE)*, pp. 3844-3851.

[59] E. Tedeschi, M. Carraro, M. Molinas, and P. Mattavelli, "Effect of Control Strategies and Power Take-Off Efficiency on the Power Capture From Sea Waves," *IEEE Trans. Energy Convers.*, vol. 26, pp. 1088-1098, 2011.

[60] J. Falnes. (1997), "*Principles for capture of energy from ocean waves. Phase control and optimum oscillation*," [online]. Available: http://www.phys.ntnu.no/instdef/prosjekter/bolgeenergi/phcontrl. pdf i, (URL), accessed Jan 2014.

[61] A. Schacher *et al.*, "Novel control design for a wave energy generator," in *Proc. 2008 AIAA Aerospace Science Meet. Exhibit.*, pp. 1-9.

[62] T. K. A. Brekken, B. A. Batten, and E. A. Amon, "From Blue to Green," *IEEE Control Systems Mag.*, vol. 31, pp. 18-24, 2011.

[63] M. Richter, M. E. Magana, O. Sawodny, and T. K. A. Brekken, "Nonlinear Model Predictive Control of a Point Absorber Wave Energy Converter," *IEEE Trans. Sustain. Energy*, vol. 4, pp. 118-126, 2013.

APPENDIX

The analytical model for calculating the axial force of a TROMAG is adopted from [38] and [48], and is summarized below. As a first step, as depicted in Fig. 70(a), the TROMAG is approximated by a 2D system. The area enclosed within the dashed rectangle of Fig. 70(a) is zoomed and shown in Fig. 70(b) and Fig. 70(c). Then the translator magnets are removed, as indicated by dashed lines in Fig. 70(b). In the resultant system, the magnetic field due to rotor magnets is calculated. It would suffice to obtain the radial component of field only because the axial force, whose calculation is of the interest in this paper, arises from that component. To calculate the field of rotor magnets, Laplace (A.1) and Poisson (A.2) equations must be solved in the air gap region (both the physical air gap and the air region which resulted from removing the translator magnets) and in the rotor magnet region, respectively.

$$\nabla^2 \vec{A} = 0 \tag{A.1}$$

$$\nabla^2 \vec{A} = -\mu_0 \nabla \times \vec{M} \tag{A.2}$$

In the above equations, $\vec{A}$ denotes the magnetic vector potential and has only an azimuthal component due to the symmetry in Z direction. $\vec{M}$ denotes the magnetization vector of magnets and has only a radial component because the magnets are assumed to be radially magnetized.

$$\vec{M} = \overrightarrow{M_r} = \frac{4B_r}{\mu_0} \sum_{n=1,2,\dots} \frac{\sin\left[(2n-1)\frac{\pi}{2}\frac{w}{\tau_P}\right]}{(2n-1)\pi} \hat{a}_r \tag{A.3}$$

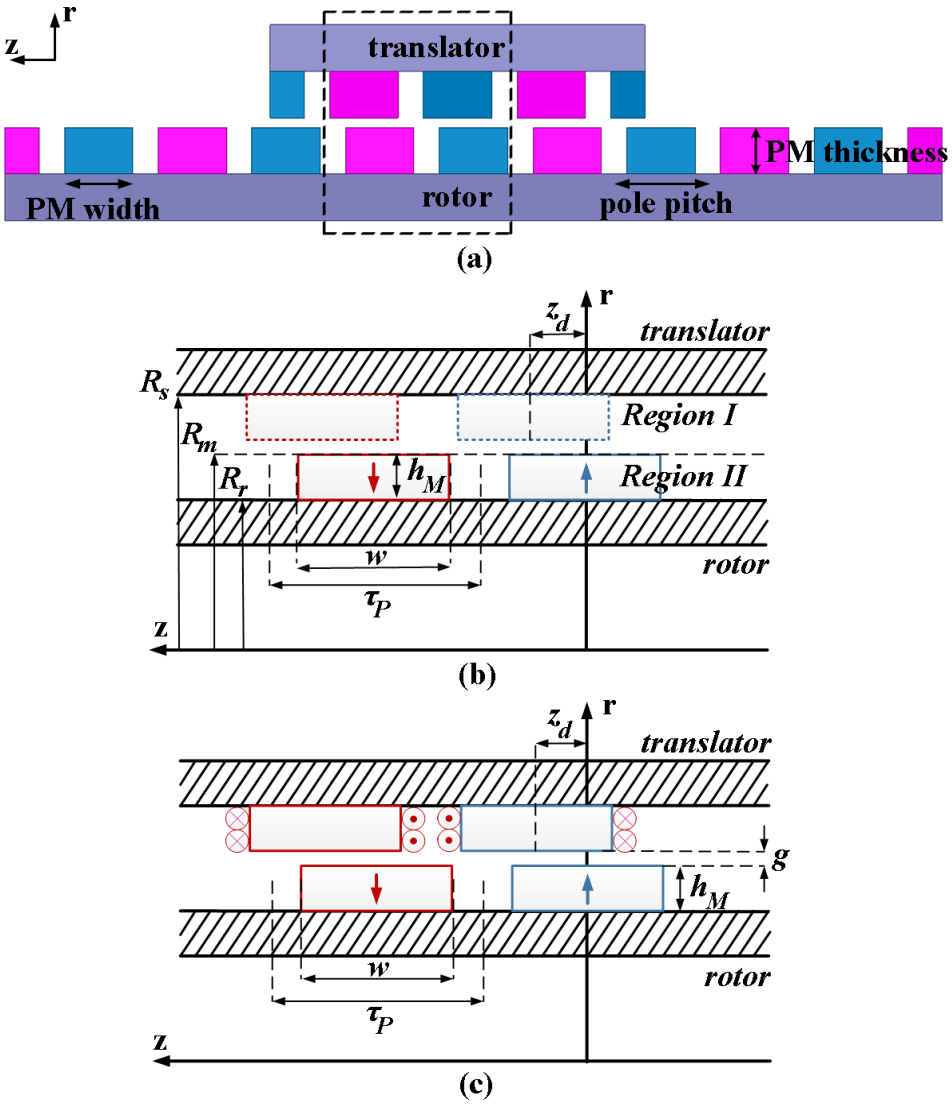

Fig. 70. TROMAG force calculation. (a) 2D approximation of the TROMAG. (b) field due to rotor magnets in the absence of translator magnets. (c) replacing translator magnets with equivalent current carrying coils.

In (A.3), $\hat{a}_r$ is the unity vector in radial direction and n is the index of summation. The radial and axial components of flux density in the air gap region, B_{rI} and B_{zI}, are as follows:

$$t_s \cong \frac{4}{\alpha_r} = \frac{4}{B_r/(2J)} \Rightarrow B_r \cong \frac{8J}{t_s} \tag{63}$$

$$B_{rI} = -\sum_{n=1,2,\ldots} [a_{In} I_1(m_n r) + b_{In} K_1(m_n r)] \cos m_n z \tag{A.4}$$

$$B_{zI} = \sum_{n=1,2,\ldots} [a_{In} I_0(m_n r) - b_{In} K_0(m_n r)] \sin m_n z \tag{A.5}$$

in which I_0 and K_0 are modified Bessel functions of first and second kind of order zero, I_1 and K_1 are modified Bessel functions of first and second kind of order one, and m_n is defined as $(2n\text{-}1)\pi/\tau_P$. The radial and axial components of flux density in the magnet region, B_{rII} and B_{zII} are as follows:

$$B_{rII} = -\sum_{n=1,2,\ldots} \begin{bmatrix} (F_{An}(m_n r) + a_{IIn}) I_1(m_n r) + \\ (-F_{Bn}(m_n r) + b_{IIn})\, K_1(m_n r) \end{bmatrix} \cos m_n z \tag{A.6}$$

$$B_{zII} = \sum_{n=1,2,\ldots} \begin{bmatrix} (F_{An}(m_n r) + a_{IIn}) I_0(m_n r) + \\ (F_{Bn}(m_n r) - b_{IIn})\, K_0(m_n r) \end{bmatrix} \sin m_n(z) \tag{A.7}$$

To express unknown coefficients, the following definitions are made:

$$P_n = \frac{4B_r}{\tau_P} \sin\left[(2n-1)\frac{\pi}{2}\frac{w}{\tau_P}\right] \tag{A.8}$$

$$\begin{aligned} c_{1n} &= I_0(m_n R_s) & c_{2n} &= K_0(m_n R_s) \\ c_{3n} &= I_0(m_n R_r) & c_{4n} &= K_0(m_n R_r) \\ c_{5n} &= I_0(m_n R_m) & c_{6n} &= K_0(m_n R_m) \\ c_{7n} &= I_1(m_n R_m) & c_{8n} &= K_1(m_n R_m) \end{aligned} \tag{A.9}$$

The coefficients $F_{An}(m_n r)$ and $F_{Bn}(m_n r)$ are as follows:

$$F_{An}(m_n r) = \frac{P_n}{m_n} \int_{m_n R_r}^{m_n r} \frac{K_1(x)\, dx}{I_1(x)K_0(x) + K_1(x)I_0(x)} \tag{A.10}$$

$$F_{Bn}(m_n r) = \frac{P_n}{m_n} \int_{m_n R_r}^{m_n r} \frac{I_1(x)\, dx}{I_1(x)K_0(x) + K_1(x)I_0(x)} \tag{A.11}$$

The coefficients a_{In}, a_{IIn}, b_{In}, and b_{IIn} are obtained from (A.12) to (A.14).

$$\begin{pmatrix} \mu_r\left(\frac{c_{5n}}{c_{6n}} - \frac{c_{1n}}{c_{2n}}\right) & -\left(\frac{c_{5n}}{c_{6n}} - \frac{c_{3n}}{c_{4n}}\right) \\ \left(\frac{c_{7n}}{c_{8n}} + \frac{c_{1n}}{c_{2n}}\right) & -\left(\frac{c_{7n}}{c_{8n}} + \frac{c_{3n}}{c_{4n}}\right) \end{pmatrix} \begin{pmatrix} a_{In} \\ a_{IIn} \end{pmatrix} = \begin{pmatrix} F_{An}(m_n R_m)\frac{c_{5n}}{c_{6n}} + F_{Bn}(m_n R_m) \\ F_{An}(m_n R_m)\frac{c_{7n}}{c_{8n}} - F_{Bn}(m_n R_m) \end{pmatrix} \tag{A.12}$$

$$b_{In} = \frac{c_{1n}}{c_{2n}}\, a_{In} \tag{A.13}$$

$$b_{IIn} = \frac{c_{3n}}{c_{4n}}\, a_{IIn} \tag{A.14}$$

The next step is to use the Lorentz force law to calculate the force exerted on translator magnets. To that end, the translator magnets are replaced with equivalent current-carrying sheets, as depicted by crosses and dots in Fig. 70(c). Each sheet is an annulus around the Z-axis with inner radius of $r=R_m+g$, outer radius of $r=R_s$), and an infinitesimal width (length in Z direction) of *dz*. The current flowing in each sheet equals the magneto-motive force (mmf), F_{PM}, generated by the magnet it is replacing.

$$F_{PM} = H_c h_M \tag{A.15}$$

In (A.15), H_c is the PM coercivity and h_M is the PM thickness. When B_r, μ_0, and μ_r denote the PM residual flux density, permeability of the vacuum, and recoil permeability of the PM material, then $H_c = B_r/\mu_0 \mu_r$.

Finally, the force exerted on each current-carrying sheet can be obtained by applying Lorentz's force law and integrating the force over the surface of current sheet, *S*.

$$\vec{F} = \int (\vec{H}_c \times \vec{B}_I) dS \tag{A.16}$$

In (A.16), $\widehat{H}_c$ is a vector whose magnitude is H_c and its direction is the same as that of the flow of current in the equivalent current sheet. $\vec{B}_I$ is the magnetic flux density vector in Region I, and $dS = 2\pi r.dr$.

The radial component of flux density results in an axial force component, F_z on the translator as follows:

$$F_z = \frac{4\pi B_r}{\mu_0 \mu_r} \sum_{n=1,2,\ldots} K_{rn} \sin(m_n w/2) \sin(m_n z_d) \tag{A.17}$$

in which w is the magnet width, and z_d is shown in Fig. 70. The coefficient K_{rn} is given by

$$K_{rn} = \int_{R_s+g}^{R_s} [a_{In} I_1(m_n r) + b_{In} K_1(m_n r)] \, r \, dr \tag{A.18}$$